MULTI-SCALE THERMAL MODELING METHODOLOGY FOR HIGH POWER-ELECTRONIC CABINETS

A Thesis
Presented to
The Academic Faculty

by

Ludovic Burton

In Partial Fulfillment
of the Requirements for the Degree
Master of Sciences in the
George W. Woodruff School of Mechanical Engineering

Georgia Institute of Technology
December 2007

MULTI-SCALE THERMAL MODELING METHODOLOGY FOR HIGH POWER-ELECTRONIC CABINETS

Approved by:

Dr. Yogendra Joshi, Advisor
School of Mechanical Engineering
Georgia Institute of Technology

Dr. Srinivas Garimella
School of Mechanical Engineering
Georgia Institute of Technology

Dr. Syed I. Haider
School of Mechanical Engineering
Georgia Institute of Technology

Date Approved: August 17th, 2007

ACKNOWLEDGEMENTS

I would like to express my deep and sincere gratitude to my advisor, Professor Yogendra Joshi, Ph.D., John M. McKenney and Warren D. Shiver Distinguished Chair in Building Mechanical Systems and director of the Microelectronics and Emerging Technologies and Thermal Laboratory (METTL), for his guidance during my studies at the Georgia Institute of Technology. His wide knowledge in thermal sciences, his understanding, and encouragements have been of great value for me.

I would like to thank Dr. Syed I. Haider for his collaboration and extensive discussions during this study. I also greatly appreciate the support and encouragement of my committee member, Dr. Garimella. I wish to thank my colleagues and friends at the METTL, and more particularly Graham Nelson and Quihong Nie for sharing their thoughts and providing me a collaborative and friendly work environment.

I wish also to express my deepest gratitude to my mother, Ange Marie, for her encouragements and giving me the opportunity to study abroad.

TABLE OF CONTENTS

LIST OF TABLES

Page

LIST OF FIGURES

Page

LIST OF SYMBOLS AND ABBREVIATIONS

Symbols

a_i, b_i ……..….....Modal weight coefficients

A, L, R,V, ∑……..…... Matrices

α.……...Porous medium permeability

$c_{p.}$ …….Specific heat

D_h ……Hydraulic diameter

Δp……..…Pressure drop

E ……...…….Energy content

ε …….…….…… Surface roughness

F_{HX} …….LMTD correction factor for the heat exchanger unit

f…….....Friction factor

f_1, f_2, f_3, f_4 ……...Equipment performance functions

$\vec{\varphi}$ ……Eigenvector

L…….…....Plenum length

λ. ……..Eigenvalue

MRE……...…….Mean relative error

m……...…...Number of observations

p……Number of modes

n……...……....Number of system DOF

N_f……..Number of fans in parallel

N_{HX} ……..……...Number of heat exchanger units

Ω……Domain

Q…….Heat load

RE……Relative Error

Re……..…….Reynolds number

R_{th}……..…….Thermal resistance

$\vec{R}'$……..Correlation matrix

ρ …….……..……..Density

T …….……..……..Temperature

$\vec{U}$ …….Velocity field observation matrix

UA_{HX} …….……..Overall thermal conductance of the heat exchanger unit

u, v, w ……...……..Velocity components

$\dot{v}_a$…….…...Observation parameter, total air flow rate through

$\dot{v}_w$……Water flow rate through each heat exchanger unit

x, y, z.…….…….Spatial coordinates

Acronyms

CFD/HT…….Computational Fluid Dynamics and Heat Transfer

CFM.....Cubic Feet Minute

CTM……..……Compact Thermal Model

DOF……...……..…….Degrees of Freedom

HX……Heat Exchanger

IGBT……..……Insulated Gate Bipolar Transistors

IPS…….Integrated Power System

ITD……Initial temperature Difference

LMTD.....Log Mean Temperature Difference

PCM.....Power Conversion Module

POD……....Proper Orthogonal Decomposition

RANS……...……. Reynolds-Averaged Navier Stokes

SSCM……. ……Ship Service Converter Module

SSIM…….……. ……Ship Service Converter Module

TIM…….Thermal Interface Material

SUMMARY

Future generation of all-electric ships will be highly dependent on electric power, since every single system aboard such as the drive propulsion, the weapon system, the communication and navigation systems will be electrically powered. Power conversion modules (PCM) will be used to transform and distribute the power as desired in various zone within the ships. As power densities increase at both components and systems-levels, high-fidelity thermal models of those PCMs are indispensable to reach high performance and energy efficient designs. Efficient systems-level thermal management requires modeling and analysis of complex turbulent fluid flow and heat transfer processes across several decades of length scales.

In this thesis, a methodology for thermal modeling of complex PCM cabinets used in naval applications is offered. High fidelity computational fluid dynamics and heat transfer (CFD/HT) models are created in order to analyze the heat dissipation from the chip to the multi-cabinet level and optimize turbulent convection cooling inside the cabinet enclosure. Conventional CFD/HT modeling techniques for such complex and multi-scale systems are severely limited as a design or optimization tool. The large size of such models and the complex physics involved result in extremely slow processing time. A multi-scale approach has been developed to predict accurately the overall airflow conditions at the cabinet level as well as the airflow around components which dictates the chip temperature in details. Various models of different length scales are linked

together by matching the boundary conditions. The advantage is that it allows high fidelity models at each length scale and more detailed simulations are obtained than what could have been accomplished with a single model methodology.

A proper orthogonal decomposition (POD) methodology has been performed to develop reduced-order compact models of the PCM cabinets. The reduced-order modeling approach based on POD reduces the numerical models containing 35×10^9 DOF down to less than 20 DOF, while still retaining a great accuracy. The reduced-order models developed yields prediction of the full-field 3-D cabinet within 30 seconds as opposed to the CFD/HT simulations that take more than 3 hours using a high power computer cluster. The reduced-order modeling methodology developed could be a useful tool to quickly and accurately characterize the thermal behavior of any electronics system and provides a good basis for thermal design and optimization purposes.

CHAPTER 1

INTRODUCTION

The trend in commercial and military ships is toward improving electric propulsion, ship service power and electric loads in order to obtain an integrated power system (IPS). The IPS program of the U.S. Navy combines development in electric propulsion systems and power electronics to improve ship performance and flexibility in power usage, along with reducing the number of prime movers, the maintenance costs and the number of crew members [1]. The concept of all-electric IPS ships is to use common sets of generators for propulsion, combat systems and other ship service loads. Direct current (DC) distribution is used to supply power to the various zones where power conversion modules (PCM) are used to transform the current as desired. Switching losses in the transistors along with the resistance in inductors and capacitors, lower the PCM efficiency and generate large heat losses. Development in the computer industry since the invention of the transistor in 1947 by Bell Labs allows more power and functionality to electronic packages and power modules. Because of the continuing miniaturization of electronics, increasing heat densities have made the cooling of microprocessor devices much more challenging. Heat removal is a critical issue in their design. The thermal management community has studied various possibilities to develop techniques able to satisfy emerging challenges and improve cooling systems' efficiencies. The need for cost-effective cooling solutions pushed researchers to investigate unique methods involving new materials, liquid cooling and multi-phase transport.

Air cooling has been used extensively to dissipate heat for generations of electronic devices. This heat removal method has been pushed towards its limits and will

have to be coupled with other techniques in order to satisfy cooling requirements of future power electronics. Identifying methods to improve thermal management within the PCM systems will allow those units to operate more efficiently and be more reliable. Thermally more efficient PCMs could have higher power densities and result in a more compact system. Therefore, the development of packaging tools able to analyze and optimize the cooling requirement of complex systems, such as air-to-water cooled power cabinets, is essential.

The principal objective of this thesis is to elaborate a methodology for thermal modeling of complex power cabinets used in naval applications. This goal is achieved by investigating the multi-scale nature of the systems. High fidelity computational fluid dynamics and heat transfer (CFD/HT) models are created in order to analyze the heat dissipation from the chip to the multi-cabinet level and optimize turbulent convection cooling inside the cabinet enclosure. A compact model is developed which incorporates proper orthogonal decomposition (POD) for reduced-order modeling to perform system level analysis for optimization purposes. In Section 1.1, the background and the motivation for the work presented within this thesis are given. This section covers the challenges in next generation of electronic systems, system level thermal management of enclosures and a description of computational fluid dynamics. In Section 1.2 a review of the literature covering analysis, optimization, and compact modeling of electronic chip packages and power cabinets is presented.

1.1 Background and Motivation

Moore's law is the empirical observation made in 1965 by Dr. Gordon Moore, co-founder of Intel, stating that the density of transistor on an integrated circuit (IC) doubles every 24 months [2]. This observation was at first a short term forecast that rapidly became an objective for the entire semiconductor industry. Assuming that chip complexity and performance are proportional to the number of transistors, this law is

used to predict semiconductor transistor density, performance and subsequently power dissipation. The microprocessor industry has closely followed Moore's law and used it as a driver for continuous technological evolution. This trend is also observed for other products within the semi-conductor industry. Reduced transistor size, faster switching speeds and greater on-chip functionality, combined with a slowdown in voltage scaling, have resulted in an increase in heat generation rates of chips. Large nonuniformities in heat flux at the chip level which lead to component failure, are also observed [3]. As power densities increase at both the component and circuit board levels, heat fluxes exceed 100W/cm^2 for commercial electronics and over 1000W/cm^2 for military high-power electronics are projected [4]. For electronic devices such as integrated power converters based on insulated gate bipolar transistors (IGBT) operating in temperature above 100°C, thermal concerns are becoming critical. High operating temperature generally compromises performance of devices and may in some cases have an impact on reliability. Additionally, temperature cycles resulting from turning on and off large amounts of power can cause fatigue of the die and other elements of the chip package.

The demand for electronics working under thermally-challenging conditions is also increasing. Defense, aerospace, automotive and oil exploration applications use electronics devices in harsh environments. As shown in Table 1, harsh environment electronics operate undergo much larger range of operating temperature

Table 1: Operating Temperature of Electronics [5]

Application	Operating Temperature
Commercial	0°C – 70°C
Industry	-40°C – 85°C
Automotive	-40°C – 125°C
Military	-55°C – 125°C
Aviation	-65°C – 225°C

In addition to severe temperature conditions, electronics in military applications must maintain reliability to vibration, changes of altitude, and humidity. Also, military

electronics are required to have a lifetime up to 30 years, while commercial electronics lifetime requirements typically don't exceed 5 years [5]. Furthermore, weight and volume are even larger constraints for military applications, and as a result, electronic devices are denser than in commercial applications. In order to ensure reliability and cost effectiveness of electronics under such extreme temperature and physical constraints, the introduction of advanced thermal management systems become essential in the design of harsh environment electronics, and more particularly for military applications.

1.1.1 Challenges for Electronics Thermal Management

Heat in electronic systems is removed at the chip level either by conduction or convection and then transferred to the environment or a coolant. The thermal management technique can be classified as either passive, active, or a combination of the two (hybrid). Passive cooling techniques are relatively simple, and their usage does not require external power. The simplicity of such systems makes them reliable at relatively low cost. The major passive cooling solutions are obtained through conduction (heat spreaders, thermal interface materials), natural convection (heat sinks, liquid immersion), radiation (coating, surface treatments) or phase change (heat pipes, phase change materials). However, passive cooling techniques have low cooling performance requiring a large device size. Consequently, high-power systems require active techniques, which require input power but have larger heat removal capacity. The major active techniques are forced convection (fans, active heatsinks), pumped loops (heat exchanger, liquid cold plates, micro-channels, jet spray), thermoelectric cooling (TEC) and refrigeration.

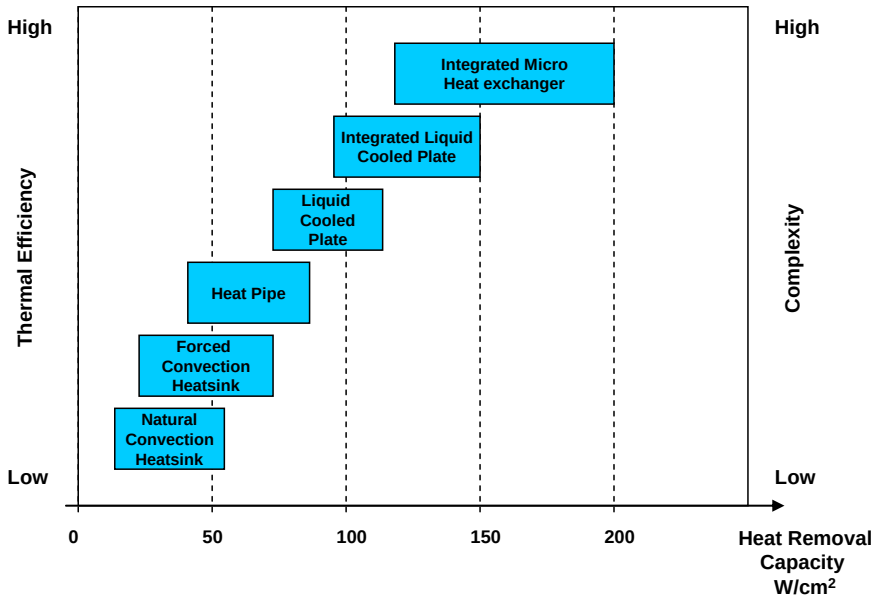

Figure 1: Thermal Management Techniques and Heat Removal Capacity [5]

With the increase in heat dissipation at the chip level, air cooling technique was enhanced through the use of advanced fans and heat sinks with optimized fin design. Analysis and design of heat sinks have been a major research topic for the thermal management community. Gardner [6] and Elenbaas [7] were the pioneers of heat sink studies in the 1940s and developed analysis for fin efficiency and convection through parallel plates respectively. Heat sink optimization work was extended by study of rectangular-fin arrays by Starner and McManus [8], Van de Pol and Tierney [9] and more recently by Aihara and Maruyama [10]. Advances in cooling performances have been obtained through improvement of manufacturing technologies, fan design, and material science. The more advanced air convection cooling technologies exceed 50 W/cm^2 as shown by Figure 1. It is important to note that heat fluxes reached today by air cooling could have been obtained only by liquid cooling in the late 1980s. In 1985, 5 W/cm^2 was considered the limit of air cooling [11]. To meet the demands for higher air cooling performance, more complex heat sinks were developed. The use of highly thermally-conductive materials such as graphite creates a reduction in heat sink base plate thermal spreading resistance. The use of two phase heat transfer mechanism is also emerging.

Base plate made of two phase heat pipes can reach thermal performances 25 times higher than copper block base plate [12]. Integration of advanced technologies not only enhances overall thermal performance but also increases cost [12].

Enhancing the performance of air cooling does not limit only to optimization of heat sink design but also requires minimizing chip-to-ambient thermal resistance in the heat transfer chain. The main areas of development for air cooling are listed in Table 2.

Table 2: Challenges to Optimize Junction to Ambient Thermal Resistance [5]

Thermal Resistance	Thermal Management Challenge
Junction-to-case	IC-level cooling
	Package architecture development
	Interface thermal resistance minimization
Case-to-heat sink	Interface thermal resistance minimization
Heat sink-to-ambient	Advanced heat sink manufacturing technologies
	Integration of heat spreading technologies
	Integration of hybrid cooling solutions
	Aerodynamic fan performance improvement
	Airflow optimization
	Heat sink surface fouling minimization
	Standardization of thermal management hardware performance characterization
	Sustainability

In order to ensure efficient heat transfer from the die to ambient and minimize contact resistance between the die and the heat spreader as well as the chip package and the heat sink base thermal interface materials (TIM) are used. In several applications, the chip package-to-heat sink thermal resistance is equivalent to the thermal resistance of the actual heat sink. Therefore, improving the TIM performance has been the focus of several research programs. A large variety of materials, adhesives and greases has been investigated recently. Metal particle filled gels and phase change materials have been developed and integrated to high power devices [12].

Fan technology has been largely developed for electronic cooling applications. The objective of new fan design and technology has been to increase airflow rate at comparable pressure. The development of novel solutions faces the following challenges and obstacles:

- Low aerodynamic performance due to high pressure drop induced by enclosure screens and filters. Constricted operating space within electronic devices also results in low fan performances.
- Fan bearing reliability
- High manufacturing cost
- Induced acoustic noise emissions. Reduction in noise generated by fans has been the primary motivation for the development of liquid cooling for desktop computer.

1.1.2 Facility and Rack Cooling

Data centers are facilities used for housing large amount of electronics such as computers, servers and communications equipment. Such facilities are used by organizations requiring storage and processing of large amounts of data. Shipboard electronics and computing facilities such as data centers are housed within large centralized locations. As such, facility level cooling of electronics is of significant interest. As data are crucial for those organizations and electronic power density increases, the operating environment remains under strict control, and the development of efficient air conditioning systems for such infrastructures is under particular consideration. New rack architectures, such as blade servers, have higher power densities than a traditional rack. For comparison, in 2000 a rack of servers consumed 2 kW. In 2002, the heat load had risen to 6 kW and today servers' heat load can go up to 30 kW. In 2007, power and cooling costs overcame the investments for new equipments.

With the use of air cooling remaining the main heat removal mechanism for present and future generations of high-power electronic devices, the need to control electronics operating temperatures considerably increases in power systems design. As stated by Garimella *et al.* [3], combined efforts of industry and university research programs are necessary to develop new thermal management technologies and to define new opportunities in order to ensure reliability of future generations of high power electronics. Integration of thermal analysis tools and processes at early stages of new electronic designs allows engineer to investigate cooling solutions by avoiding costly and time-consuming experiments. Thermal analysis can also be used at later stages of the design process for verification and optimization purposes.

1.2 Compact Modeling of Electronic Systems

A detailed model represents the physical properties of a package as closely as possible. A properly-constructed detailed model has to be boundary condition independent to accurately predict the temperature distribution within the package, regardless of the environment. Detailed models are suitable for use in design simulations to determine the thermal characterization of a single package such as junction-to-ambient air thermal resistance; However, the use of such high-fidelity models is usually not feasible for system-level simulations involving numerous semi-conductor packages. Due to the wide disparity in length scales involved, the computational resources required for solving complex problems such as the PCM cabinets would be excessive if each electronic component is represented in detail. In order to do so, compact models have to be introduced. A compact thermal model (CTM) aspires to predict package thermal behavior by taking a detailed model and extracting a far less grid-intensive representation. That way, the accuracy in predicting the temperatures at key points in the package, such as the junction, is preserved using far less computational effort.

An efficient thermal design has to focus on the complete heat transfer chain of an electronic system. With the heat generated within the chip being conducted through IC board, modules, and then dissipated at the system level, thermal analysis of electronics is a complex heat transfer problem. Nie and Joshi [13] have shown that at least five decades of length scale and modes of heat transfer have to be resolved simultaneously. The multiple length scales involved in the heat transfer chain from the chip level to the multi-cabinet level are illustrated in the following figure.

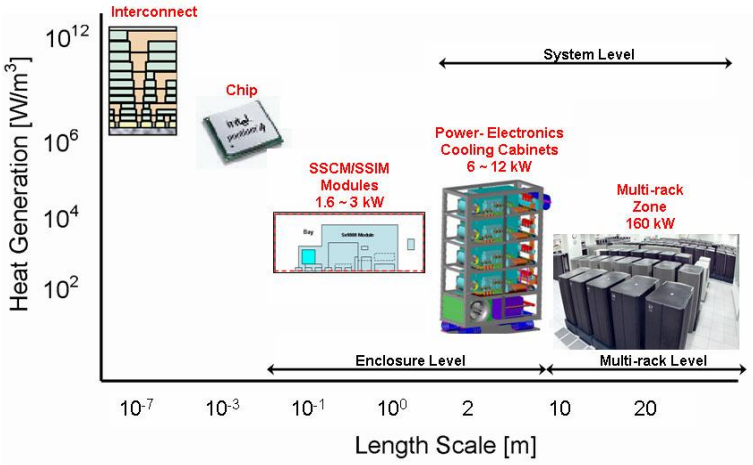

Figure 2: Multi-scale Hierarchy Involved in Electronic Modeling

Compact modeling helps to develop active thermal management techniques which can also be directly connected to the power management system of power modules in order to limit heat losses and prevent overheating or power cycling failures.

1.2.1 Computational Fluids Dynamic and Heat Transfer Modeling

CFD/HT models use numerical methods and algorithms to solve and analyze problems that involve fluid flows. The spatial domain is discretized into small cells to form a volume mesh or grid. A three-dimensional CFD/HT simulation of an incompressible turbulent flow with negligible body forces and buoyancy effects solves the following Reynolds-averaged Navier Stokes (RANS) continuity, momentum and

energy equations to evaluate velocity, temperature and pressure fields of airflow in the enclosure.

$$\nabla \cdot \vec{u} = 0 \tag{1}$$

$$\vec{u} \cdot \nabla \vec{u} - \nabla \cdot (\nu \nabla \vec{u}) + \frac{1}{\rho} \nabla p = 0 \tag{2}$$

$$\vec{u} \cdot \nabla T - \nabla \cdot (\alpha \nabla T) = 0 \tag{3}$$

Simulation of a three-dimensional air cooled power electronics problem must be checked for mesh and boundary condition independence. Local mesh refinement is used to improve the resolution and capture the complex physics involved in the system. The CFD/HT model simulates thermal fields based on geometrical and boundary conditions such as component sizes, configurations, presence of ventilation, and heat sources. Based on these CFD/HT simulations, a reduced-order model with a small number of parameters that adequately capture the complex thermal behavior of the system may be developed. The reduced order model was obtained using the proper orthogonal decomposition (POD) technique discussed in section 1.4.

Despite advances in CFD/HT based numerical modeling and its capacity to analyze complex electronic systems, even large electronic corporations with thermal design capabilities tend to outsource both electronics cooling design and research to specialized consulting firms and academic institutions. As thermal engineers increasingly integrate CFD/HT tools within their design process, the need for detailed studies validating CFD/HT based numerical models and compare results obtained with experimental data is needed. The application of CFD/HT to electronic systems is discussed by Tucker [14]. A comparison of the major commercial and non commercial CFD/HT programs is provided. Agreement with experiments was found to be within 30% for all programs. Baelmans *et al.* [15] developed a compact thermal model (CTM) for enclosures with forced convection, focusing on typical complex flow features where CFD/HT accuracy is poor. Results obtained from CFD/HT analysis were then compared

with experimental data. Fan modeling and induced swirling flow was investigated. It was found that the outlet profile could be accurately predicted by a fan model; however induced swirling flow was not represented well using a $k - \varepsilon$ turbulence model. The pressure loads and friction forces induced by screens was studied as well. It was shown that the flow around closely placed components was well simulated if a distance between theses components and the screen about 5-10 times the screen diameter hole is respected. Also, the flow in between printed circuit boards (PCB) and around in line position electronic components was investigated. It was concluded that velocity field after the second row of component is not well predicted.

As a compact model of an electronic package is a simplification of a detailed thermal model, a methodology to develop accurate compact models independent to boundary condition is discussed in [16-18]. It is shown that values from compact models developed with this systematic strategy typically approach detail model values within 6%. Vinke [17] also shows that high fidelity CTMs can be obtained through the development of thermal resistance networks.

The air flow around electronic chip and components was studied as well by Dhinsa *et al.* [19]. A comparison between several turbulence models including the distance from nearest wall and the local velocity (LVEL), Wolfshtein, Norris and Reynolds, $k - \varepsilon$, $k - \omega$, shear-stress transport (SST), and $k\varepsilon$ / kl models is given. It has been shown that the $k\varepsilon$ / kl model simulate the flow profile in the wake of a component pretty well and appears to approach mesh independence just as rapidly as the $k - \varepsilon$ model. The $k - \varepsilon$ model, which is one of the most common turbulence models, is used as the default model in many CFD/HT codes. As the $k - \omega$, it is a model using two extra transport equations to represent the turbulent properties of the flow. The $k - \varepsilon$ model was found to predict the flow profile very poorly. Such model has difficulties to predict flow with low Reynolds number.

Muthuraj *et al.* [20] present the thermal analysis of an RF communication sub-system. Like the PCM-1 and PCM-2 power cabinets, such electronic systems are housed in sealed enclosures to protect them against the corrosive marine environment. Since laboratory tests are not representative of actual operating scenario, CFD/HT thermal analysis was conducted to obtain transient and failure analysis of the unit at simulated marine conditions. Gupta [21] describes a methodology for modeling of large-scale telecommunication racks using a "zoom-in" approach. A compact model of a telecom system was developed in order to define hot spots within the system. A more detailed model is used to represent the printed circuit board experiencing the system's largest temperature. Then the card level model was used to simulate the near-component flow field in details and to extract temperatures of the components on the card. The boundary conditions of the card compact model are extracted from the system model. A similar multi-scale methodology for air-cooled power system is given by Nie and Joshi [13]. A two-step "zoom in" multiscale model was developed in order to better simulate the flow and heat transfer at both the system level and chip package level. This model was then successfully coupled with a POD reduced order technique.

1.2.2 IGBT Compact Modeling

Insulated gate bipolar transistor (IGBT) power modules are widely found in modules for power conversion application within the industry. IGBTs are used in medium to high power applications for generating large power pulses. The main causes of power module failures are related to overheating and power cycling. As stated earlier, high operating temperature is a destructive player in the lifetime of a power module as much as damages from physical stress cycles leading to wire bond interfaces or die-attach solder joint failures.

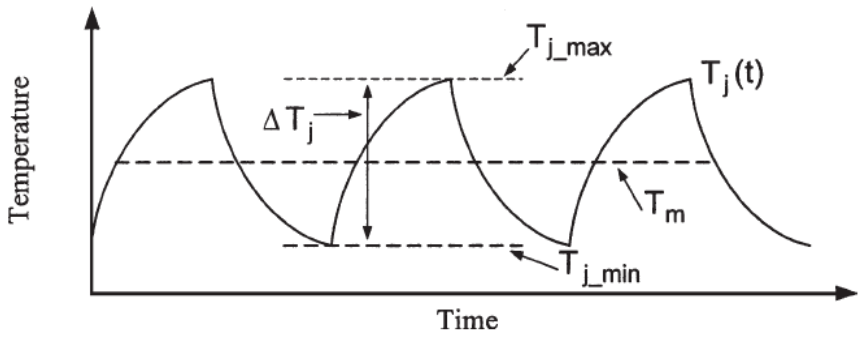

Figure 3: IGBT Typical Temperature Variation

The junction temperature variation over time of IGBT module is illustrated by Figure 3. Recently, several techniques were introduced to integrate in power electronics, such as multi-chip IGBT modules, controller which monitors temperatures of the multiple semiconductor dies, and adjusts cooling such that the desired performance levels can be obtained. Murdock *et al*. developed active thermal control techniques such as closed loop observers to limit the junction temperatures of such power devices. An algorithm monitoring the switching frequency and the output current of the IGBT allows to predict the heat dissipated by the modules.

Shammas *et al* [22] used finite element modeling to investigate the effects of thermal fatigue on the thermal performance of power module packages. A thermal analysis was done for an 800A-1800V IGBT module. Temperature dependent thermal conductivity of the silicon chip and cycling power pulse were taken into consideration to simulate real thermal cycling conditions and obtain transient values of the temperature distribution within the package. From the temperature excursion values, the shear strain and the number of cycles to failure of the solder joint are estimated.

Wen *et al*. [23] studied the issues related with thermal management and thermo-mechanical reliability of 3-D power electronic package. A finite element analysis of a half bridge power module dissipating 800 Watts total was performed. The module under study consisted of two high power IGBT and two diodes (both rated at 1200V and 75A)

dissipating respectively 300W and 100 W. The particularities of this package are the copper interconnect replacing conventional wire bonding as well as the thick metal posts and metal layers directly soldered onto the power chips to form an interconnected package offering double-sided cooling configuration (see Figure 4).

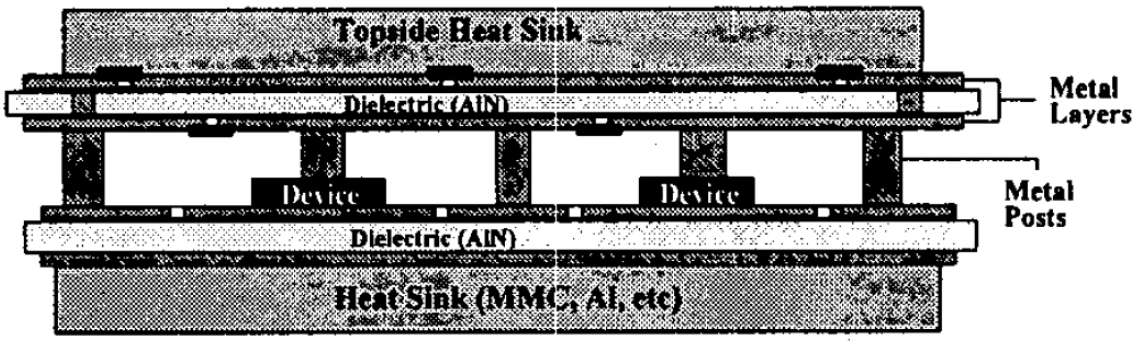

Figure 4: 3-D Power Module Interconnect Scheme [23]

A steady-state heat transfer analysis was completed to describe the temperature distribution though operation. Nonlinear static and creep analysis was used to evaluate residual stress and thermo-mechanical response induced by the soldering process. The maximum junction temperature in such double-side cooling power package was estimated to be 119°C.

Lee [24] describes a CFD/HT based thermal modeling of IGBT power module. The power module studied has a total heat dissipation of 1200 W and a maximum allowable junction temperature of 100°C. Conventionally, such power module is mounted to either an air cooled plate-fin heat sink using some type of TIM or a liquid cooled base plate. Recent development on metal matrix composites (MMC) encourages the use of liquid channel cooled MMC structures for high heat cooling applications. Such internally liquid cooled module is described in Figure 5.

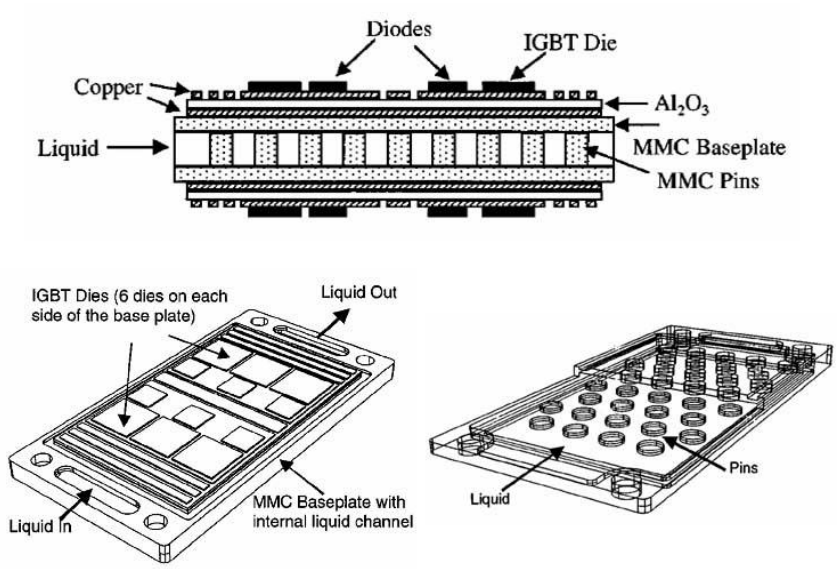

Figure 5: Liquid Cooled Hybrid Power Module [24]

By introducing different pin array designs, Lee investigated the effects of total convective and fluid pattern on the junction temperature. The analysis shows that the best pin array design was two rows of rectangular pins. The maximum junction temperature was calculated to be 99.4°C. A major advantage of such design is that issues related to nonuniform temperature distribution across the device are minimized since a maximum temperature variation of 1°C among the multiple chips is observed.

Berning *et al.* [25] developed an electro compact model able to simulate transient thermal data of multi-chip IGBT modules. The power module studied experience high power heating conditions (1080-7700W) during short period of time (under 0.003 sec). Various research works describe the development of RC compact models and electro-thermal methods for static and thermal analysis of IGBT multi-chip modules. A lumped parameter network called Foster network, consisting of parallel resistance R and capacitance C sub-circuit connected in series was used to form a RC compact thermal model. The thermal response of every single layer of power IGBT module was described by the calculated thermal impedance of the system. Finite element modeling was used to define the temperature observations at the layer boundaries, that are use to define the thermal impedance of each layer.

1.3 Introduction to Proper Orthogonal Decomposition

CFD/HT modeling is computationally expensive and time consuming, and is not economical for optimization or exploring large number of design options. The proper orthogonal decomposition (POD) based reduced order modeling technique offers a viable, low-cost alternate. It provides an orthonormal basis for representing the given data, which is optimal in a least squares sense [10]. The POD technique identifies basis functions or dominant modes which optimally capture the energy content from the multi-dimensional data previously obtained experimentally or numerically by CFD/HT analysis.

The POD basis is completely data driven, makes no a-priori assumptions about the data structure, and captures more statistical variance than any other basis. The technique allows ordering the modes in terms of decreasing energy content. By projecting the Navier–Stokes equations onto these modes, low-dimensional ordinary differential equation models are obtained for the fluid flow, as described by Smith *et al.* [11]. This way the flow field is characterized in terms of its most "energetic" characteristic modes (eigenmodes), and its lower dimensional approximation is obtained in terms of a significantly reduced number of coefficients. Tennekes and Lumley [12] estimated that the number of degrees of freedom (DOF), n, of a 3-D turbulent flow scales as $n \sim Re^{9/4}$. This would suggest that a very large number of DOF would be necessary in order to accurately analyze an application subjected to a turbulent flow with a large Reynolds number, such as the cabinets studied in this paper. POD techniques are used to reduce the data with a large DOF obtained from detailed CFD/HT simulations into a model with a significantly smaller DOF. The system domain Ω is decomposed into a series of fundamental modes and an approximate state is obtained by using the expansion theorem:

$$\vec{u}(\vec{x}) = \sum_{i=1}^{m} a_i \vec{\varphi}_i(\vec{x}) \tag{4}$$

The Galerkin method converts a differential equation to a problem of high dimensional linear system of equations, which may then be projected to a low dimensional system. When the basis functions are used in a Galerkin procedure, they yield a finite-dimensional dynamical system with the smallest possible degrees of freedom (DOF).

1.4 Scope and Objectives of Study

The objective of the research work described in this thesis is to present an approach for the thermal modeling of complex power enclosures such as the power conversion module cabinets. Such cabinets rely on forced convection air cooling. The architecture of the cabinets and the air-to-water-cooled packaged heat exchangers they employ for heat rejection are described in detail in Chapter 2. The overall approach to the cabinet thermal modeling consists of a detailed analytical model (Part 1) for the bottom bay containing the packaged heat exchanger and the return-air fan assembly; and a compact model (Part 2) of the upper four power-electronics bays based on their CFD/HT simulation data (See Chapter 3). The CFD/HT models are used to predict the airflow characteristics, the heat transfer mechanism and ultimately the component junction temperatures. A compact model for the entire cabinet is developed by coupling the two compact models. This high-fidelity modeling approach is specially suited as the present research program requires the resulting cabinet compact model to be linked to independent design and optimization tools.

CHAPTER 2

THE PHYSICAL SYSTEM

The systems of interest consist of two Power Conversion Module (PCM) cabinets called PCM-1 and PCM-2. Those PCM cabinets are used to distribute power in various zones in the Navy's next generation of battle ships. Those warships are envisioned to be highly dependent on electric power, since every single system aboard for instance the electric drive propulsion, weapon, communication and navigation systems will be electrically powered. All-electric ships will have comparable performance of today's mechanically driven ships as well as reduce the owner's life cycle cost. The demand in electric power for this future generation of all-electric warships is projected to reach 100 MW [1].

2.1 Integrated Power System (IPS)

Today's ships are designed with separated mechanical propulsion and electric power systems. As shown below, typical warships include multiple gas turbines per shaftline coupled with other power generation turbines dedicated to the ship service load.

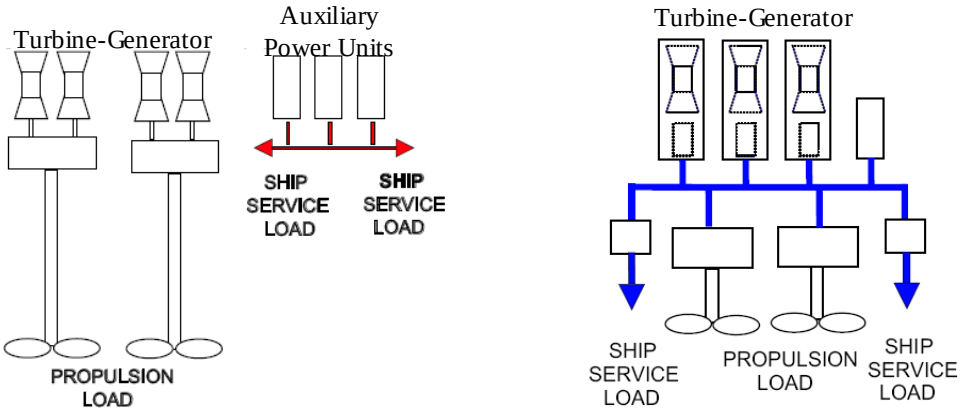

a) Existing Power System b) Future IPS

Figure 6: Ship Power Systems [26]

These systems have shown their limits through the years. A lack of flexibility and capacity to maintain power during combat missions have pushed designers to replace such systems with more reliable and efficient electromechanical systems. The development of high power switches and variable frequency motor drives have made AC propulsion motors more attractive, since they allow better control of motor current, noise and vibrations. Next generation of commercial and military ships are built with turbine generators, which provide power to the electrical propulsion motors mounted most of the time in external pods [26]. The turbine generators also provide power to the entire ship electric load. The result is a complex and reliable electric generation and storage system coupled with a power management and distribution network. This architecture is able to ensure power supply continuity for the ship electric load, enhancing the reliability and survivability of the ship power system. Such power system architecture is known as an Integrated Power System (IPS). The IPS consists of advanced power electronics, inverters, rectifiers and converters, such as the PCM cabinets.

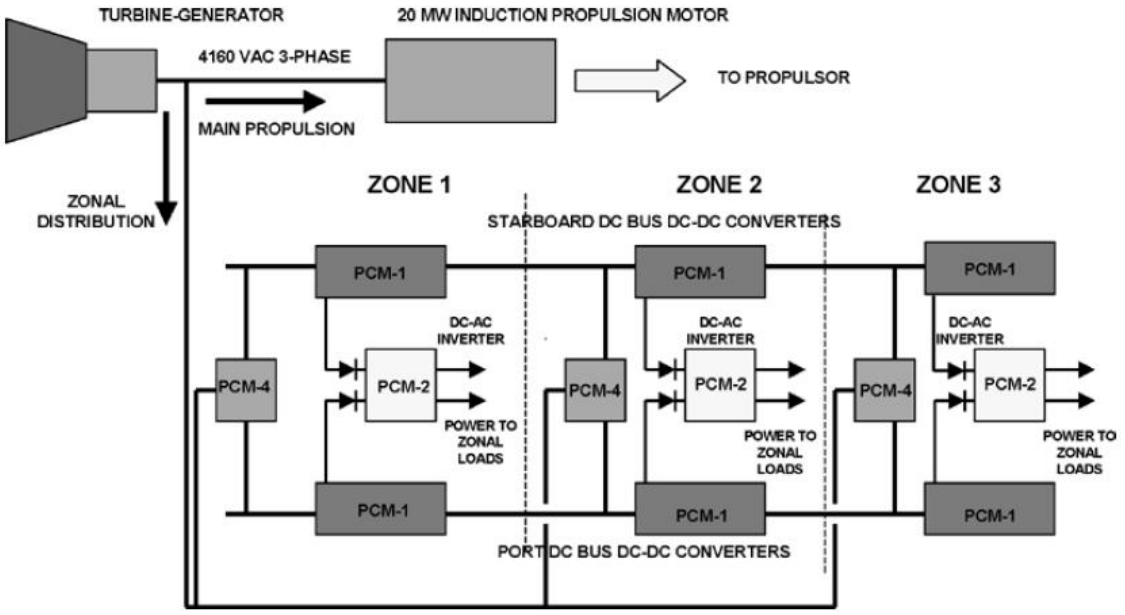

Figure 7: Zonal IPS Architecture [26]

Figure 7 illustrates a multi-MW IPS architecture basis for future systems that will be used in all-electric warships. Electric power is generated by a turbine in order to drive one or more propulsion motors and the various zone loads. Then a power conversion composed of multiple PCM cabinets change one form of electric power to another form. PCM-4s convert AC to DC, PCM-1s reduce the DC level and PCM-2s invert DC to AC for local loads [26].

2.2 PCM-2 (SSIM) Cabinet

2.2.1 Description

The PCM-1 power electronic cabinet is 1.98 m (78”) high, 1.22 m (48”) deep and 0.61 m (24”) wide. It is divided into 5 bays. Figure 8 illustrates a right side view of the PCM-2 cabinet. It is shown that the upper four bays are filled with various power electronic components. Those 4 bays are identical. Each of these bays forms the Ship Service Inverter Module (SSIM).

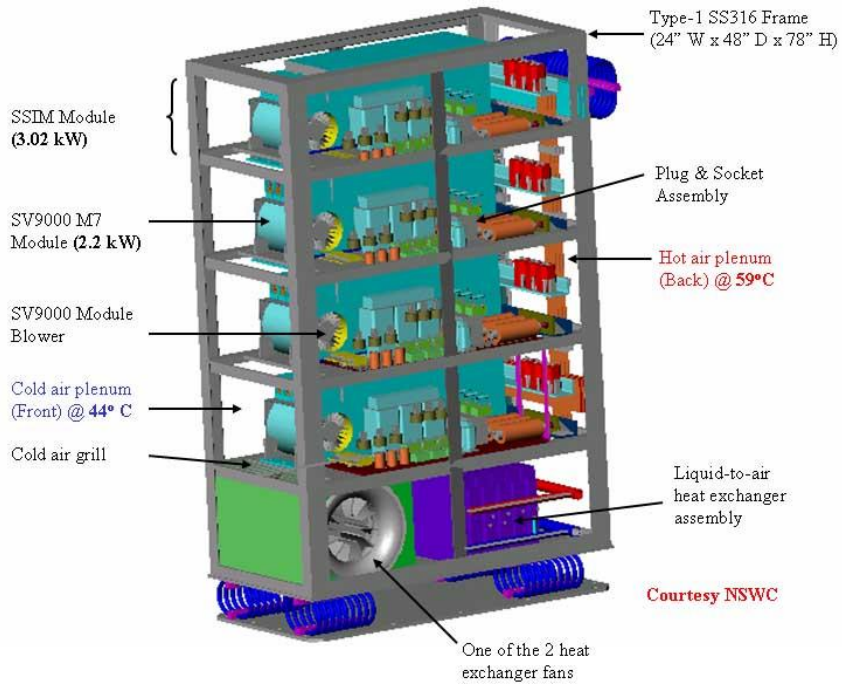

Figure 8: PCM-2 [27]

Table 3 lists the various SSIM electronics and the resultant heat losses. The SSIM major hardware includes components such as the SV9000 module, filters, fuses and fans. From the description given in [27], it appears that only the major heat producing SSIM components are listed. In other words, this list of SSIM components is certainly not exhaustive. The total heat dissipation generated by the 16 electronic components of each SSIM reaches 3.02 kW at a 100% rated output. Heat losses per electronic part range from 7 W to 2200W. The heat load of the entire hardware enclosed within the top four bays is estimated to be 12.09 kW. It was reported in 2004 that typical data processing and communication (Datacom) equipments may exceed 20 kW per rack and a heat load density of 5 kW/ft^2 [28]. Actual predictions estimate a power density of 8 kW/ft^2 by 2014. Therefore with a 1.5 kW/ft^2 power density and 3.5 tons of refrigeration (12.9 kW) the SSIM cabinet is well under the actual datacom power trends. However, with

development of IPS architecture, a substantial increase in the heat dissipation of the PCM cabinets can be expected in the future.

Table 3: Heat Losses of SSIM Components [27]

SSIM Components	Heat Loss (W)	Number of Units	Total Heat losses (W)
SV9000	2200	1	2200
Blower - SV9000	190	1	190
Control board	25	1	25
Output inductor	200	1	200
Dampening inductor	16	1	16
EMI filter (input)	50	1	50
DC contactors	7	2	14
DC fuse	20	1	20
AC contactor	9	3	27
AC fuse	10	3	30
EMI filter (output)	50	1	50
Miscellaneous	200	-	200
Total	-	16	3022

2.2.2 SV9000 Module for SSIM

The SV9000 module is responsible for 73 % of the total heat dissipation of the SSIM. The SV9000 is a new generation of integrated power converter based on insulated bipolar transistors (IGBT) power modules. Devices with such heat losses have to operate in high temperature environments, typically above 100°C, and are susceptible to failure as a consequence of high thermal constraints.

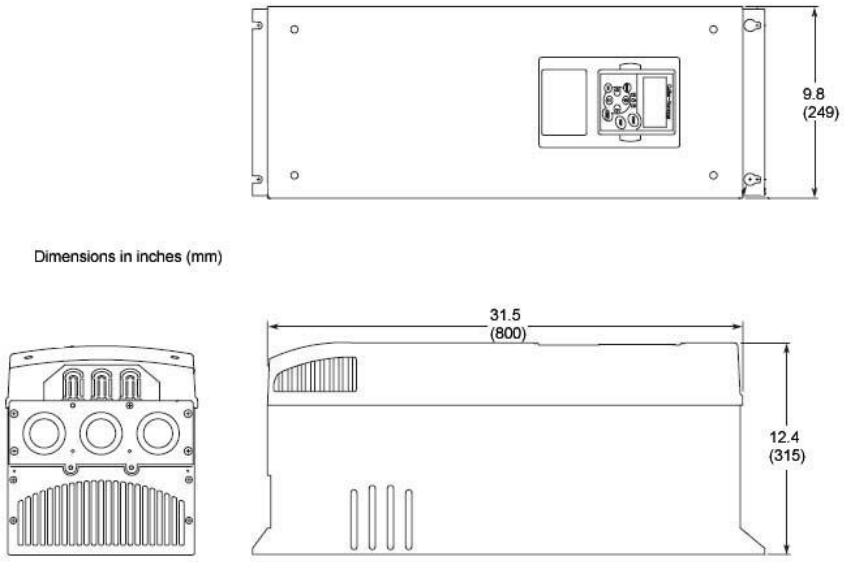

Figure 9: SV9000-M7 Frame Dimensions

Figure 9 gives the dimensions of the SV9000-M7 frame module. It is 24.9 cm (9.8") wide x 80 cm (31.5") deep x 31.5 cm (12.4") high. This 125 Hp module used for the SSIMs is the largest single inverter frame available in the SV9000 family and weighs 133 lbs. The photograph below illustrates the actual power-electronics packaged within the SV9000-M7 module used within the SSIMs.

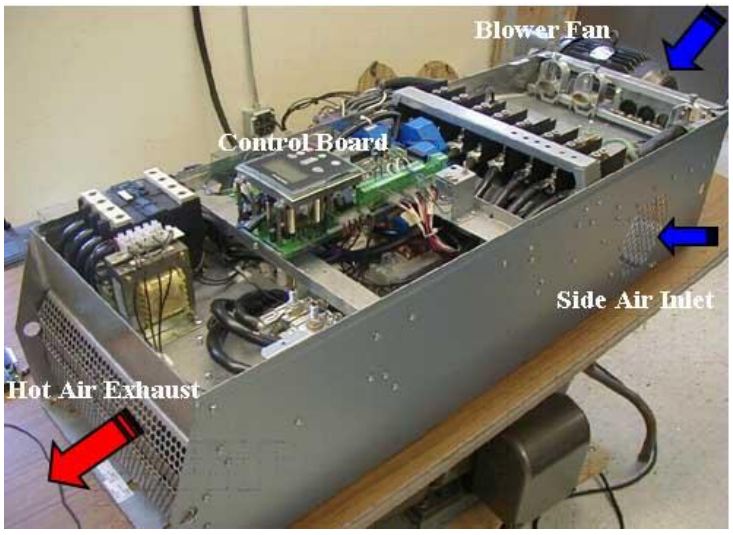

Figure 10: SV9000-M7 frame for SSIM (PCM-2) Cabinet [27]

The actual centrifugal blower located at the front of the SV9000 module is illustrated in Figure 10 and Figure 11. The cold air from the supply plenum enters the module through the air inlets located on both sides. The blower thrusts the cold air into the SV9000 module, before being rejected in the back of the unit.

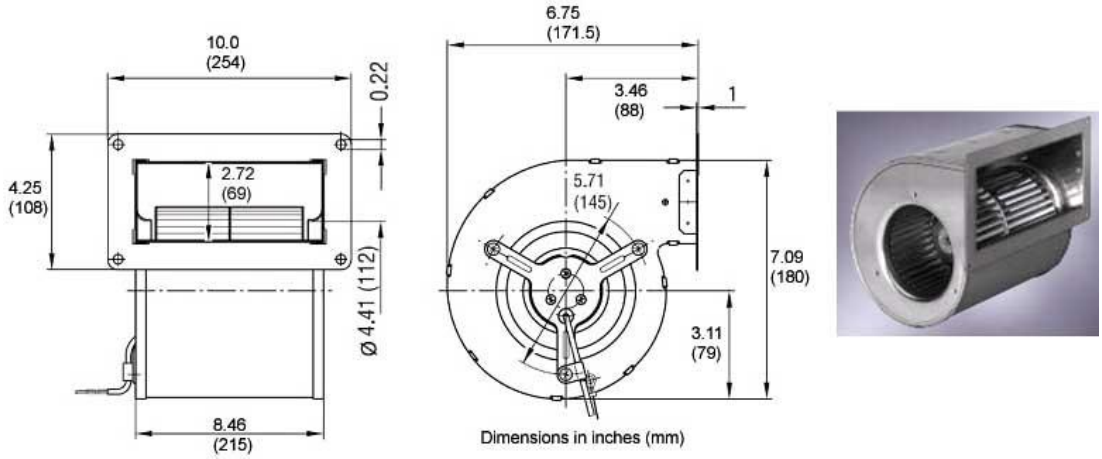

Figure 11: Centrifugal Blower (Model# D2E133) of SV9000-M7

Air enters through 133 mm diameter dual inlets by means of the centrifugal force generated by rotating a cylindrical runner on which blades have been arranged. These fans are used for intensive cooling application. They create larger static pressure than axial fans and larger airflow rate, making them optimal for cooling equipment through which air cannot easily flow. Also, this blower dissipates 190 W of heat. Characteristics of the blower and fan curve are obtained from the manufacturer, Ebm-Papst. Figure 12 shows the fan performance curve for model # D2E133.

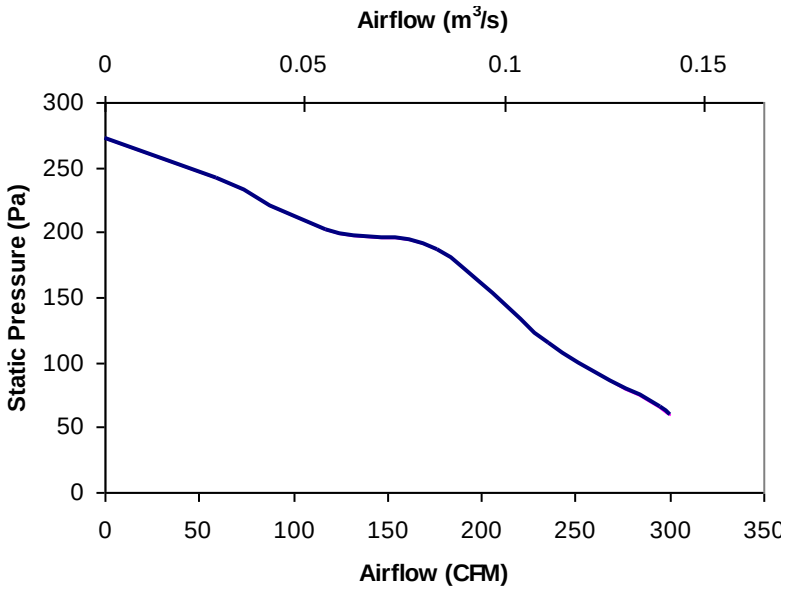

Figure 12: Blower (Model# D2E133) Pressure Drop vs Air Flow Rate

The cooling fan is rated at an air flow rate of 0.142 m^3/s (300 CFM) at 54 Pa. The packaging of the SSIM module is set up not to block the SV9000 blower air inlets. The heat load of the SV9000 including the blower is given as 2390 W in the SSIM heat load summary. The required air flow rate for cooling the SV9000 module is obtained with the following correlation:

$$Q_{SV9000} = \Delta T_{air}\ \rho_{air}\ \dot{v}_{air}\ C_{p\,air} \qquad (5)$$

where Q_{SV9000} is the heat load in W, ΔT is the temperature change in °K, $\dot{v}_{air}$ is the air flow rate in m^3/s, the ρ density in kg/m^3, and C_p the specific heat in J/kg.°K. The minimum airflow rate for a maximum temperature rise of 15°K is 0.141 m^3/s (299.3 CFM).

2.2.3 PCM-2 Cooling

The PCM-2 cabinet is sealed, so no air is transferred to the outside environment. Forced air convection is used for the cooling of the power electronics. The internal air

cooling flow consists of a closed air loop. Heat is dissipated by the power electronics within the top 4 bays and transferred to the air coming from the front of the cabinet (the cold air plenum). The air flow is directed to the return located in the back of the cabinet, the hot plenum. The hot air circulates through a heat exchanger assembly located in the bottom bay of the cabinet. Figure 13 illustrates the heat exchanger bay. The heat exchanger assembly for the SSIM cabinet consists of 5 tube-fins air-to-liquid heat exchangers manufactured by Lytron. More details regarding the heat exchanger assembly is given in the next paragraph.

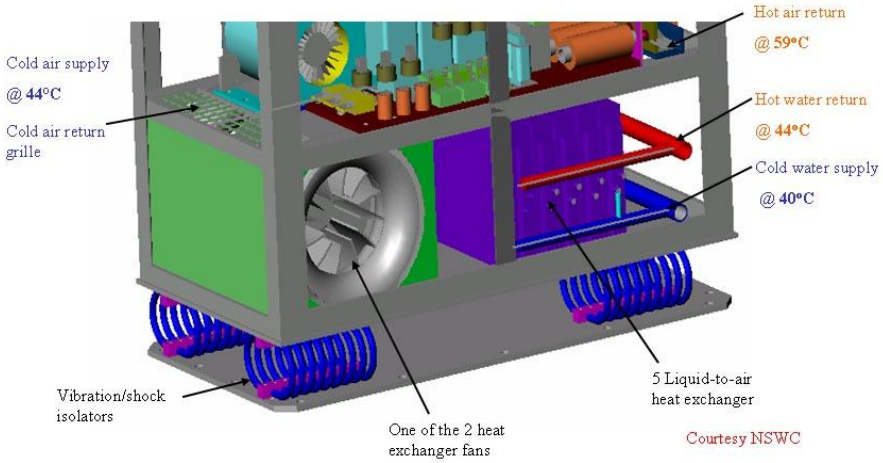

Figure 13: PCM-2 Heat Exchanger Bay [27]

The cooling fluid of this cross flow heat exchanger is a mixture of 80% water and 20% ethylene glycol [27]. The 40°C cold mixtures enters the bottom bay though the cold water supply pipe. The heat dissipated by the components is removed by the series of air-to-water heat exchangers. The hot water is then rejected from the cabinet through the hot water return located in back of the cabinet. The air, cooled down by the heat exchanger, is forced by the fan bank into the upper SSIM bays through the cold plenum. The following figure illustrates the closed air loop cooling process of the PCM-2 cabinet.

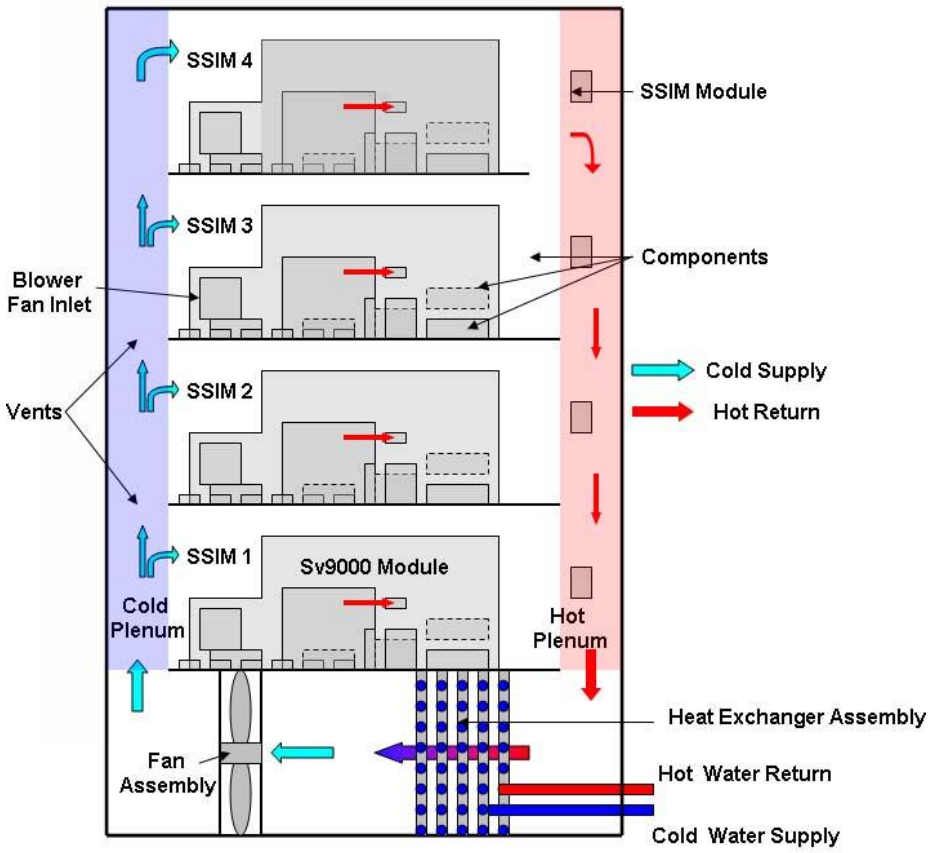

Figure 14: Cooling Process within PCM-2

The blue arrows represent cold air coming out of the heat exchanger bay. This cold air flow is then distributed to the various SSIM through the cold plenum before cooling down the various SSIM components.

The heat exchanger selected is a Lytron model# 6320 air to liquid tube-fin heat exchanger. This model made of copper tubing and fins is 30.5 cm (12") high, 58.2 cm (22.9") wide and 5.3 cm (2.1") deep. Figure 10 illustrates this heat exchanger and gives its thermal performance. This model comes with a built-in fan-ready mounting plate. However, if the fan is placed too close to the heat exchanger, the effective size of the heat exchanger is reduced to the size of the fan. Therefore. placing the fan(s) at a correct distance ensures that the air is distributed on the entire face of the heat exchanger.

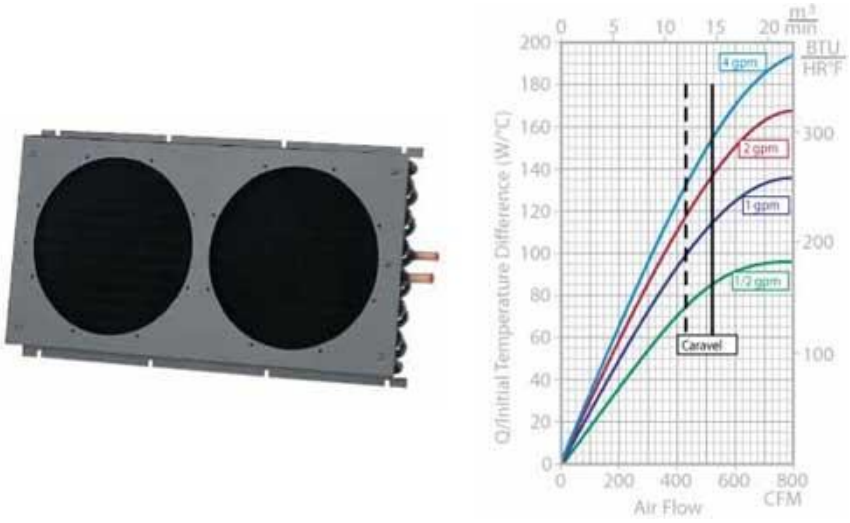

Figure 15: Lytron Heat Exchanger model# 6320 and its Thermal Performance [29]

The Lytron Heat Exchanger model# 6320 was pre-selected by the designers due to its physical characteristics. Several of these heat exchangers are put in parallel to form the heat exchanger assembly described in Figure 13. In order to select the proper number of heat exchangers, it is important to first determine the cooling requirement of the system as described in [29]. The first step it to calculate the initial temperature difference (ITD), or the difference between the air return temperature and the water supply temperature as shown below:

$$ITD = T_{air\ out} - T_{wat\ in} = 19°C \quad (6)$$

The performance capability (PC) is calculated for the heat exchanger selection.

$$PC = Qcabinet / ITD = 636.2\ W/°C \quad (7)$$

PC is defined as the ratio of the heat load $Q_{cabinet}$ to the ITD. For a water flow rate of 2 - 4 gpm (7.57 - 15.14 liter/min) and an air flow rate of 550 - 650 CFM (0.260 – 0.307 m^3/s), this heat exchanger's performance capability exceeds 160 W/°C. The number of heat exchanger can be now determined as:

$$N_{HX} = PC_{PCM-2} / PC_{HX6320} = 5 \quad (8)$$

The ratio of the cabinet PC to the heat exchanger PC indicates that 5 Lytron's 6320 heat exchangers mounted in series on the air side will be necessary to remove the

12.09 kW of heat loss from the PCM-2 cabinet under the prescribed conditions. The water flow rate for this design is 2.5 gpm (9.46 liter/min) per heat exchanger. Since the 5 heat exchangers are mounted in parallel on the water side the total water flow rate for this heat exchanger assembly is $\dot{v}$ = 12.5 gpm (47.32 liter/min). Assuming that the entire 12.09 kW of heat is absorbed by the coolant, the return temperature can be calculated using Equation 4. The water temperature rise is estimated as approximately 4°C. The inlet water temperature of 40°C is a predetermined design parameter of the systems studied, so the water return temperature is 44°C. On the air side, the maximum temperature of hot return for this design is 59°C. In order to obtain a maximum air temperature rise of 15°C, the required air flow rate for this PCM-2 cabinet is then 1418 CFM or 354.3 CFM per SSIM. Figure 14 summarizes the various flow properties of the design cooling process of PCM-2 cabinet.

2.3 PCM-1 (SSCM) Cabinet

The PCM-1 cabinet converts a higher DC input to a lower DC voltage output within the IPS. The PCM-1 cabinet is similar to PCM-2 cabinet in size, configuration and overall thermal management approach.

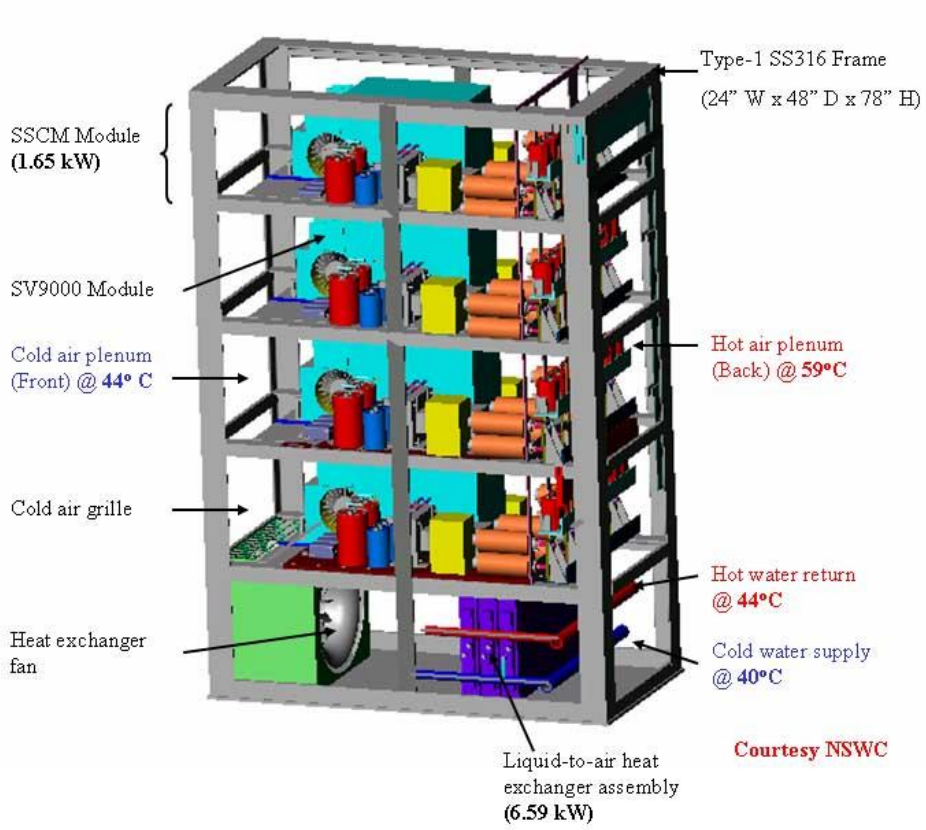

Figure 16: PCM-1 Solid Model [27]

As shown in Figure 16, both cabinets use a SS316 frame, have the same dimensions (1.98 m x 1.22 m x 0.61 m) and are divided into five bays. The power electronics located within each of the top 4 bays form the Ship Service Converter Module (SSCM). The bottom bay is also dedicated to cooling purpose. Table 4 lists the major heat producing power electronics that form the SSCM.

Table 4: Heat Losses of SSCM Components [27]

SSIM Components	Heat Loss (W)	Nbr of Units	Total Heat losses (W)
SV9000	864	1	864
Fan – SV9000	190	1	190
Control board	25	1	25
Output inductor	40	1	40
Dampening inductor	16	1	16
Dampening capacitor	50	2	100
Dampening resistor	7	1	7
EMI filter inductor (input)	50	1	50
DC contactor (input)	7.5	2	15
DC fuse (input)	26	1	26
Voltage LEM (input)	10	1	10
Voltage LEM (output)	10	1	10
DC contactor (output)	10	2	20
AC fuse (output)	8	3	24
EMI filter inductor (output)	50	1	50
Miscellaneous	200	-	200
Total	-	16	1.65 kW

The heat dissipation per SSCM electronic component ranges from 7 to 864 W, nd the total heat dissipated within each SSCM reaches 1.65 kW. Similarly to the SSIM, the SV9000 is responsible for the major part (64 %) of the heat loss within this module. As shown in Figure 17, the SV9000-M6 frame is 22.1 cm (8.7”) wide x 61.7 cm (24.3”) deep x 29.0 cm (11.4”) high and weighs 38 kg (83.8 lbs) which is much smaller than the SV9000-M7 frame used in the SSIMs.

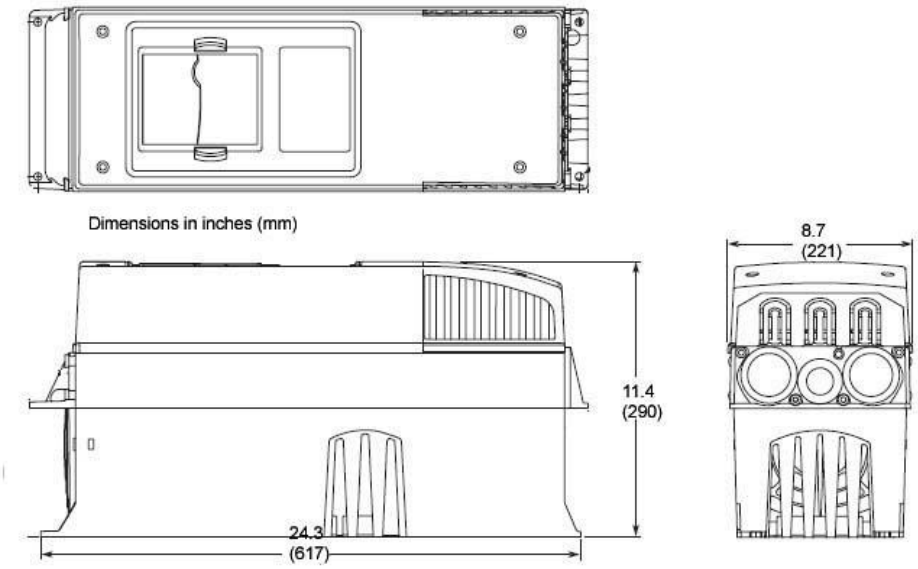

Figure 17: SV9000-M6 Frame Dimensions

Figure 18: Axial Fan (Model# MC24B3) of SV9000-M6

Since the heat dissipated by the SV9000 within the SSCM is much lower than for the SSIM, the internal cooling fan and the airflow rate within the module is much smaller. Figure 18 illustrates the fan manufactured by Comair Rotron used for cooling the SSCM. It is 0.12 m (4.72 in) wide x 0.12 m (4.72 in) high x 0.3 m (1.25 in) deep axial fan with a maximum flow rate of 0.047 m^3/s (100 CFM) at a 0 Pa static pressure, as shown by the fan curve illustrated by the following figure.

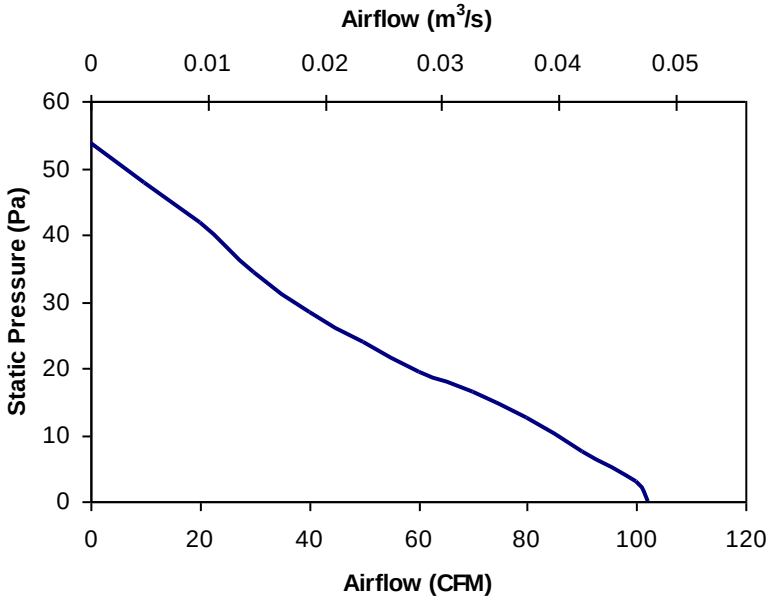

Figure 19: SV9000 M6 Fan Curve

The total PCM-1 cabinet heat loss is then 6.59 kW, which is just over half that of the PCM-2 cabinet. Consequently, the cooling requirement is much lower for the PCM-1 cabinet. The fan/heat exchanger bay is therefore different than the one used in the PCM-2 cabinet. The same Lytron 6320 heat exchangers are used for the air-to-liquid heat exchanger assembly. Using the method described previously for PCM-2, 3 heat exchangers with air in cross-flow are necessary to remove the 6.59 kW heat load.

CHAPTER 3

ANALYSIS METHODOLOGY

Due to the flow complexity within the power cabinets CFD/HT models are used to investigate the flow behavior and the thermal performance of the systems. The difficulty with such modeling approach is related to the multi-scale nature of the system. CFD/HT models of package-level or system-level electronics thermal- fluid problem require high meshing resolution to predict sharp gradients accurately within the system. The smallest length scale within the power cabinets dictates the grid size of the system-level CFD/HT model and results in extremely large mesh that is computationally impossible to solve. Resolving such large numerical models using commercially available codes, results in extremely large processing time and slow convergence limiting the thermal analysis to a few number of system observations. In this section, a methodology is introduced for an efficient modeling of the PCM-1 and PCM-2 cabinets. Both cabinet model are divided into the three parts, modeled separately interfacing together. An analytical model of the bottom bay, two CFD/HT models of the upper four bays and the IGBT multi-chip power module with its heat sink are developed.

3.1 Heat Exchanger Model

The cabinet manufacturer uses the ITD as a design parameter for selecting an HX model and the size of HX bank. This method for defining performance of the bottom bay appears to be too simplistic to capture accurately the heat load removal and pressure drop. A more detailed analysis is given in the following section. Since the performance data for the fan and heat exchangers are available, an analytical model is developed by

Haider *et al.* [30] to predict the bulk flow properties in the bottom bay using standard correlations.

3.1.1 Temperature Change Calculations

Four performance functions, f_1, f_2, f_3, and f_4 are developed to predict the heat transfer and pressure drop characteristics of each heat exchanger unit and the pressure head characteristics of the return air fan unit. The model takes in account the effect related to different number of heat exchanger units (N_{HX} = 3 for PCM-1, N_{HX} = 5 for PCM-2) and return air fans (N_f = 1 for PCM-1 and N_f = 2 for PCM-2). At 100% operating point, the heat loads of the SSIM and SSMM module are defined as Q_m = 1.635 kW for PCM-1 and Q_m = 3.02 kW for PCM-2, respectively [27]. The overall cabinet heat load can be evaluated as:

$$Q = 4Q_m + N_f Q_f \tag{9}$$

where Q_f is the fan heat dissipation (560 W) and N_f is the number of fans within the bottom bay. This leads to an overall cabinet load of 7.1 kW for PCM-1, and 13.2 kW for PCM-2. The cabinet heat load is assumed to be entirely removed by the fan-heat exchanger assembly and is defined as the sum of the unknown heat duties of each heat exchanger units:

$$Q = \sum_{i=1}^{N_{HX}} Q_i \tag{10}$$

The heat removed by each heat exchanger unit, Q_i, is calculated using the standard counter-flow log mean temperature difference (LMTD). LMTD is widely used to determine the temperature driving force for heat transfer in flow systems. It consists of taking the logarithmic average of the temperature difference between the hot air and water at the boundary of each heat exchanger unit [30]:

$$LMTD = \frac{Q_i}{F_{HX} UA_{HX}} = \frac{\left[\left(T_{a,in}\right)_i - \left(T_{w,out}\right)_i\right] - \left[\left(T_{a,out}\right)_i - T_{w,in}\right]}{\ln\left(\frac{\left(T_{a,in}\right)_i - \left(T_{w,out}\right)_i}{\left(T_{a,out}\right)_i - T_{w,in}}\right)} \quad (11)$$

where $T_{w,in}$ is the known water inlet temperature (40°C), $(T_{w,out})_i$ is the unknown water outlet temperature, $(T_{a,in})_i$ and $(T_{a,out})_i$ are the unknown air inlet and outlet temperature of the ith heat exchanger unit. F_{HX} is the coefficient for the present flow configuration and is assumed to be 0.97 for all HX units as suggested in [31]. The overall conductance value, UA_{HX}, assumed to be constant for each HX unit, is estimated as a function of the air and water volumetric flow rates using a curve-fit of the thermal performance illustrated in Figure 15:

$$UA_{HX} = f_1(v_a, v_w) \quad (12)$$

The temperature change in the air and water at the boundary of each HX unit is determined using the following heat balance equation:

$$\rho_a v_a c_{p,a}\left[\left(T_{a,in}\right)_i - \left(T_{a,out}\right)_i\right] = \rho_w v_w c_{p,w}\left[\left(T_{w,out}\right)_i - T_{w,in}\right] \quad (13)$$

The air inlet temperature of a HX unit is defined as the air outlet temperature of the preceding HX unit as shown below:

$$\left(T_{a,in}\right)_{i+1} = \left(T_{a,out}\right)_i \quad \text{for } 1 \leq i \leq N_{HX} - 1 \quad (14)$$

As stated before the entire cabinet load is assumed to be removed by airflow within the enclosure, which leads to following equation:

$$Q = \rho_a v_a c_{p,a}\left[\left(T_{a,in}\right)_1 - \left(T_{a,out}\right)_{N_{HX}}\right] \quad (15)$$

The set of relations described in Equation 9 to Equation 15 are used to solve the air and water flow properties at each HX unit. It is important to note that constant air and water properties atmospheric pressure are used for these calculations.

The outlet temperature of the bottom bay is calculated is obtained by adding the temperature of the air leaving the HX bank and entering the fan assembly with the heat dissipation from the fan's electric motor.

$$T_{f,a,out} = T_{f,a,in} + \frac{N_f Q_f}{\rho_a v_a c_{p,a}} \tag{16}$$

3.1.2 Pressure Change Calculations

The model developed predicts also the pressure drop within the bottom bay. The function f_2, defining the air pressure drop through each HX unit, is obtained from the total air pressure drop across the HX bank as follows:

$$\Delta p_{HXB,a} = N_{HX} f_2(v_a) \tag{17}$$

where $\Delta p_{HXB,a}$ is the HX bank air pressure drop obtained from the manufacturer. The rectangular plenum between the HX bank and the fan assembly has a cross section of 0.610 m x 0.386 m and a hydraulic diameter D_h of 0.473 m for both cabinets. The plenum length L is 0.500 m for PCM-1 and 0.287 m for PCM-2. The air pressure drop in the bottom bay along this plenum from the heat exchanger bank outlet to the fan assembly inlet is calculated by using the Darcy equation as follows:

$$\Delta p_{pl,a} = f \frac{L}{D_h} \frac{\rho_a u_a^{\,2}}{2} \tag{18}$$

where u_a is the normal flow velocity, and f is the turbulent friction factor. f was evaluated using the following Colebrook equation [32] recommended for turbulent flow with Re > 4000:

$$\frac{1}{\sqrt{f}} = -2\log_{10}\left[\left(\frac{\varepsilon/D_h}{3.7}\right) + \frac{2.51}{\mathrm{Re}\sqrt{f}}\right] \tag{19}$$

where the Reynolds number, Re, is based hydraulic diameter and the wall roughness, ε, is assumed to 0.05 mm as suggested in [33]. The pressure head, $\Delta p_{f,a}$, obtained from the test data of the manufacturer, helps to determine to performance curve, f_4, of the EBM/PAPST backward curved AC Impeller fan Model RH35M-4/205407.

$$\Delta p_{f,a} = f_4\left(\frac{v_a}{N_f}\right) \tag{20}$$

The total pressure change across the bottom bay is then obtained with:

$$\Delta p_{bb,a} = \Delta p_{f,a} - \left(\Delta p_{HXB,a} + \Delta p_{pl,a}\right) \tag{21}$$

In a similar way than the air pressure drop calculations, the water pressure drop across each HX is evaluated. The function f_3, defining the water pressure drop through each HX unit is obtained as follows

$$\Delta p_{HXB,w} = f_3(v_w) \tag{22}$$

where $\Delta p_{HXB,w}$ is the HX bank water pressure drop obtained from the manufacturer.

3.2 Top 4 Bay CFD/HT Modeling

CFD/HT analysis essentially consists of the following steps: geometry creation, meshing, solving, and post processing. Figure 1 gives an illustration of the procedure done in order to achieve the cabinet modeling.

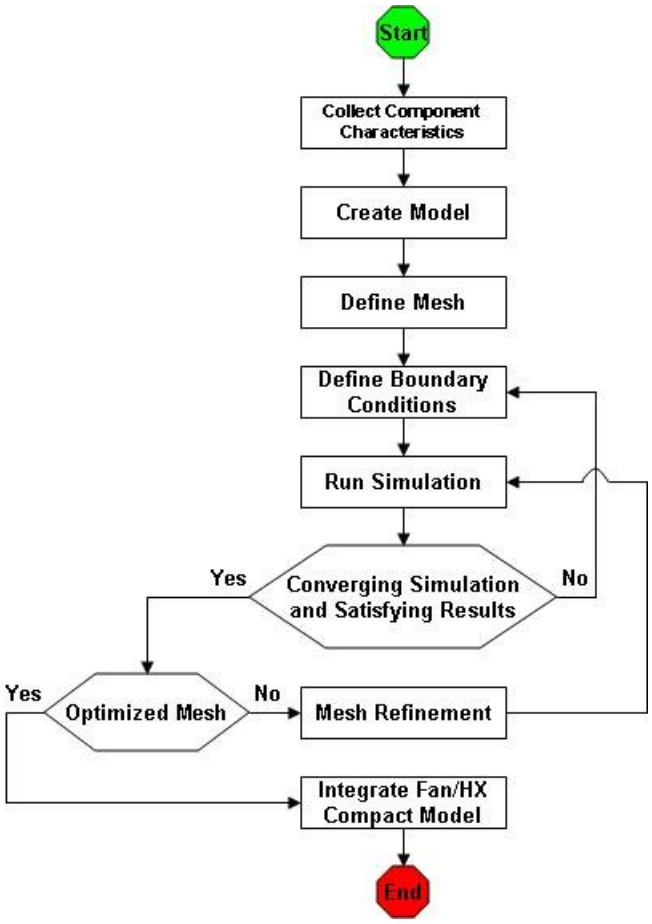

Figure 20: Cabinet Modeling Flow Process Chart

The key to an efficient finite element analysis is frequently an effective mesh. Geometric modeling and grid generation are the required preprocessing steps for conducting the CFD/HT analysis of the IPS cabinets. Creating a mesh is one of the most complex steps in a CFD/HT analysis. Therefore particular attention must be payed to discretizing the domain into small enough volumes. Traditionally, detailed geometric models are imported from a CAD system and the mesh of the model is created within a separate grid generator, such as Gambit. This way, the geometry is built only once. Such a direct import of product geometry from a CAD package to a grid generator is very useful in a product design cycle. While it is certainly a very elegant concept, however, it is known that the data transfer between a CAD system and a grid generator is error-prone, and a great deal of time is spent on fixing the errors to make the model geometry suitable

for grid generation. Since the smallest length scale dictates the grid size, a detailed geometry of these electronics components will significantly increase the demands on the computational resources and it will boost the time required to obtain the simulation solutions. Despite modern developments in computer technology, computational resources still limit the mesh size along with the complexity of electronic system models.

The other way to create a compact model is to manually build the cabinet geometry from scratch in a mesh generator, such as Gambit. Since detailed CAD drawings of the cabinet were not available, simplified compact models of the cabinets were made as described. Despite the lack of geometrical information regarding the cabinet provided in [27], a considerable effort was done before building the compact model to collect as much as possible details regarding every electronics component from the manufacturers. Special attention was made to refine the grid when the model was built the quality of the mesh is of highest importance in large, complex multi-scale electronics systems such as this one. The mesh needs to be refined in areas of sharp gradients, yet could be coarse enough to keep the problem solvable with the computational resources available and attain convergence in a convenient amount of time. The adaptive mesh refinement is a process in which an appropriate grid cell repartition is assigned, based on the geometry of the model and the characteristics of the flow field experienced. In other words, the mesh is optimized for this specific application by devoting particular consideration to zone experiencing high flow complexity by refining the grid and adding more cells. As a result, more computational efforts are assigned to this region. On the contrary, regions that have no crucial effects on the flow field are meshed with sufficient number of cells to capture the essential features of the flow field. Several assumptions were made to complete the PCM cabinet compact models:

- The material and flow properties are assumed to be constant and temperature independent.
- Buoyancy effects are neglected since it s a forced convection system.
- Since the system Reynolds number based on the inlet condition is larger than 50,000, the flow field is assumed to be turbulent within the cabinet.
- The $k - \varepsilon$ turbulent model is used.
- The various components are considered as aluminum cuboid blocks with uniform properties.
- Wires providing power and connecting the various components are neglected for simplification purposes.
- Heat losses due to radiation are neglected. Only conduction and convection heat transfer are considered.
- Since the cabinets are sealed, no heat is transferred to the ambient (multi rack zone). Therefore the cabinet external walls are assumed to be adiabatic.

Omission of any component from the bay modules would have some effect on the flow solution and the convective heat transfer coefficients. For this reason, all the components within the SSIM and SSCM modules are included in the CFD/HT model. The first step in the creation of the 3-D CFD/HT compact models is to collect information regarding the various components within the PCM-1 and PCM-2 cabinet. All the components were modeled as aluminum cuboid blocks with a 0.05 mm roughness. Each of these blocks was given a uniform volumetric heat generation, calculated from the dimensions and heat losses communicated by the manufacturers.

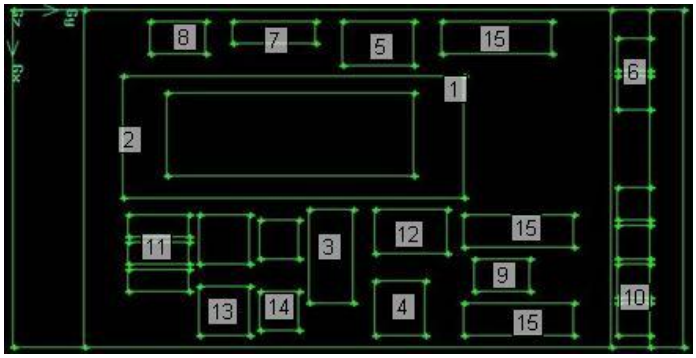

(a) Top View

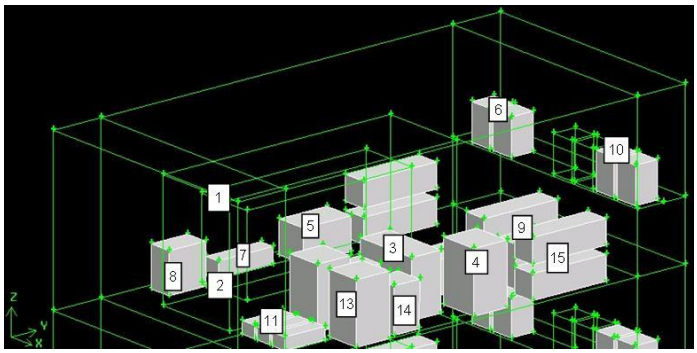

(b) Isometric View

Figure 21: SSCM Geometries in Gambit

Figure 21 illustrates the top and isometric views of a SSCM module in Gambit. The various electronic components within the module can be seen. Table 5 lists the characteristics of the labeled components. The SSCM model is composed of 26 components, with a total heat dissipation of 1,610 W. At the PCM-1 cabinet level, a total number of 104 components are represented, with a total heat loss of 6,440 W.

Table 5: Components within SSCM

		Dimensions (cm)			Heat Dissipated		Number of Units	Total Heat Loss
#		W*	D*	H*	(W)	(W/m3)	Units	(W)
1	SV9000 M6	22	62	29	864	21877	1	864
2	Fan (SV9000)	22	17	18	190	28543	1	190
3	Output inductor	8	17	14	40	20628	1	40
4	Dampening resistor	5	11	10	7	11959	1	7
5	EMI filter inductor –in	13	8	8	50	61394	1	50
6	DC contactors (input 2)	6	6	8	8	30617	2	15
7	DC fuse – input	4	15	4	26	107281	1	26
8	Voltage LEM – Vin	10	10	6	10	16667	1	10
9	Voltage LEM – Vout	10	10	6	10	16667	1	10
10	DC contactor (output 2)	6	6	9	10	34440	2	20
11	DC fuse (out-3)	3	11	4	8	68287	3	23
12	EMI filter inductor-out	15	10	9	50	34420	1	50
13	Dampening capacitor	9	9	15	50	41152	2	100
14	Capacitor 1	7	7	11	25	46382	2	50
15	Capacitor 2	6	20	6	21	28472	6	123
	Board	-	-	-	32		-	32
						Total	26	1610

As described in Chapter 2, the SSIM system is different from the SSCM. The following table lists the various components, their dimensions, and heat losses within each SSIM. A total number of 34 components and 3.07 kW of heat losses are simulated for each SSIM. At the PCM-2 cabinet level, a total number of 136 components are represented for a total heat loss 12.28 kW.

Table 6: Components within SSIM

	Dimensions (cm)			Heat Dissipated		Number of Units	Total Heat Loss
	W*	D*	H*	(W)	(W/m3)	(Units)	(W)
SV9000 M7	25	80	31	864	13774	1	2200
Blower (SV9000)	22	17	18	190	28543	1	190
Output inductor	9	26	21	200	42040	1	200
Dampening inductor	5	11	10	16	27335	1	16
EMI filter-in	7	11	7	50	90718	1	50
DC contactors (2)	6	6	9	7	24108	2	14
DC fuse	4	15	4	23	94902	3	69
AC contactor (output 3)	6	6	9	9	30996	3	27
AC fuse (3)	3	11	4	10	89070	3	30
EMI filter-out	8	13	10	50	48533	1	50
Misc 1	6	20	6	20.5	28472	5	102.5
Misc 2	4	5	3	10	305119	12	120
					Total	34	3068.5

As shown in Table 5 and Table 6, the SV9000 modules are the major source of heat in both PCM-1 and PCM-2 cabinets. Those units are complex power electronic devices. Unfortunately, only limited information is available regarding the various components and the flow distribution within those SV9000 modules. Therefore, the SV9000 modules are assumed as simple enclosures with a heated aluminum cuboid block inside.

The grilles located at the flow inlet and outlet of the module are assumed to be thin porous media whose pressure drop is defined as a sum of the Darcy's friction term and an inertial pressure loss term. From [34]the pressure drop across these grilles is defined as:

$$\Delta p_{SV9000} = -\left(\frac{\mu}{\alpha}u + \frac{C}{2}\rho u^2\right)t \qquad (23)$$

The inertial term in the above equation is inversely proportional to the porous medium permeability, α. Since the permeability is assumed to be infinite, the first term disappears. The pressure drop is therefore proportional to the dynamic pressure due to the flow velocity u normal to the porous face and C is defined as the static pressure drop coefficient per unit thickness t of the porous medium.

As described in the previous chapter, each SV9000 has a built in cooling fan. Fans are defined in the CFD/HT model as infinitely thin with a pressure rise across them. The pressure change across the fan is approximated as a quadratic polynomial function of the velocity normal to the face as shown by the following relation:

$$\Delta p_{Fan} = C_0 + C_1 u + C_2 u^2 \qquad (24)$$

The C coefficients are obtained from the fan curves provided by the manufacturer (illustrated by Figure 12 and Figure 19). The flow though the fan was modeled as only being normal to the face. Therefore, the tangential and radial flow velocity components of fan swirl are neglected.

3.3 IGBT Multi-Chip Power Module Model

Electrical characteristic and reliability of integrated power electronic modules (IPEMs) is highly dependent on the temperature distribution inside the module. The purpose of the following section is to extend the cabinet modeling work to the component level by developing an insulated gate bipolar transistor (IGBT) thermal model. An existing IGBT module tested and introduced by the National Institute of Standards and Technology in collaboration with the Center for Power Electronic Systems at Virginia Tech [25] is used for that purpose. Berning *et al* in [25] developed and experimentally validated IPEM CFD/HT model. The IPEM and heat sink system model was simulated under high power (1080-7700W) and short term (100 μs) heating conditions. This IPEM is investigated again in the present work in order to evaluate the temperature distribution and the cooling requirements of an IGBT multi-chip module subjected to power heating and operating conditions found within power cabinets such, as PCM-1 and PCM-2.

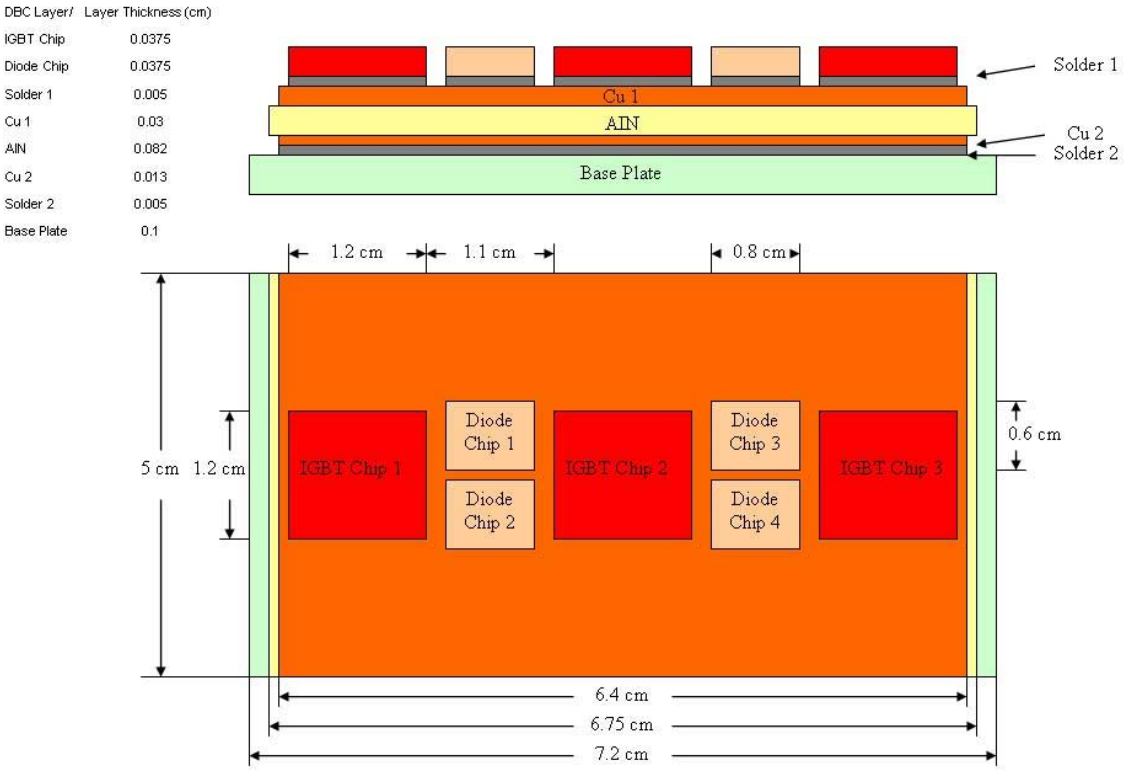

Figure 22: Physical properties of IGBT multi-chip module

A complete physical description of the IGBT multi-chip module is given in Figure 22. This IPEM consists of three silicon IGBT chips and four diode chips where heat is dissipated, a direct bond copper (DBC) layer and a base plate. The structure of the DBC layer is also illustrated in Figure 22. It can be seen that the DBC layer consist of two 0.005 cm solder layers, one 0.03 cm copper layer (Cu 1), one 0.082 cm aluminum nitride layer (AIN) and one 0.03 cm copper layer (Cu 2). The base plate is directly connected to a heat sink system.

The material properties for the various layer of the DBC are listed in Table 7.

Table 7: Material Properties for IGBT Module

	Specific Heat J/kg. °K	Thermal Conductivity W/m. °K	Density kg/m^3
Cu	390	400	8900
Solder	150	50	8500
AIN	820	150	3250
Silion	700	150	2330

During operation, cycling current and voltage are applied to the IGBT multi-chip module. The IGBT chips increase in temperature, and heat propagates through the DBC layers to the base plate and heat sink. A simplified 1-D thermal resistance network of the IGBT chip package and the equivalent thermal circuit were developed and are illustrated in Figure 23. In this 1D network, heat is assumed to be rejected only vertically.

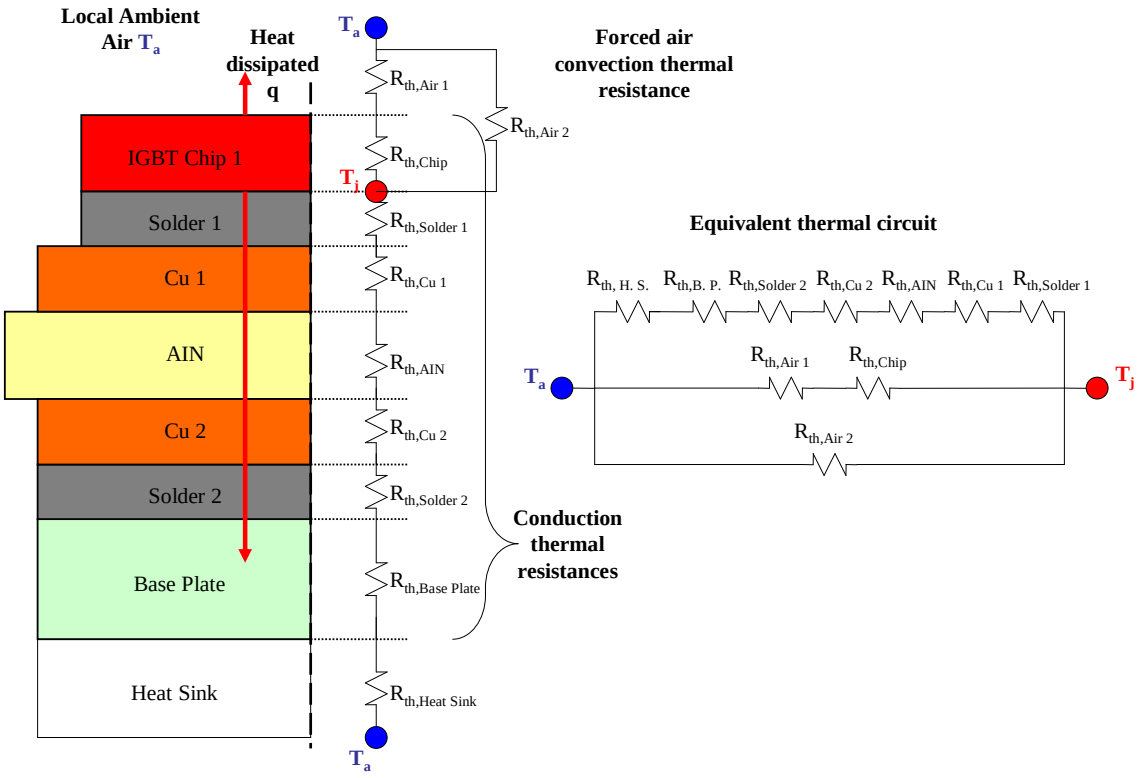

Figure 23: Thermal Resistance Network of Chip Package.

As shown in Figure 22, the thermal circuit consists of parallel sequences of thermal resistances in series. The junction to ambient 1-D heat transfer rate q_{JA} for this package is expressed as:

$$q_{JA} = \frac{T_J - T_A}{R_{JA}} \tag{25}$$

where $T_J - T_A$ is the junction to air temperature difference. The junction to air thermal resistance R_{JA} is the sum of all thermal resistances as follows:

$$R_{JA} = \sum R_{th} = \left(\frac{1}{R_{th,Air1} + R_{th,Chip}} + \frac{1}{R_{th,Air2}} \right)^{-1} \frac{1}{R_{th,HeatSink} + R_{th,BasePlate} + R_{th,Solder2} + R_{th,Cu2} + R_{th,AIN} + R_{th,Cu1} + R_{th,Solder1}} \tag{26}$$

The conduction thermal resistance $R_{th\ layer}$ of through a material layer of chip package is defined as:

$$R_{th,layer} = \frac{t_{layer}}{k_{layer} A_{layer}} \tag{27}$$

where t_{layer} is the thickness of the layer of interest, k_{layer} is the thermal conductivity and A_{layer} is the surface area. The calculated thermal resistances for the various layers of the multi-chip module are listed in Table 8.

Table 8: Conduction Thermal Resistance within IGBT Multi-Chip Module

Layer	Thermal resistance [10^{-3}°K/W]
Solder 1	1.6026
AIN	1.7083
Cu 2	1.0156
Solder 2	0.3125
Silicon	4.0064
Base Plate	0.9921

The thermal resistance $R_{th,conv}$ associated with heat transfer by convection at the surface of the heat spreader may be obtained from Newton's law of cooling:

$$R_{th,conv} = \frac{1}{hA_{layer}} \tag{28}$$

where h is the air convection coefficient, The thermal resistance of the air to the top of the multiple module convection was calculated to be 44.44°C/W. The Cu 1 layer area is much larger than the solder 1 layer area which implies that spreading effects has to be considered. Spreading or constriction resistances exist whenever heat flows from one region of a certain cross-sectional area to another region of a larger cross-sectional area. Such thermal resistance is evaluated using the results obtained by D.P. Kennedy. First, the equivalent radii a and b, for the 2 layers are expressed as:

$$a = \sqrt{\frac{A_{Solder\,1}}{\pi}} = 0.032 \text{ m and } b = \sqrt{\frac{A_{Cu\,1}}{\pi}} = 0.014 \text{ m} \quad (29)$$

The spreading thermal resistance of the Cu 1 layer $R_{Cu\ 1}$ is then evaluated using the following expression:

$$R_{Cu\,1} = \frac{H}{k_{Cu\,1}\pi a} = 1.41 \text{ e}^{-3}\text{°K/W} \quad (30)$$

where the spreading resistance factor, *H*, obtained by the Kennedy curve illustrated by Figure 24, is evaluated to 0.025.

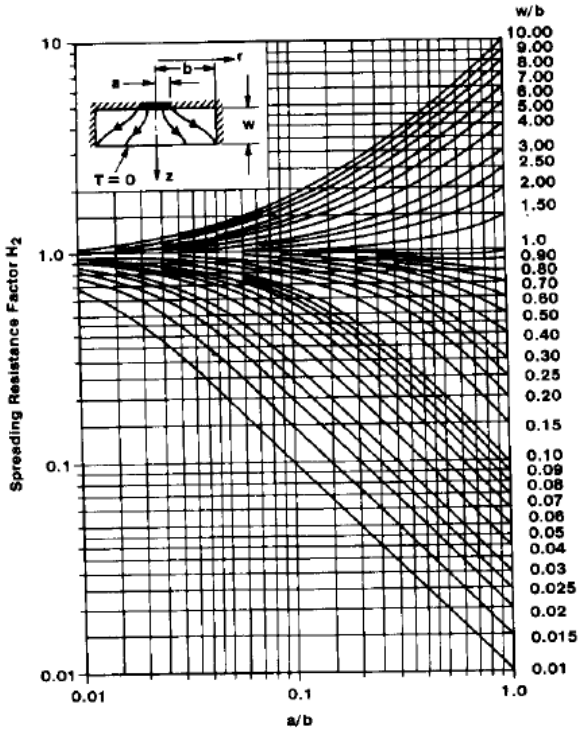

Figure 24: Spreading Resistance Factor *H*

The conduction thermal resistance of the Cu 1 layer without taking into account the heat spreading would have been 2.34 x 10^{-4}°K/W which is 9 times smaller. Assuming a 100W/m^2-°K convection coefficient on the top of the module, a constant base plate temperature and therefore neglecting the heat sink resistance, the total resistance of this multi-chip module using this 1-D thermal resistance network is calculated to be

0.011°C/W using Equation 12. Similar results were obtained by the detailed model. As shown in

Table 10. Despite their inherent mathematical simplicity, 1-D thermal resistance networks are widely used in steady state heat transfer analysis. However, such analysis does not take in account effects of spatially distributed heat sources which may lead to poor accuracy of the junction temperature predictions.

One detailed CFD/HT model consisting of 1,718,187 nodes is created. Then two different compact models with larger grid size and less physical details are also created. Compact model 1 and compact model 2 are composed of 433,199 and 435,741 nodes respectively. The following table illustrates the accuracy of the two compact models compared to the detailed CFD/HT model. To test the accuracy of the developed models and verify that boundary condition independence is achieved the method described by Lasance *et al* [18] is used. Only 10 different sets of various boundary conditions from the 38 proposed in [18] are used. A combination of adiabatic (A), isothermal (T = 300°K) and various convective heat transfer coefficients (h_1 = 10 W/m^2-°K, h_2 = 100 W/m^2-°K, h_3 = 500 W/m^2-°K, h_4 = 1000 W/m^2-°K) are used. The following table lists the boundary conditions used for each case.

Table 9: Boundary Conditions

Case →	1	2	3	4	5	6	7	8	9	10
Top	h_2	h_2	h_2	h_2	h_1	h_1	A	A	A	A
Bottom	T	h_2	h_3	h_4	T	h_3	T	h_3	T	h_3
side	A	A	A	A	A	A	A	A	h_1	h_1

Table 10: Accuracy of Compact Model

	CASE 1 Junction Temperature [°K]					CASE 2 Junction Temperature [°K]				
	Detailed	Compact 1	Error %	Compact 2	Error %	Detailed	Compact 1	Error %	Compact 2	Error %
Base plate	300.00	300.00	0.00	300.00	0.00	654.51	697.89	6.63	682.32	4.25
Diode 1	302.10	302.12	0.01	302.18	0.03	666.34	709.67	6.50	694.19	4.18
Diode 2	302.10	302.11	0.00	302.19	0.03	666.35	709.66	6.50	694.17	4.18
Diode 3	302.10	302.12	0.00	302.18	0.03	666.26	709.61	6.51	694.31	4.21
Diode 4	302.10	302.12	0.00	302.18	0.03	666.27	709.59	6.50	694.28	4.20
IGBT 1	304.47	304.47	0.00	304.60	0.04	671.22	714.43	6.44	699.07	4.15
IGBT 2	304.53	304.54	0.00	304.63	0.03	672.62	716.02	6.45	700.48	4.14
IGBT 3	304.52	304.52	0.00	304.62	0.03	671.09	714.37	6.45	699.33	4.21
	CASE 3 Junction Temperature [°K]					CASE 4 Junction Temperature [°K]				
	Detailed	Compact 1	Error %	Compact 2	Error %	Detailed	Compact 1	Error %	Compact 2	Error %
Base plate	430.72	426.76	-0.92	424.54	-1.44	369.88	368.20	-0.45	367.52	-0.64
Diode 1	443.19	439.21	-0.90	436.82	-1.44	382.04	380.33	-0.45	379.56	-0.65
Diode 2	443.18	439.21	-0.89	436.82	-1.43	382.02	380.34	-0.44	379.57	-0.64
Diode 3	443.17	439.18	-0.90	436.84	-1.43	382.03	380.33	-0.45	379.57	-0.64
Diode 4	443.16	439.19	-0.90	436.84	-1.42	382.02	380.33	-0.44	379.58	-0.64
IGBT 1	447.05	443.16	-0.87	441.03	-1.35	385.79	384.18	-0.42	383.54	-0.58
IGBT 2	449.73	445.76	-0.88	443.22	-1.45	388.53	386.83	-0.44	385.99	-0.65
IGBT 3	447.04	443.14	-0.87	441.12	-1.32	385.81	384.21	-0.41	383.62	-0.57
	CASE 5 Junction Temperature [°K]					CASE 6 Junction Temperature [°K]				
	Detailed	Compact 1	Error %	Compact 2	Error %	Detailed	Compact 1	Error %	Compact 2	Error %
Base plate	300.00	300.00	0.00	300.00	0.00	436.65	446.36	2.23	444.31	1.76
Diode 1	302.10	302.18	-0.03	302.19	0.03	449.31	459.06	2.17	457.01	1.71
Diode 2	302.10	302.18	-0.02	302.19	0.03	449.31	459.05	2.17	457.02	1.72
Diode 3	302.10	302.18	-0.03	302.19	0.03	449.24	459.03	2.18	457.03	1.73
Diode 4	302.10	302.18	-0.02	302.19	0.03	449.25	459.02	2.17	457.03	1.73
IGBT 1	304.48	304.58	-0.03	304.60	0.04	453.09	462.67	2.12	460.94	1.73
IGBT 2	304.54	304.64	-0.03	304.64	0.03	455.87	465.72	2.16	463.50	1.67
IGBT 3	304.52	304.62	-0.03	304.62	0.03	453.00	462.65	2.13	461.03	1.77
	CASE 7 Junction Temperature [°K]					CASE 8 Junction Temperature [°K]				
	Detailed	Compact 1	Error %	Compact 2	Error %	Detailed	Compact 1	Error %	Compact 2	Error %
Base plate	300.00	300.00	0.00	300.00	0.00	439.12	448.86	2.22	447.03	1.80
Diode 1	302.10	302.49	-0.13	302.19	0.03	451.84	459.93	1.79	459.78	1.76
Diode 2	302.10	302.32	-0.07	302.19	0.03	451.83	459.93	1.79	459.78	1.76
Diode 3	302.10	303.92	-0.60	302.19	0.03	451.77	459.96	1.81	459.81	1.78
Diode 4	302.10	304.20	-0.69	302.19	0.03	451.78	459.96	1.81	459.81	1.78
IGBT 1	304.47	304.82	-0.11	304.60	0.04	455.57	463.81	1.81	463.66	1.78
IGBT 2	304.53	304.15	0.13	304.64	0.03	458.41	466.44	1.75	466.29	1.72
IGBT 3	304.52	305.20	-0.22	304.62	0.03	455.49	463.92	1.85	463.77	1.82
	CASE 9 Junction Temperature [°K]					CASE 10 Junction Temperature [°K]				
	Detailed	Compact 1	Error %	Compact 2	Error %	Detailed	Compact 1	Error %	Compact 2	Error %
Base plate	300.00	300.10	-0.03	300.00	0.00	438.61	446.56	1.81	446.36	1.77
Diode 1	302.10	302.29	-0.06	302.19	0.03	451.36	459.36	1.77	459.16	1.73
Diode 2	302.10	302.29	-0.06	302.19	0.03	451.36	459.37	1.77	459.17	1.73
Diode 3	302.10	302.29	-0.06	302.19	0.03	451.30	459.39	1.79	459.19	1.75
Diode 4	302.10	302.29	-0.06	302.19	0.03	451.30	459.40	1.79	459.20	1.75
IGBT 1	304.47	304.70	-0.07	304.60	0.04	455.06	463.14	1.78	462.94	1.73
IGBT 2	304.53	304.74	-0.07	304.64	0.03	457.95	465.93	1.74	465.73	1.70
IGBT 3	304.52	304.72	-0.07	304.62	0.03	454.98	463.26	1.82	463.06	1.78

As shown, the results obtained from the two compact models are extremely closed to those obtained from the detailed CFD/HT model. Under the prescribed conditions, the compact model 2 experiences errors under 5% for the various IGBT and diode chips junction temperatures. As a result the boundary condition independence of the compact model 2 is demonstrated.

Due to relatively smaller dimension scale (~5 μm) and the finer grid compared to the rest of the cabinet, the implementation of the IGBT compact model can not be done directly. The development of CFD/HT models with multiple length scales such as the PCM cabinet is almost impossible using a uniform grid. The resulting model would be too large to be solved by commercially available codes. This implementation is done using a multi grid method described as the two-step "zoom in" multi-scale approach described by Gupta [21] and Nie and Joshi [13] . The zoom-in process involves matching the boundary conditions of the IGBT multi-chip and the top-4-bay CFD/HT models of the PCM cabinets. The cabinet CFD/HT model is used to obtain the boundary conditions of temperature, pressure mass and heat fluxes at the location of the IGBT within the cabinet. The local boundary conditions are extracted and applied to the boundary conditions of the IGBT model. That way, realistic and highly accurate simulations can be easily obtained for the cabinet and the component levels.

3.4 Heat Sink Model

Due to their simplicity, reliability and relative low cost heat sinks are frequently used in power electronics cooling to enhance heat dissipation rate from power sources to the ambient. In order to increase overall system thermal performances and better understand the mechanisms involved in air cooling, heat sinks have received much attention. Flow pressure drop undeniably affects the thermal performance of a heat sink. Predicting the pressure drop across heat sinks is commonly accomplished through the use of theoretical correlation or by experiments. Various theoretical correlations based on

different approaches have been introduced. In the next section, a detailed CFD/HT based heat sink model is developed. The pressure drop results are then compared to theoretical values to validate the model.

The heat sink studied consists of a conventional extrusion heat sink with high fin density used for high power applications. It consists of 14 cm x 10 cm x 1 cm base plate with 46 fins of 3.3 cm high and 0.1 cm thick. The gap between each fin is 0.2 cm. More details about the heat sink specifications and dimensions are given by in the following figure.

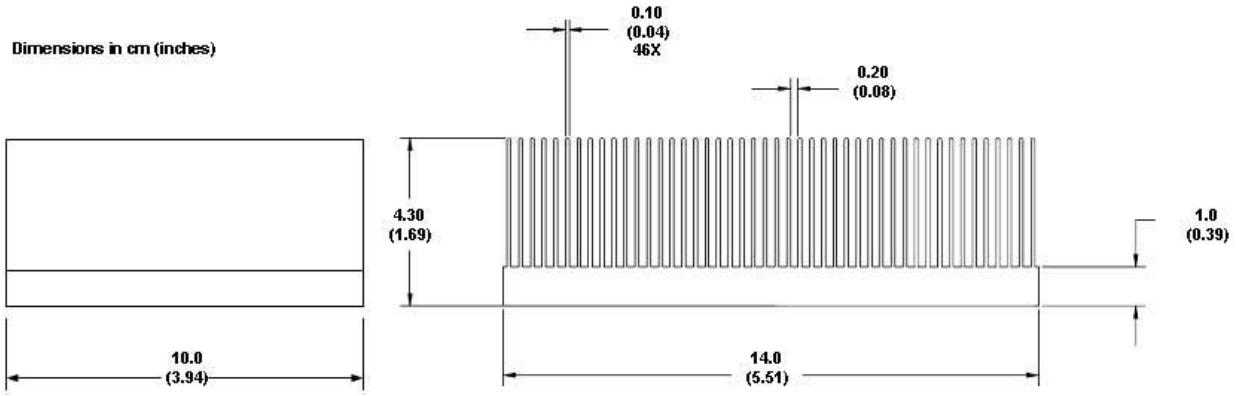

Figure 25: Heat Sink Dimensions

Culham and Muzychka [35] provided the following correlation to calculate air the flow pressure drop through an heat sink:

$$\Delta P = \frac{1}{2}\rho V_{ch}^2 \left[\frac{f_{app} N(2HL + bL)}{HW} + K_c + K_e \right] \tag{31}$$

where the dimension terms H, L and W represent the height, the length and the width of the heat sink respectively and b is the base plate thickness. The hydrodynamic pressure drop is a function of the air density ρ and the channel velocity V_{ch}. The channel velocity is obtained by applying conservation of mass to the flow:

$$\rho_{ap} V_{ap} A_{ap} = \rho_{ch} V_{ch} A_{ch} \tag{32}$$

Assuming that air is incompressible and that flow is equally distributed through the heat exchanger channels, V_{ch} can be defined as:

$$V_{ch} = \frac{V_{ap} A_{ap}}{A_{ch}} = V_{ap} \frac{W H}{N g (H - b)} \tag{33}$$

where N represents the number of fins, g is the width of the gap between two fins, and V_{ap} is the approach velocity of the flow. The hydrodynamic developing flow apparent friction f_{app} is defined as:

$$f_{app} = \frac{1}{\mathrm{Re}_{ch}} \left[\left(\frac{3.44}{\sqrt{x^+}} \right)^2 + \left(f \, \mathrm{Re}_{ch} \right)^2 \right]^{1/2} \tag{34}$$

where the channel Reynolds number Re_{ch} is given by:

$$\mathrm{Re}_{ch} = \frac{V_{ch} D_h}{\upsilon} \tag{35}$$

and the hydrodynamic entrance length x^+ is defined as:

$$x^+ = \frac{L}{D_h \, \mathrm{Re}_{ch}} \tag{36}$$

The fully developed laminar flow friction factor f can be obtained from the following:

$$f \, \mathrm{Re}_{ch} = 24 - 32.53\beta + 46.72\beta^2 - 40.83\beta^3 + 22.96\beta^4 - 6.09\beta^5 \tag{37}$$

where,

$$\beta = \frac{b}{H} \tag{38}$$

Pressure drops caused by abrupt flow area expansion and contraction at the inlet and exit of the heat sink are captured respectively by the expansion loss coefficient K_e given by:

$$K_e = \left(1-\alpha^2\right)^2 \tag{39}$$

and the contraction loss coefficient K_c defined as:

$$K_c = 0.42\left(1-\alpha^2\right) \tag{40}$$

where

$$\alpha = 1-\frac{N}{W} \tag{41}$$

An extremely fine mesh was necessary to characterize this heat sink. With a gap between the fins of 2 mm wide, a mesh size of 0.25 mm was used to accurately predict the flow and heat transfer within those channels. The total number of nodes of the heat sink model is evaluated to 4,236,874. To define the pressure drop as accurately as possible, the heat sink model is mounted in a rectangular duct with dimensions of 14 cm wide x 4.3 cm tall x 30 cm long.

In order to validate the heat sink model, pressure drop values obtained from the numerical CFD/HT model at the inlet and the outlet of the duct are compared to theoretical values calculated using Equation 11. Figure 26 gives a comparison of those results. As shown, the pressure drop results obtained from the CFD/HT model are particularly close (within 12 %) to the theoretical values.

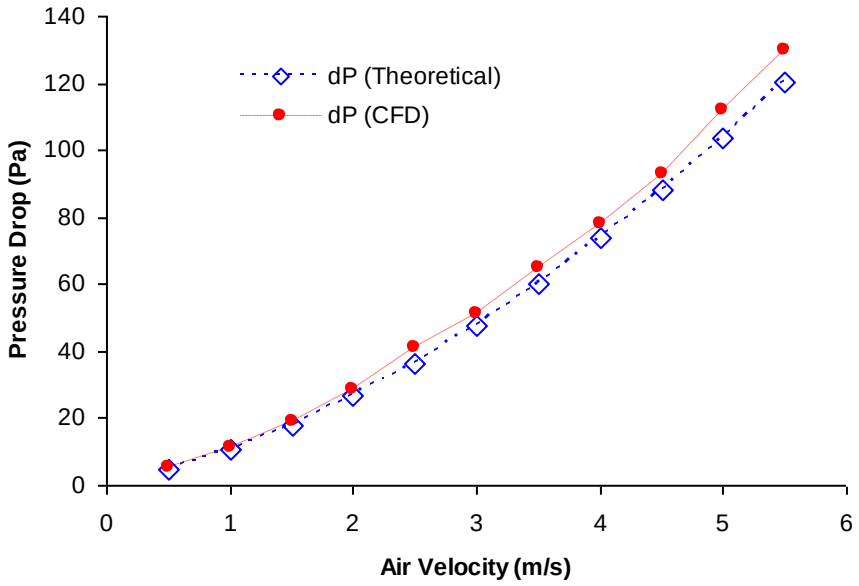

Figure 26: Pressure Drop across Heat Sink

CHAPTER 4

MODELING RESULTS

The following section describes the system-level simulation results obtain. Bulk flow properties such as the temperature, pressure, or volumetric at the inlet and outlet of each bay were computed using the area weighted average of the quantity over all the grid cell facets involved in the cross-section of interest. The boundaries the top-4-bays and the bottom bay models as well as the inlet and outlet locations for the bays are shown in the following figure.

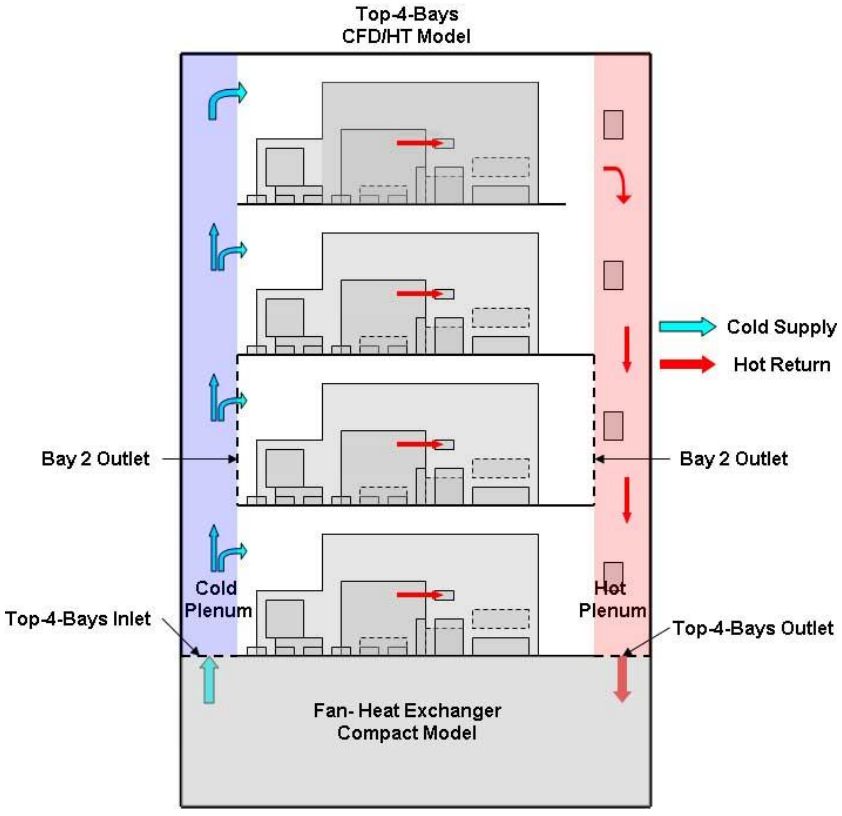

Figure 27: Cabinet Modeling

4.1 PCM-1 Models Results

In order to determine the cabinet operating point of the entire system, the pressure change across the top 4 bays and the heat exchanger models have to match. From Figure 28, it can be seen that as the air flow rate increases, the pressure change across the heat exchanger and the plenum increases while the return fan pressure head decreases. As a result, the net pressure change decreases across the bottom bay from 308.6 Pa at 0.19 m^3/s (400 CFM) to -907.1 Pa at 0.94 m^3/s (2000 CFM).

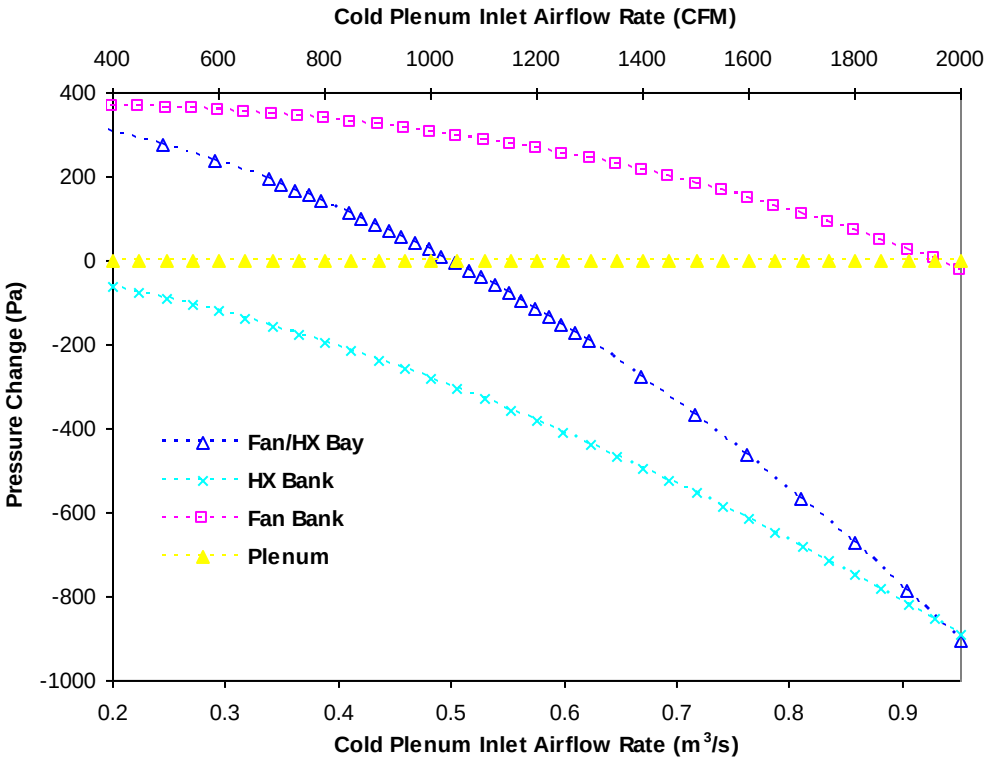

Figure 28: Bottom Bay Pressure Change

The results obtained from the top-4-bay CFD/HT simulations predict an overall flow pressure drop across the four SSCM modules as the inlet air flow rate increases. Pressure changes obtained independently from the top-4-bay CFD/HT model and the

bottom bay heat exchanger model are illustrated in Figure 29. The graph shows the decreasing pressure change across the bottom heat exchanger bay and the increasing pressure drop across the top four bays for a range of air flow rates.

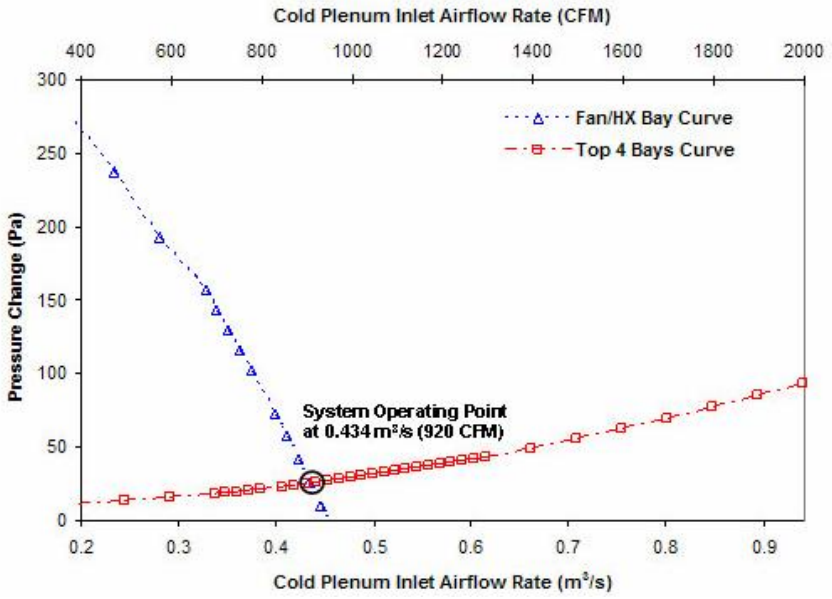

Figure 29: PCM-1 cabinet pressure characteristics

The operating point of the PCM-1 cabinet is determined by the intersection of the two model characteristic curves. The operating point is estimated to be at air flow rate of 0.434 m^3/s (920 CFM), corresponding to a pressure change across the two models of 26 Pa.

Air flow temperatures at the inlet and outlet grilles separating the bottom bay from the top four bays are first evaluated by the bottom bay model and used as the boundary conditions for the CFD/HT model. The following figure shows the inlet air temperature predicted by the bottom-bay model. As shown, the inlet temperature range from 47.5°C to 49.2°C on the air flow rate range observed.

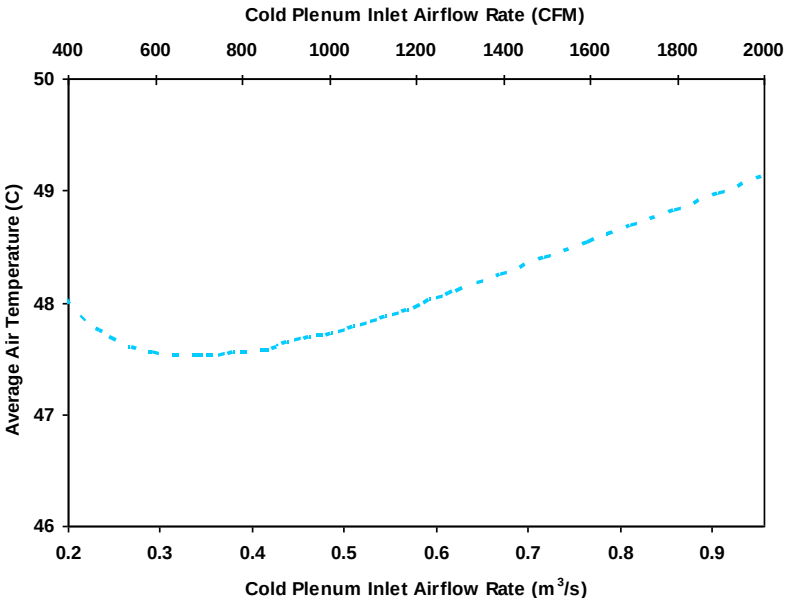

Figure 30: Inlet Air Flow Temperature Predicted by Bottom Bay HX Model

The CFD/HT results for the air flow temperature rise between the inlet and the outlet of the top four bays are shown in Figure 31. As illustrated, the air temperature rise decreases as the cold plenum inlet air flow rate increases. At operating point, the temperature rise of the airflow through the four SSCM modules is evaluated to 11 °C.

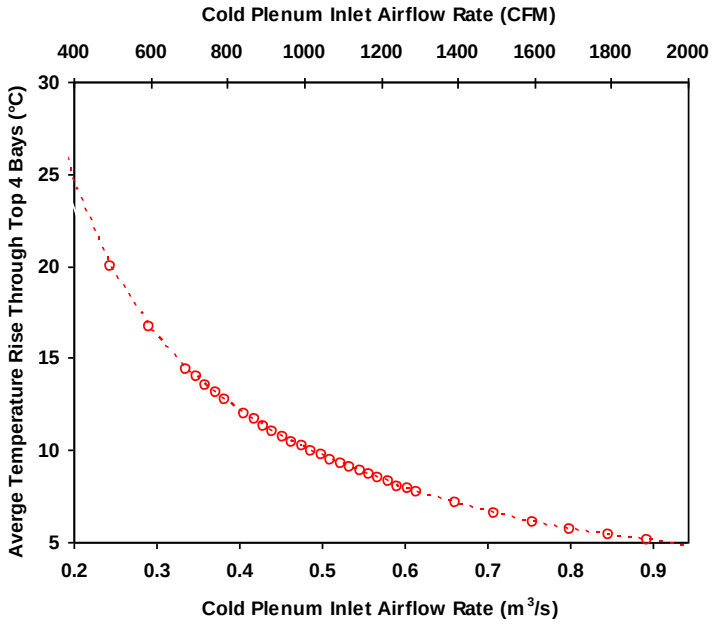

Figure 31: Average Air Flow Temperature Rise through the Top 4 Bays of the PCM-1 Cabinet

Figure 32 gives a comparison of the average air temperature rise through each SSCM module as the cold plenum inlet airflow rate increases. Larges discrepancies appear between the air temperature behaviors through the various bays.

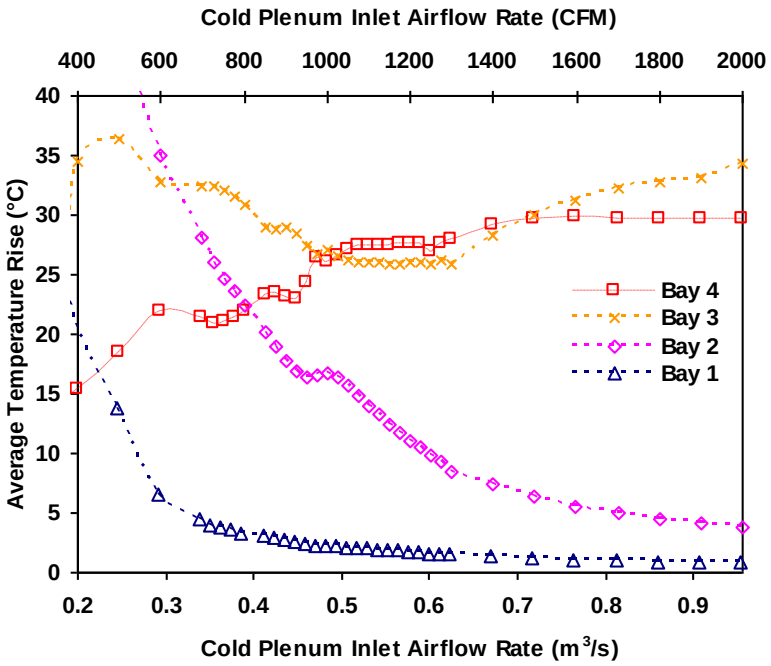

Figure 32: Average Air Flow Temperature Rise through the PCM-1 Cabinet

Bay 1 experiences the lowest temperature rise on the observed air flow rate range. The air temperature rise reduces as the inlet air flow rate increases in a similar way in Bay 1 and Bay 2. However, the air temperature rise characteristics of the upper Bay 3 and Bay 4 are completely different. While Bay 1 experiences a low temperature rises of 2.5°C, Bay 2, Bay 3 and Bay 4 experience a temperature rise of 16°C ,28°C and 23°C respectively. These values for the various SSCM air temperature rises increase for larger air flow rates since the bay temperature rise increases through Bay 3 and Bay 4 as the air flow rate increases.

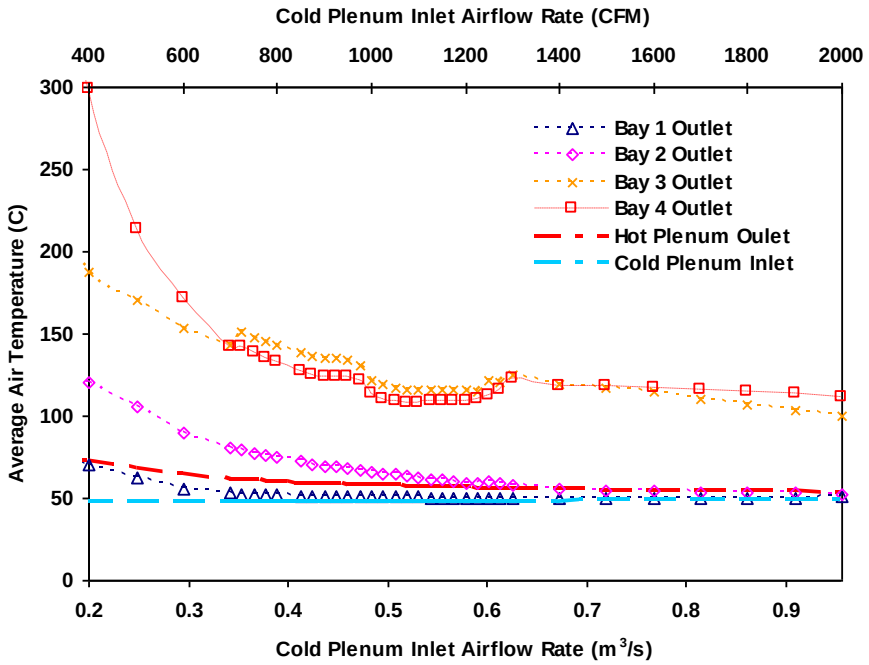

Figure 33: Air temperature at the PCM-1 cabinet bay outlets

The average temperatures at the outlets of the various SSCMs reveal another anomaly in the flow behavior within the cabinet. As illustrated in Figure 33, Bay 3 and Bay 4 temperatures in the hot plenum are much larger than for Bay 1 and Bay 2. While outlet temperature differences between Bay 1 and Bay 2 vanishes as the inlet flow rate increases and their values approach the hot plenum temperature, Bay 3 and Bay 4 outlet temperatures remain 50°C higher.

Despite the fact that the disparity between Bay 1 and Bay 2 temperature diminishes at large air flow rate, the air flow temperature discrepancies revealed by Figure 32 and Figure 33 suggest that either a lack of fluid motion or a region of re-circulating flow is experienced in Bays 2, 3 and 4. Therefore, a closer look at the air flow distribution is needed. Figure 34 and Figure 35 compare the flow rate at the inlet and outlet of each bay of the PCM-1 cabinet. Here again, major discrepancies appear between the various bays. As illustrated, the flow is unevenly distributed through the four bays of the PCM-1 cabinet.

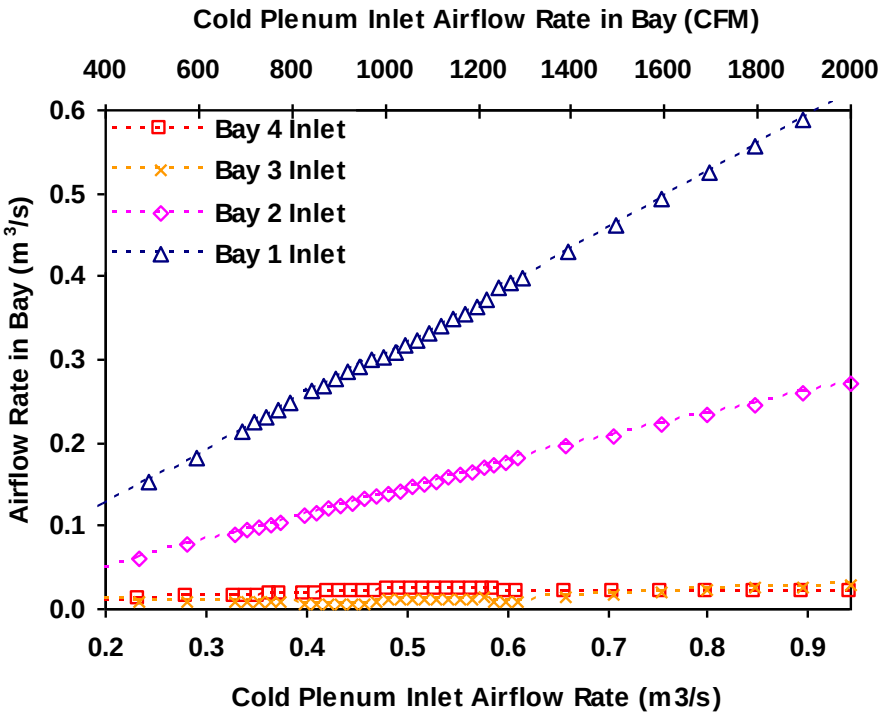

Figure 34: Airflow Rate through SSCM Inlets

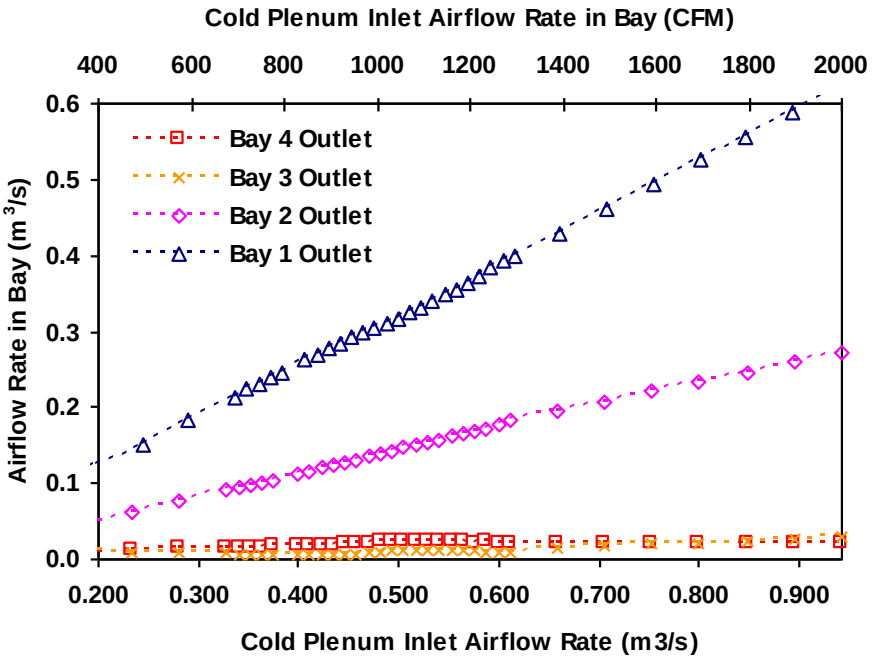

Figure 35: Airflow Rate through SSCM Outlets

It can be seen that Bay 1, which is the closest to the cold plenum inlet, experiences a significantly higher air flow rate. At the operating point, for a cold plenum

inlet flow rate of 0.434 m^3/s (920 CFM), the flow though Bay 1 is 0.349 m^3/s while Bay 2, 3 and 4 experience a flow rate of 0.152 m^3/s, 0.008 m^3/s and 0.023 m^3/s respectively . In other words, the air flow rate within Bay 1 is about twice as high as the combined airflow through all other bays, and more than 90 % of the cold plenum inlet flow rate goes exclusively through Bay 1 and Bay 2. As the total air flow rate increases, the trend continues with most of the cold air being directed exclusively to Bay 1 and Bay 2. A lack of flow motion is clearly observed in the 2 upper bays resulting in the higher temperatures observed previously for Bay 3 and Bay 4.

Figure 36 shows the flow field at the operating point within the upper four bays of PCM-1 Cabinet. Cross-sections of the flow in the four SSCMs at x = 0.1, 0.3 and 0.5 m are illustrated.

Figure 36 confirms the results presented previously, the flow velocity at various cross sections, represented by the blue arrows, appears to be larger in Bay 1 than in the other three upper bays.

Furthermore, the red arrows reveal the presence of regions experiencing flow re-circulation. Re-circulation is observed principally in the regions that experience low flow rates. This local reversed flow, coupled with a lack flow motion, results in air high temperature and consequently high component temperatures.

Figure 36: Flow Field within PCM-1 Cabinet at Various Cross Sections

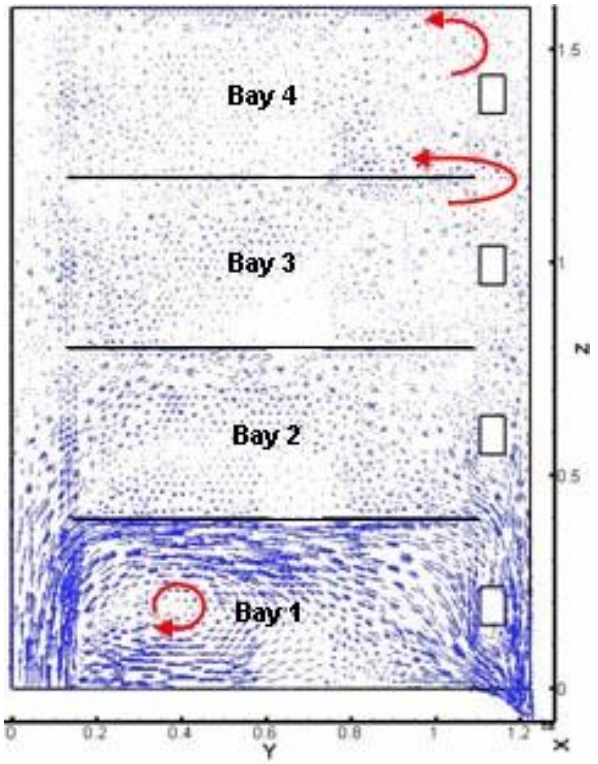

(a) x = 0.1 m

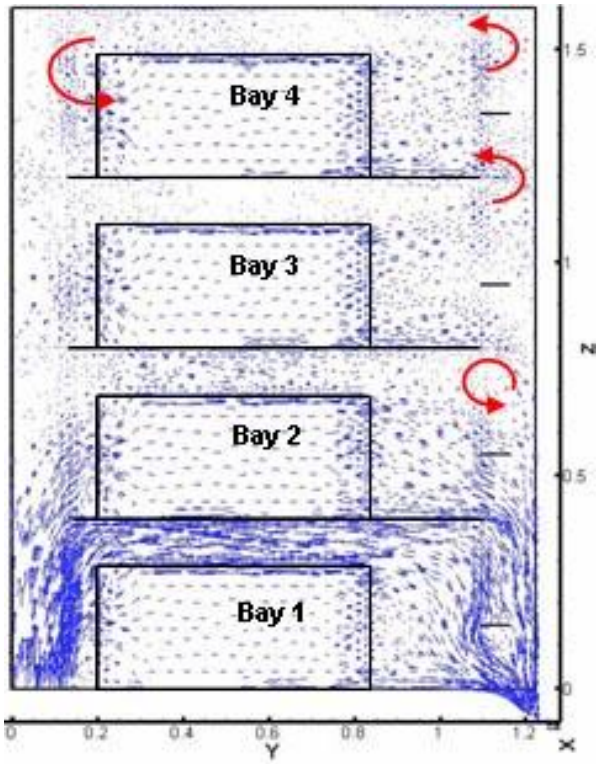

(b) x = 0.3 m

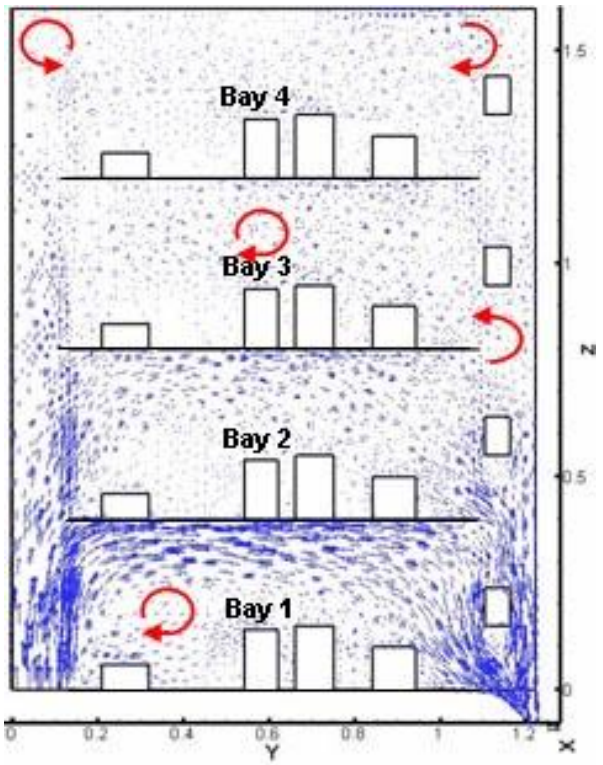

(c) x = 0.5 m

Figure 37 (continued): Flow Field within PCM-1 Cabinet at Various Cross Sections

4.2 PCM-2 Models Results

As illustrated in Figure 37, as the air flow rate increases, the pressure across the heat exchanger and the plenum increases while the return fan pressure head decreases. As a result, the net pressure change decreases across the bottom bay from 271 Pa at 0.19 m^3/s (400 CFM) to -1180 Pa at 0.94 m^3/s (2000 CFM). The difference with the pressure change values obtained for PCM-1 bottom bay cabinet can be explained from the presence of 5 heat exchangers and 2 fans in the bottom bay of the PCM-2 cabinet.

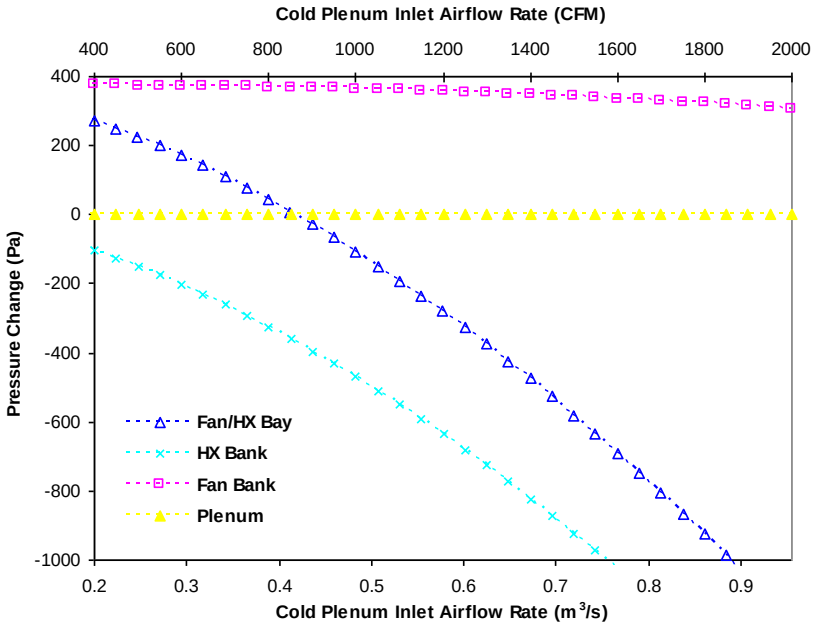

Figure 37: Bottom Bay Pressure Change

As stated previously, the pressure change across the top 4 bays and the heat exchanger models have to match in order to determine the cabinet operating point of the entire system. Figure 38 illustrates pressure changes obtained separately from the PCM-2 top-4-bay CFD/HT model and the bottom bay heat exchanger model. The graph shows the decreasing pressure change across the bottom heat exchanger bay and the increasing pressure drop across the top four bays as the cold plenum air flow rate increases.

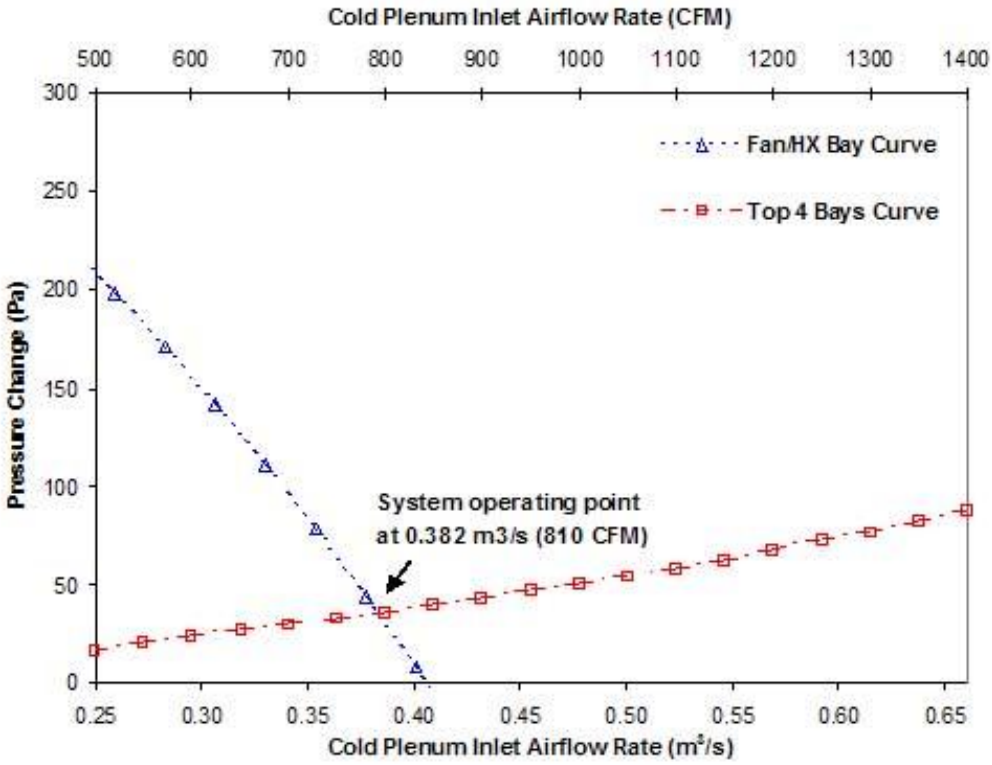

Figure 38: PCM-2 Cabinet Pressure Characteristics

The operating point of the PCM-2 cabinet, represented by the intersection of the two model characteristic curves, is estimated to be at air flow rate of 0.382 m^3/s (810 CFM) corresponding to a pressure change across the two models of 38 Pa. The PCM-2 system operating point is at a lower flow rate than the PCM-1 cabinet. The Fan/HX pressure curve is shifted on the left due to larger number of heat exchangers and fans.

Figure 39 shows the inlet air temperature predicted by the bottom-bay model. As shown, the inlet temperature ranges from 46.5°C to 48.5°C on the air flow rate range observed.

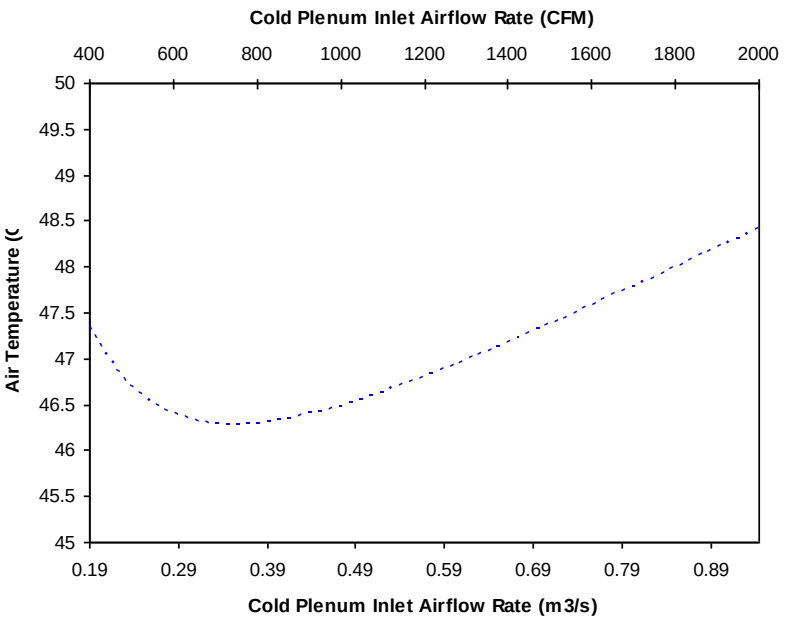

Figure 39: Inlet Air Flow Temperature Predicted by Bottom Bay HX Model

Figure 40 shows the CFD/HT results for the air flow temperature rise in the top four bays. As illustrated, the airflow temperature decreases as the cold plenum inlet air flow rate increases. A temperature rise between the inlet and the outlet of the 4 upper bays of 24°C is simulated at operating point.

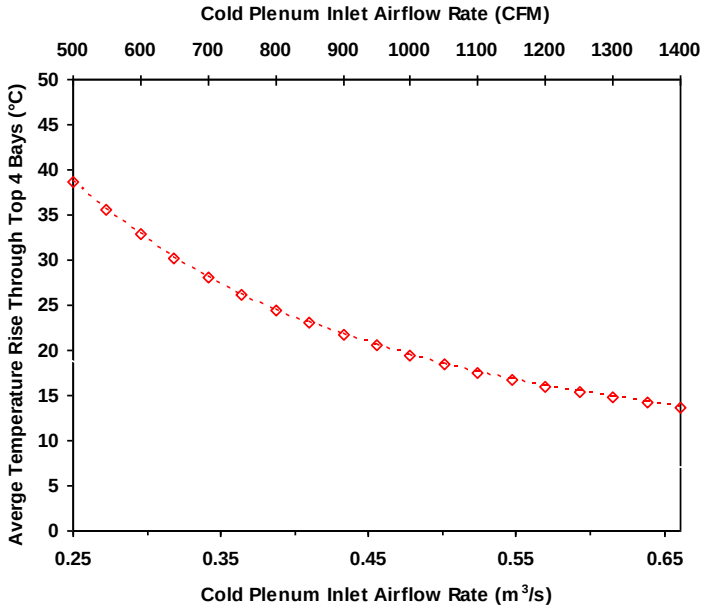

Figure 40: Average Air Flow Temperature Rise through the Top 4 Bays of the PCM-2 Cabinet

Figure 41 gives a comparison of the average air temperature rise through each SSIM module as the cold plenum inlet airflow rate increases. As illustrated, differences appear once again in the air temperature between the various bays.

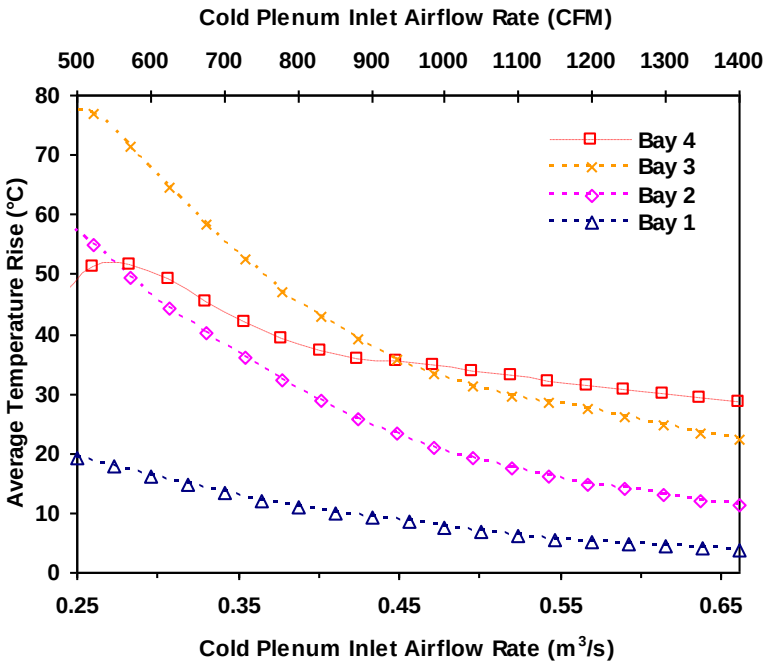

Figure 41: Average Air Flow Temperature Rise through the PCM-2 Cabinet

As illustrated in Figure 41, Bay 1 experiences the lowest temperature rise on the investigated airflow rate range. While Bay 1 experiences a low temperature rises of 10.5°C at the operating point, Bay 2, Bay 3 and Bay 4 experience a temperature rise of 32°C, 39°C and 47°C, respectively.

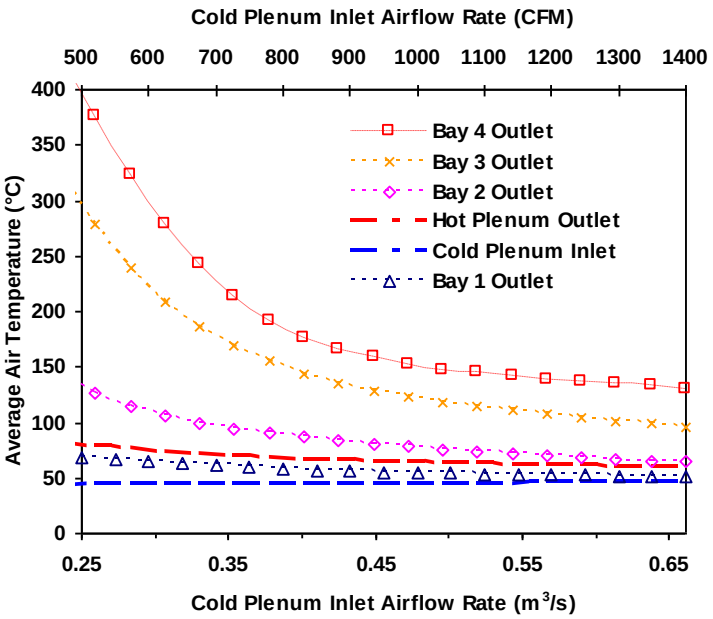

Figure 42: Air temperature at the PCM-2 Cabinet Bay Outlets

The average temperatures at the outlets of the various SSIMs show the same behavior as observed for the PCM-1 cabinet. As illustrated in Figure 42, Bay 3 and Bay 4 temperatures in the hot plenum are much larger than for Bay 1 and Bay 2. Bay 3 and Bay 4 outlet temperatures remain larger than 100°C, while outlet temperature differences between Bay 1 and Bay 2 decrease as the inlet flow rate increases.

The high air flow temperatures and discrepancies revealed by Figure 41 and Figure 42 suggest that here also a lack of fluid motion is experience in the upper bays of the PCM-2 cabinet. Figure 43 and Figure 44 illustrate the air flow rate respectively at the inlet and outlet of each bay of the PCM-2 cabinet.

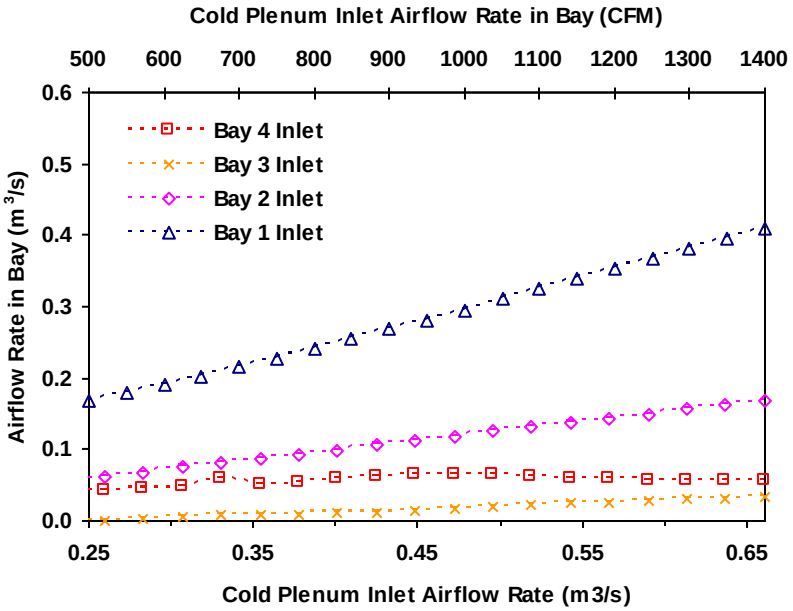

Figure 43: Airflow Rate through SSIM Inlets

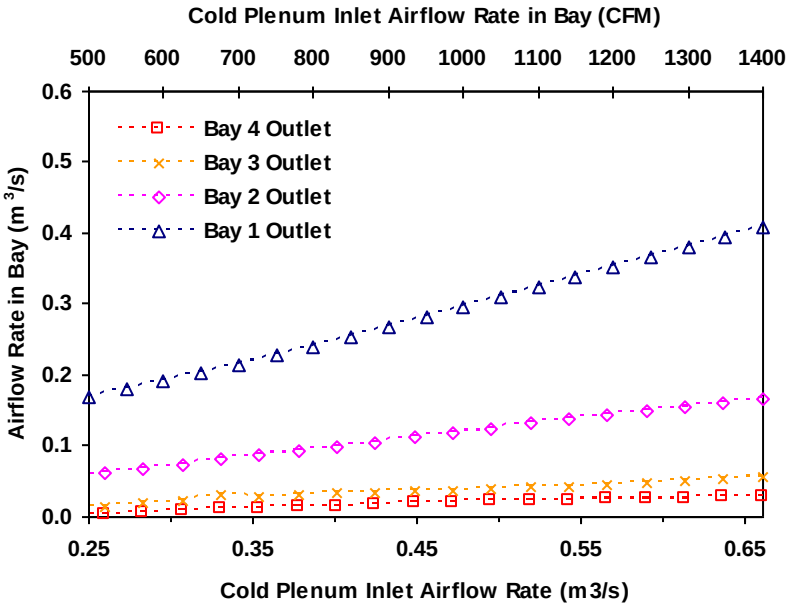

Figure 44: Airflow Rate through SSIM Outlets

It appears that the flow in not uniformly distributed in the four SSIMs. As expected, Bay 1 experiences a higher air flow rate than the others. At the operating point, for a cold plenum inlet flow rate of 0.382 m^3/s (810 CFM), the flow though Bay 1 is 0.242 m^3/s, while Bay 2, 3 and 4 experience a flow rate of 0.095 m^3/s, 0.031 m^3/s and 0.013 m^3/s respectively. 40 % of the cold plenum inlet flow goes exclusively through Bay

1. As the overall system air flow rate increases, the trend continues with most of the cold air being directed exclusively to Bay 1 and here also, a lack of flow motion is clearly observed in the 3 upper bays. This again results in the higher temperatures revealed in Figure 41 and Figure 42.

4.3 IGBT Multi- Chip Power Module and Heat Sink models

In order to demonstrate the transient capacity of the CFD/HT model, simulations are run for realistic high power cycles of the IGBT multi-chip module mounted on the heat sink device, which is designed for high power applications experiencing a forced convection air flow at 2 m/s. The assembly is tested for a set of three different power cycles ranging from 264 W to 1056. The heat loss densities are listed in Table 11.

Table 11: IGBT Multi-Chip Module Heat Losses

	Case 1 Heat Losses			Case 2 Heat Losses			Case 3 Heat Losses		
	W/cm^2	W	W/m^3	W/cm^2	W	W/m^3	W/cm^2	W	W/m^3
IGBT (3)	50	72	1.333e+09	100	144	2.667e+09	200	288	5.333e+09
Diode (4)	25	12	6.667e+09	50	24	1.333e+09	100	48	2.667e+09
Total		264			528			1056	

Figure 45 shows the heating curves for the various investigated cases. A 1 sec power cycle is simulated for each of the 3 cases.

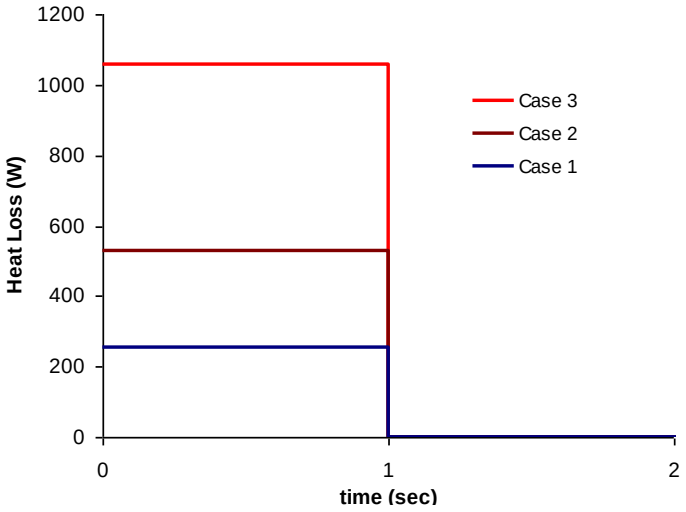

Figure 45: IGBT Multi-Chip Power Cycles

The following figures illustrate the transient results obtained by the compact model of the IGBT multi-chip power module. The average junction temperature of each chip within the module is plotted over time.

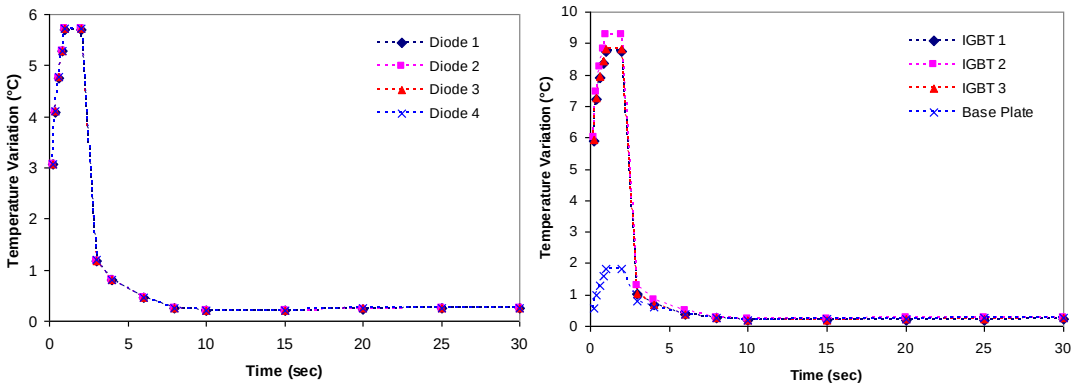

(a) 254 W Heat Losses

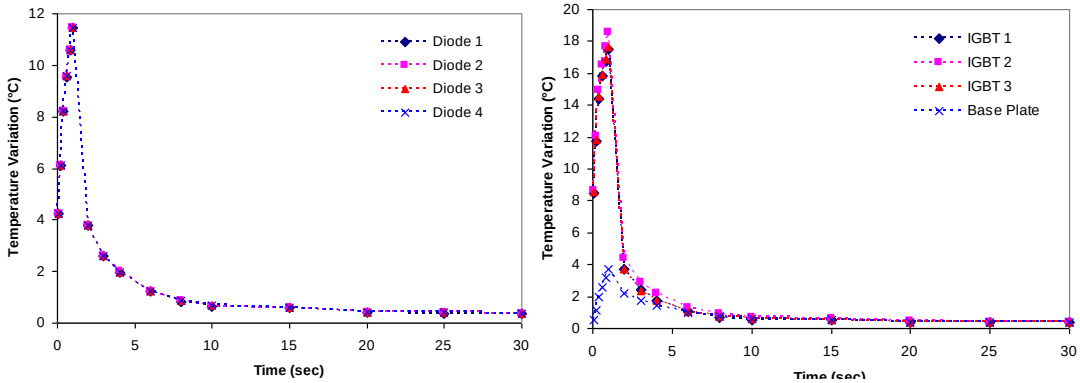

(b) 528 W Heat Losses

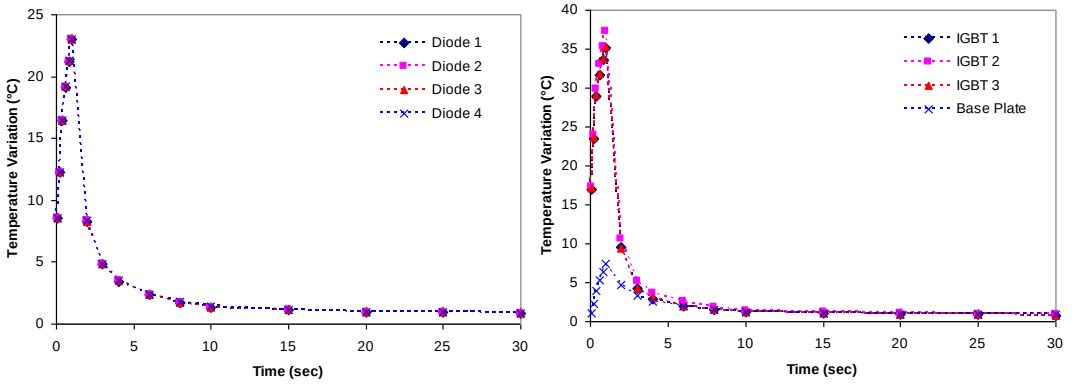

(c) 1056 W Heat Losses

Figure 46: Transient Temperature Curves of Multi-Chip Power Module

As expected, the multi-chip power module experiences the largest temperature rises when 1056 W of heat is dissipated. The average junction temperature of the central

chip, IGBT 2, experiences the highest temperature increase with 37.3°C. The other two IGBT chips experience similar temperature rises, reaching 35.3°C at the end of the heating cycle. Figure 46 also demonstrates the fact that it takes longer for the IGBT to recover from larger power pulse.

Figure 47 illustrates the temperature distribution on the Cu 1 layer of the multi-chip module over time for an ambient temperature of 300°K and a local flow velocity 2 m/s. Hot spots corresponding to the chip junctions clearly appear. It can be seen also that the highest temperatures occur along the center line while the edges remain cooler. The local highest temperature observed is around 343°K at the middle IGBT chip.

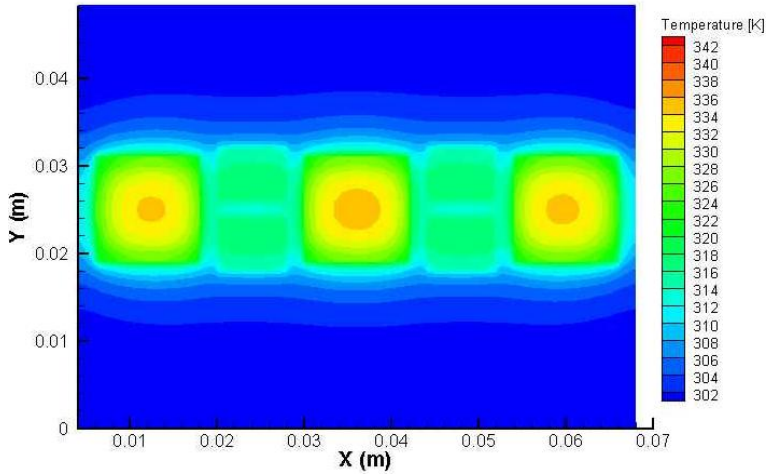

(a) t = 0.4 s

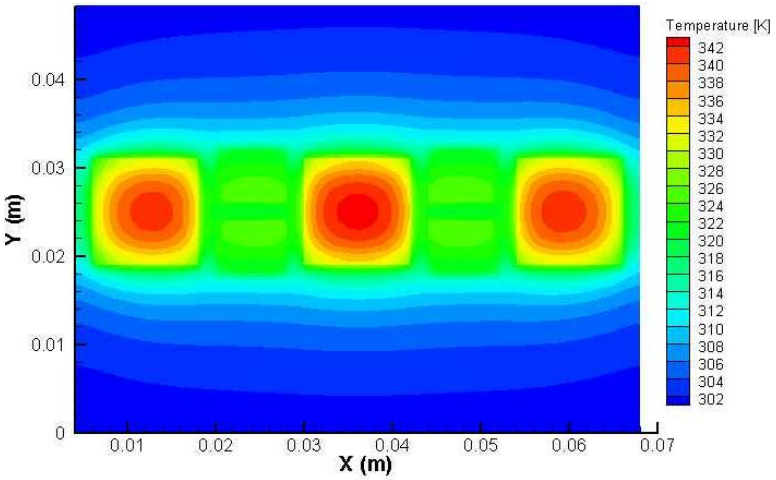

(b) t = 1 s

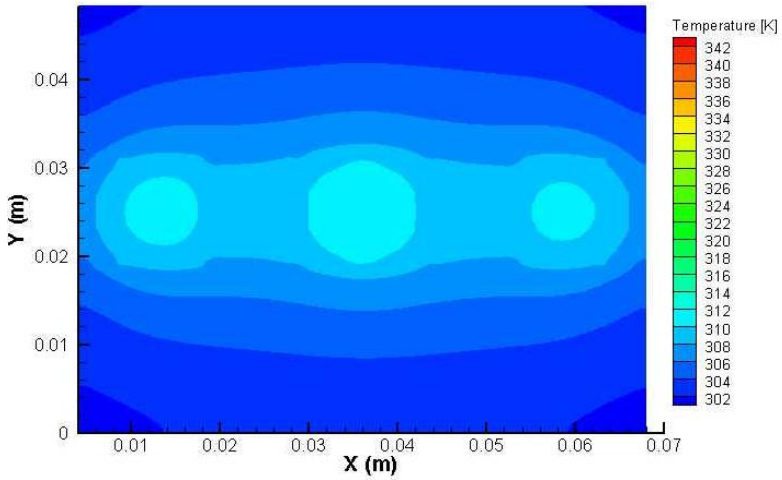

(c) t = 2 s

Figure 47: Temperature Distribution within IGBT Multi-Chip Module

CHAPTER 5

THE PROPER ORTHOGONAL DECOMPOSITION FOR REDUCED ORDER MODELING

In the following section, a description of the proper orthogonal decomposition technique is given, followed by the development of a power cabinet reduced order model along with its application with a single parameter POD technique.

5.1 Proper Orthogonal Decomposition: Literature Review

Proper Orthogonal Decomposition (POD) is an emerging reduced order model development approach for turbulent flows. This technique is used to assemble the model-specific optimal linear subspace from a group of system observations. The POD has been applied to a broad range of disciplines such as image processing and pattern recognition [36], weather prediction [37], mechanical vibrations [38]. POD has been also successfully applied to develop reduced order models in turbulent flows (Cizmas [39]; Lumley [40]; Holmes [41]; Arndt *et al*. [42]), and to design simplified flow control mechanisms (Efe and Ozbay [43]; Ly and Tran [44]; Podvin and Lumley [45]). As noted by Smith *et al*. [46], the POD goes by several different names in other disciplines, including Karhunen-Loeve decomposition, principal components analysis, singular systems analysis, and singular value decomposition.

POD can be found back in independent investigations by Kosambi [47] in 1943, Loéve [48] in 1945, Karhunen [49] in 1946, Pougachev [50] in 1953 and Obukhov [51] in 1954. But it wasn't until the 1960's that this technique was applied in the field of turbulence by Theodorsen [52] and Townsend [53], and with some developments by

Lumley [40]. Holmes *et al.* [41] provides an extensive amount of background information concerning the foundations of proper orthogonal decomposition, its optimality, uses, and properties. Chatterjee [54] describes an overview of POD and a few simple numeric examples of its applications performed using MATLAB. Cizmas *et al.* [39] researched and investigated the use of POD in the numerical simulation of a rotor-stator interaction in a one-stage turbine. The snapshots method was used to develop the basis functions. These functions were used as a reduce order model via Galerkin's projections.

Sirisup and Karniadakis [55] have made developments in low-dimensional flow modeling and proposed to use a penalty function Galerkin method to treat time varying boundary conditions. Taylor and Glauser [56] investigated geometrical scaling and created a low-dimensional model of a variable angle diffuser at the expense of 30,720 observations. POD for reduced turbulent simulations of flows with moving limits was studied by Uttakar *et al.* and the accuracy as well as the data compression associated with POD representation of the observations was also investigated [57]. Galetti *et al.* [58] developed POD-based models of flows over a large range of Reynolds and Rayleigh numbers. The inhomogeneous boundary conditions are either treated through expensive homogenization procedures or through extensive and unreasonable number of 160 system observations.

Rambo [59] provides in his doctoral work the two major deficiencies with the standard POD procedure. First, the Galerkin projection has been demonstrated to produce false limit cycles [60] and deemphasize important modal contributions under varying boundary conditions. Second deficiency is that in previous reduced-order flow modeling studies, homogeneous boundary conditions in the form of either closed [61, 62] or periodic domains [63, 64] are employed. Inhomogeneous boundary conditions have also been treated by subtracting reference velocity fields; these reference fields must

satisfy the governing equations. Therefore, in order to modify the boundary conditions, a new reference field for each set of conditions must be obtained.

5.2 Single Parameter POD with Method of Snapshots

In principle, the idea is to start from an ensemble of data called observations or snapshots of the studied system collected through physical experiments or numerical simulations such as CFD/HT solutions. Enough observations have to be made to cover the simulation range of interest for the compact model. The POD technique uses the ensemble of observation data to produce a set of basis functions that allow physics-based interpolation between the snapshots.

This section presents the application of a single parameter POD technique to develop a reduced-order model of the power cabinets. The model is needed to drastically reduce the optimization efforts by simulating the effect of the inlet airflow rate on the electronics cooling. In the first step, CFD/HT solutions of the power cabinets are obtained for several airflow rates. Then, "empirical" eigenmodes are computed from these observation data that can be used to accurately predict the system characteristics at the desired air flow rate within the observation range. Figure 48 summarizes the model reduction process.

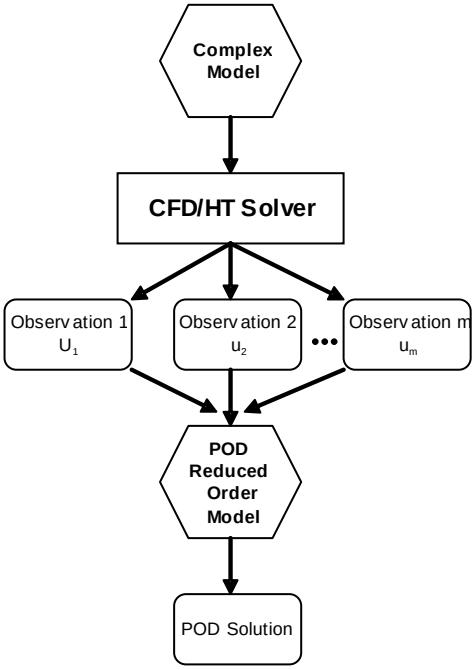

Figure 48: Model reduction process

To construct the POD modes of the velocity field, an ensemble of flow field observations $\vec{U}(\vec{x})$ is obtained by combining the independent observations of the system in an n×m matrix, where n is the number of DOF and m is the number of observations. Therefore, the velocity field data ensemble is defined as:

$$\vec{U} = \left\{ \vec{u}_1, \vec{u}_2, ..., \vec{u}_m \right\} \text{ or}$$

$$\vec{U} = \begin{pmatrix} u_{1,1}(\dot{v}_{a_1}) & u_{1,2}(\dot{v}_{a2}) & \cdots & u_{1,m}(\dot{v}_{am}) \\ \vdots & \vdots & & \vdots \\ u_{n,1}(\dot{v}_{a1}) & u_{n,2}(\dot{v}_{a2}) & \cdots & u_{n,m}(\dot{v}_{am}) \end{pmatrix} \quad (42)$$

where each column vector $u_{:,j} \in Rn$ for j = 1, 2, …, m represents a single snapshot that describes the three components of the velocity vector $\vec{u}_i = \{u, v, w\}$ for i = 1, 2, …, n at nodal position $\vec{x} = (x, y, z)$. It is important to state that the data ensemble can similarly describe any characteristic of the studied domain such as temperature or pressure field.

It is explained by Rambo [52] that the empirical basis functions of the system also called the POD modes are in fact the eigenvectors of the covariance matrix $\vec{C}$ defined as

$$\vec{C} = \frac{1}{m}\vec{U}\vec{U}^T \in \mathrm{R}^{\mathrm{n\ x\ n}} \tag{43}$$

Before proceeding to the solution, it is important to state that mean centering is usually performed in turbulent POD studies and the modes are defined as a deviation from the observation mean $\overline{\vec{U}}$. Therefore, the mean of the ensemble of snapshots is introduced and defined as:

$$\overline{\vec{U}} = \frac{1}{m}\sum_{i=1}^{m}\vec{u}_i \tag{44}$$

The deviation from the ensemble average $\vec{V}_i$ is given by:

$$\vec{V}_i = \vec{u}_i - \overline{\vec{U}} \tag{45}$$

For 3-D CFD/HT systems, the total number of DOF, n, for each observation is much larger than the total number of observations, m. Large DOF problems are computationally unsolvable, as most algorithms are capable of solving problems with matrix sizes in the order of 10^5. Therefore, a modified covariance matrix based on the deviation from the ensemble average is introduced such that the number of observations, m, dictates the size of the basis function computation, as follows.

$$\vec{\mathrm{C}}' = \frac{1}{m}\vec{V}^T\vec{V} \in \mathrm{R}^{\mathrm{m\ x\ m}} \tag{46}$$

The computation of the POD modes is reformulated as an $m \times m$ eigenvalue problem. $\vec{\varphi}$ and λ are respectively defined as the eigenmodes and eigenvalues of the following eigenvalue problem.

$$\vec{C}'b = \lambda b \tag{47}$$

The POD based interpolation requires using the eigenmodes as the base modes, and b_i, the relative weight of each mode. The weight coefficients are also eigenvectors of the solution to Equation 25. The eigenmodes are defined as

$$\vec{\varphi} = \sum_{i=1}^{m} b_i \vec{u}_i \tag{48}$$

A Matlab algorithm is used to solve the eigenvalue problem introduced by Equation 25 and to compute the weight coefficients b_i. The observation data are collected, and the observation matrix is decomposed using the singular value decomposition (SVD). The singular value decomposition takes an n x m rectangular matrix A, and produces the following decomposition:

$$A = L\Sigma R^T \tag{49}$$

where L is an n x n matrix whose columns are the left singular vectors; $\sum$ is a singular value matrix with the same dimensions as A and its diagonal form the mode amplitudes; and R is an m x m matrix whose columns form the right singular vectors. Positive semi-definite matrix can be obtained as the product of matrix A by its transpose A^T. $A^T A$ is therefore square and symmetric. Its eigenvalues are all positive or zero, and the eigenvectors corresponding to different eigenvalues are pairwise orthogonal. SVD consists of finding the eigenvalues and eigenvectors of $A^T A$, as shown below:

$$A^T A = R\Sigma L^T \; L\Sigma R^T = R\Sigma^2 R^T \tag{50}$$

The columns of R are the right singular vectors of $A^T A$. The eigenvalues of $A^T A$ are simply the square roots of the diagonal of the singular values matrix $\sum$:

$$\lambda_i = \sqrt{\Sigma_{ii}} \tag{51}$$

where $i = 1,2 \ldots p$; p is the number of POD modes.

The weight coefficients b_i are obtained in a similar way from the normalized right singular vector of the modified covariance matrix C' using SVD. Equation 26 can be used to calculate the eigenmodes $\vec{\varphi}_i$ of the original problem from the weight coefficient b_i. The governing equation is projected onto the set of eigenmodes to obtain appropriate

amplitude mode coefficients a_i, sufficient to optimally reconstruct the solution. The amplitude coefficients are obtained by applying the inner product of the deviation from the ensemble average $\vec{V}_i$. The system flow velocity field $\vec{u}*$ at a specified parameter value $\dot{v}_a*$ can then be estimated by:

$$\vec{u}* = \overrightarrow{\overline{U}} + \sum_{i=1}^{p} a_i \vec{\varphi}_i \qquad (52)$$

The mean centering is motivated by the Galerkin methods, where the mean satisfies the non-homogeneous boundary conditions. The weight coefficients, a_i, are then the optimal perturbation obtained from $\overrightarrow{\overline{U}}$. The energy represented by each mode is indicated by the corresponding mode eigenvalue. It will be shown by the POD results that only a few number of modes $p \leq m$ are necessary to accurately describe the system.

5.3 POD Reduced Order Modeling Results and Error Analysis

The POD reduced-order technique reformulates the 3-D CFD/HT system from a total number of DOF, n to an *m x m* eigenvalue problem. An algorithm developed on Matlab used four CFD/HT simulation results for an inlet airflow rate $\dot{v}_a$ = {0.399, 0.422, 0.446, 0.470} m^3/s ({845, 895, 945, 995} CFM). Those four CFD/HT simulation results are used as snapshots of the PCM-1 cabinet system. They are used as observations by the POD algorithm to generate flow field approximation of the PCM-1 system at a desired inlet flow rate. The following section introduces a comparison of the single parameter POD based reduced-order modeling results with the actual CFD/HT simulations.

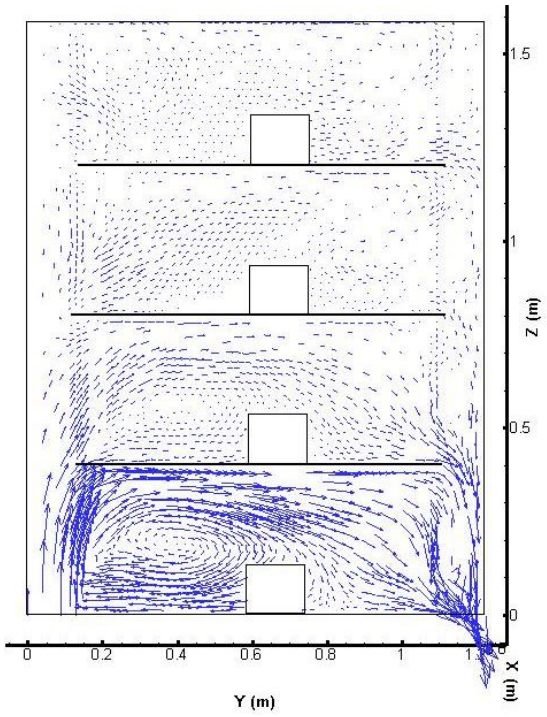

(a) CFD/HT model

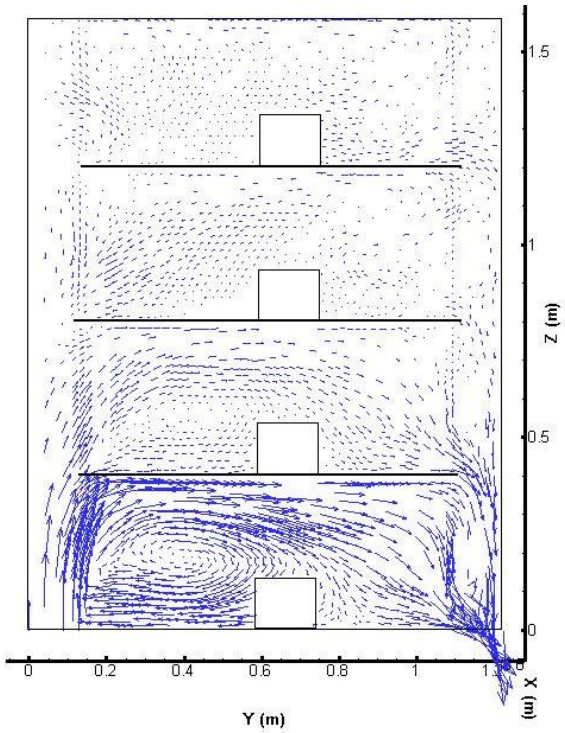

(b) POD mode

Figure 49: Cross Section of the Air Flow Velocity Field within PCM-1 at x = 0.1 m

A comparison between the flow velocity field at the cross section x = 0.1 m of the PCM-1 cabinet at operating point (inlet flow rate of 0.434 m^3/s or 920 CFM) obtained from the CFD/HT simulation and the POD model is given in

Figure 49.

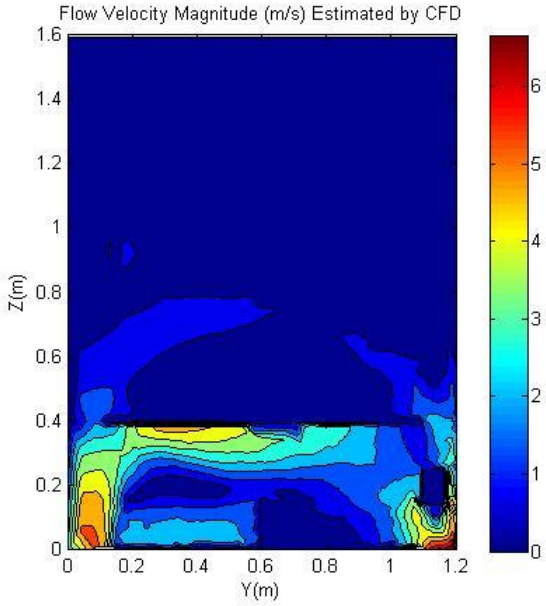

(a) CFD/HT model

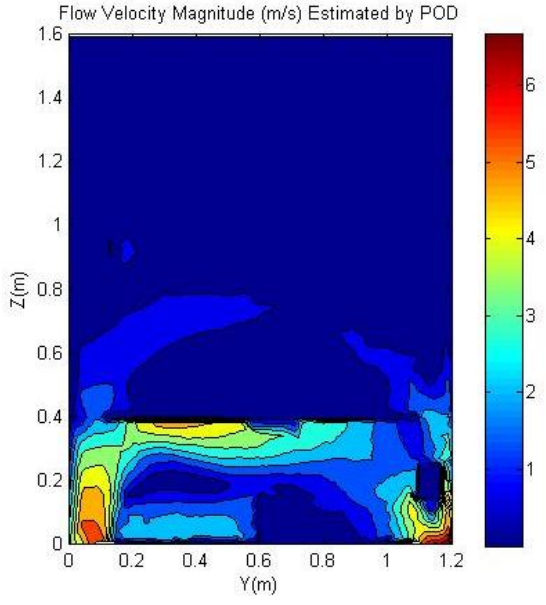

(b) POD model

Figure 50: Contours of PCM-1 Cabinet Air Flow Velocity Magnitude at x = 0.1 m

Figure 50 also gives a comparison of the air flow velocity magnitude calculated from the CFD/HT simulation and the POD model. As shown by

Figure 49 and Figure 50, both air flow fields given by the CFD/HT simulation and the POD method are extremely similar. The POD model is able to capture efficiently flow characteristics with the PCM-1 cabinet.

The local relative error *RE* in the velocity prediction between the CFD/HT and POD model can quantified as:

$$RE = \frac{\Delta u_i}{u_i} \times 100 \qquad (53)$$

where Δu_i is the absolute error made by the POD in predicting the velocity u_i. The absolute error is obtained at each nodes of the various model. The mean relative error (MRE) for the entire solution domain is defined as the sum of the relative errors at each node divided by the number of system DOF, n, as shown below:

$$MRE = \frac{1}{n}\sum_{i=1}^{n} \frac{\Delta u_i}{u_i} \qquad (54)$$

Figure 51 reveals that a mean relative error of 3.6 % is experienced for the POD-based results of the flow velocity field using only four dominant modes.

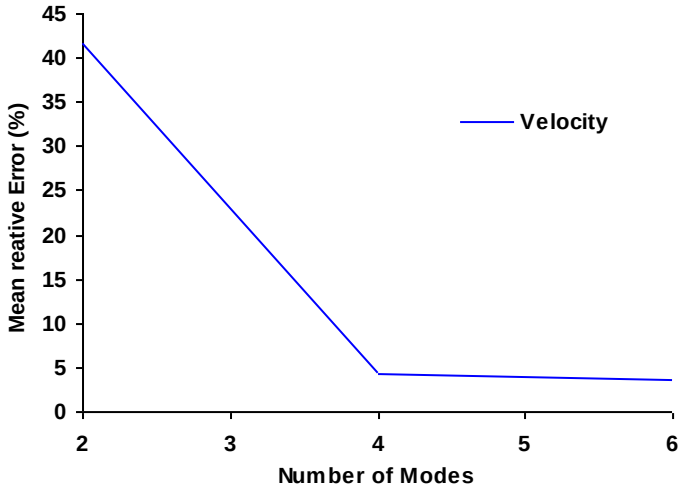

Figure 51: Flow Velocity Magnitude Relative Error

Figure 51 also illustrates the variation of the mean relative error with an increasing number of modes. It can be seen that no significant improvement in the mean relative error is observed when using higher number of modes. Therefore, only four modes are used for this present reduced order system study.

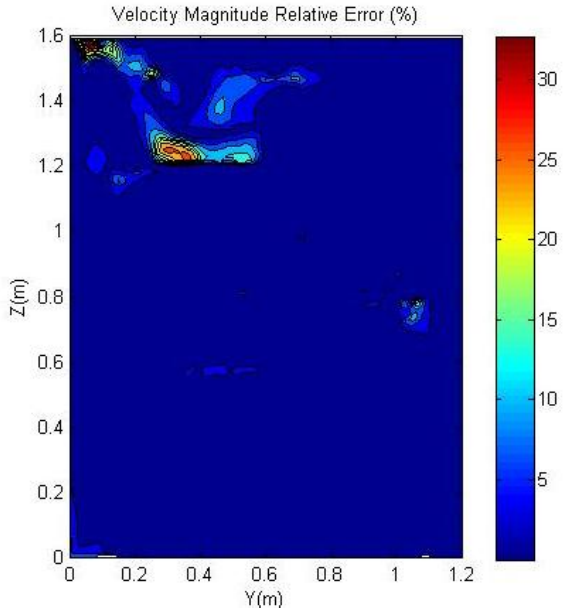

Figure 52: Flow Velocity Magnitude Relative Error of PCM-1 Cabinet at x = 0.1 m

Figure 52 illustrates that a major part of the flow field domain experiences local relative errors within 2%. It is important to note that the largest relative errors are located in the regions of small flow velocities. As suggested by the local relative error definition, even small absolute errors would result in large relative errors as the local flow velocity tends to zero. As stated before, a mean relative error of 3.6% and maximum absolute error of 0.46 m/s are experienced. These results are more than acceptable at the system scale and for the objectives of this study.

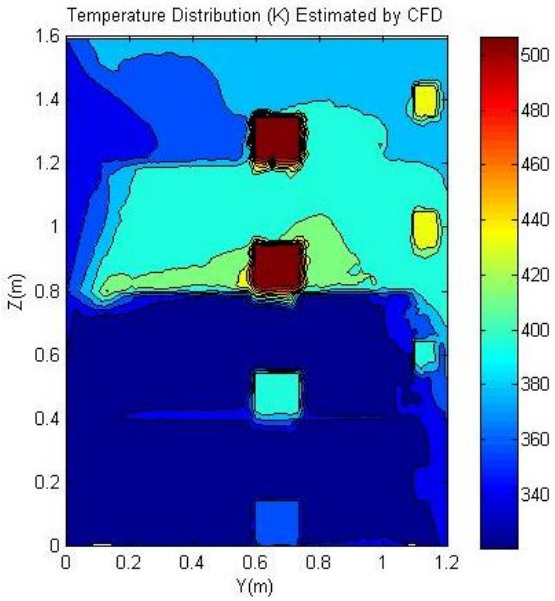

(a) CFD/HT model

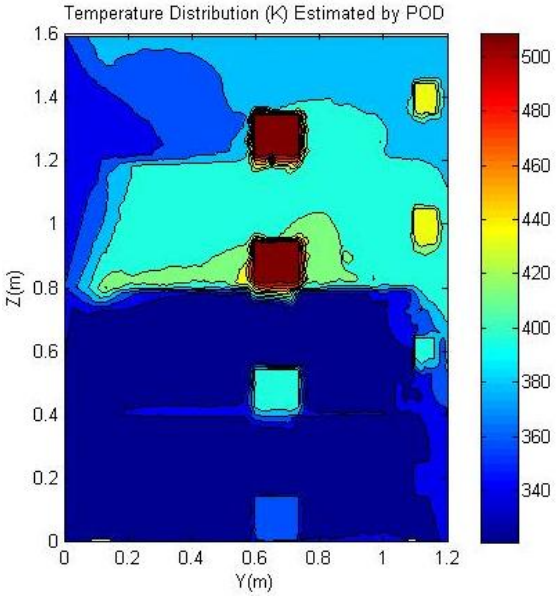

(b) POD model

Figure 53: PCM-1 Cabinet Air Flow Temperature at x = 0.1 m

Figure 53 gives a comparison of the PCM-1 airflow temperature field at operating point from the CFD/HT simulation and the 4-mode POD solutions. It can be seen that the temperature results given by the CFD/HT and the POD models are even closer than the previously described flow velocity field solutions. As illustrated by the following figure,

the mean relative errors are respectively 0.04 % and 0.15 % for the pressure and temperature fields using the four-mode POD model.

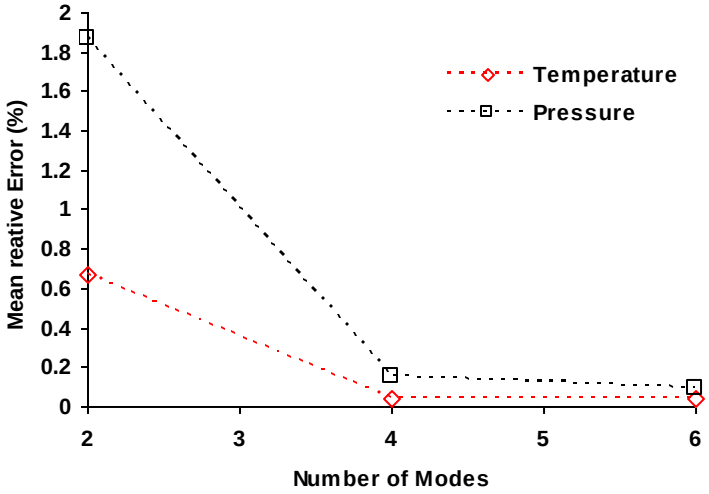

Figure 54: Relative Error for Pressure and Temperature Fields

The energy captured by each POD mode is defined as:

$$E_k = \frac{\lambda_k}{\sum_{j=1}^{N} \lambda_j} \tag{55}$$

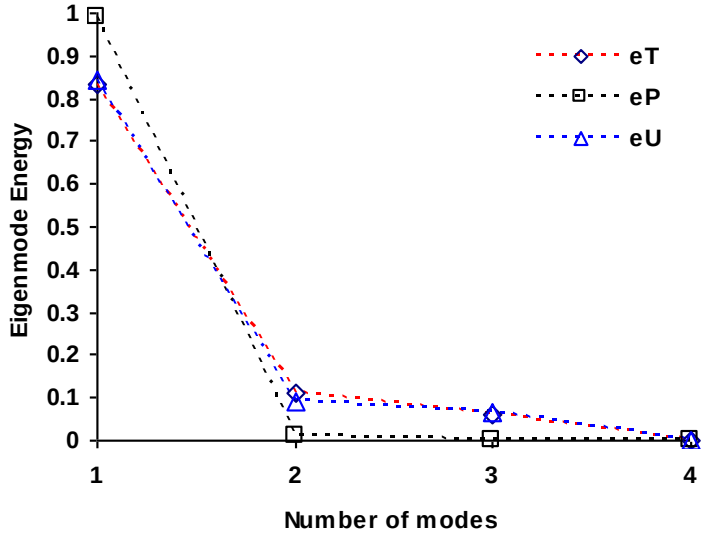

Figure 55: Eigenvalues Energy Spectra for Flow Velocity, Temperature, and Pressure Fields

Figure 55 illustrates the energy captured by various numbers of modes. The fact that four modes are enough to capture the flow behavior with the system is shown here again since the energy tends to zero for number of modes larger than four.

The choice and number of observations and the range of observation parameter in a POD analysis has a major impact on its rate of convergence and the relative error. As said before, a single parameter POD model is developed using 4 system observations for a cold plenum inlet air flow rates $\dot{v}_a$ = {0.399, 0.422, 0.446, 0.470} m^3/s ({845, 895, 945, 995} CFM). Increments of 0.0236 m^3/s (50 CFM) in the air flow rate is experienced between each system observation. In order to define the effects that the observations have on the accuracy of the POD based results various number of observations and snapshot ranges are considered as shown in Table 12.

Table 12: Effects of Observations on the POD Results Accuracy

	Range 1	**Range 2**	**Range 3**	**Range 4**	**Range 5**	**Range 6**
POD Snapshots [CFM]	{895, 945}	{870, 970}	{795, 895}	{845, 895, 945, 995}	{845, 870, 895, 945, 970, 995}	{845, 995}
CFM Range	50	100	100	150	150	150
Number of Observations	2	2	2	4	6	2
Operating Point (920 CFM) Location	Centered	Centered	Non-centered	Centered	Centered	Centered
Temperature RE	0.08 %	0.25 %	0.29 %	0.04 %	0.04%	0.67%
Pressure RE	0.11 %	0.47 %	0.66 %	0.15 %	0.09%	1.87%
Velocity RE	6.55 %	23.47 %	18.14 %	3.57 %	4.38 %	41.70 %

The objective of this error analysis study is to identify the most effective number and range of observations to optimize the POD generated flow fields. As shown, tremendous variations of the flow field relative error are observed depending on the observation parameters chosen. The following conclusions are obtained:

- The flow velocity field accuracy is more sensitive to the choice of observation range and numbers than the pressure or the temperature field predictions.
- By comparing results from Range 1 and Range 2, it can be seen that with the same number of observations (2), the smaller observation range gives POD based temperature, pressure, and velocity field better accuracy.
- By comparing results from Range 2 and Range 3, it can be observed that better predictions are obtained when the reconstructed flow field is closer to an actual observation.
- By comparing results from Range 4 and Range 6, it appears that increasing the number of observations on the same range does not necessarily improve the accuracy of the generated flow field. Pressure predictions are more accurate while velocity results are worse. This confirms the results shown by Figure 54 and Figure 55. Increasing the number of observations is unnecessary if the physics of the system is already captured. Despite the fact that increasing the number of observations does not improve the performance of the POD model, it may also have negative effects. It was noticed that the 2 additional observations slow down the POD algorithm since it may takes up to 5 extra seconds to generate a new flow field, depending on the computational power available.

CHAPTER 6

CONCLUDING REMARKS

The thermal analysis of the PCM cabinets used within the IPS architecture of future all electric Navy ships is presented. The modeling framework introduced in this study offers a full-field 3-D analysis of the thermal-fluid performance of complex air-cooled power-electronics enclosures such as the PCM-1 and PCM-2 cabinets. An accurate methodology for multi-scale field predictions of steady state and transient turbulent convection flow is presented. Usually, CFD/HT models of package-level or system-level electronics thermal- fluid problem require high meshing resolution to predict sharp gradients accurately within the system. By using a uniform grid size, the smallest length scale dictates the mesh distribution within the system-level CFD/HT model and results in extremely large mesh that are computationally impossible to solve.

One of the major contributions of this work is the approach proposed to develop compact models of the systems that are able to capture the multi-scale disparity of the problem. A multi-scale methodology has been developed to predict accurately the overall airflow conditions at the cabinet level as well as the airflow around components which dictates the chip temperature. The multi-scale disparity and the difficulties related to it, are handled by partitioning the studied power-electronics cabinets into a number of models of different natures and length scales as illustrated by Figure 56. An analytical model of the heat exchanger-fan bank located in the bottom is developed and connected to a CFD/HT model of 7,000,000 nodes representing the 4 upper bays of the cabinet containing a hundred electronic devices with various heat loss densities. A model of the IGBT multi-chip module and its heat sink with a mesh size of 0.20 mm and almost

4,700,000 nodes is also developed to predict precisely the thermal behavior of power electronics with such small length scale.

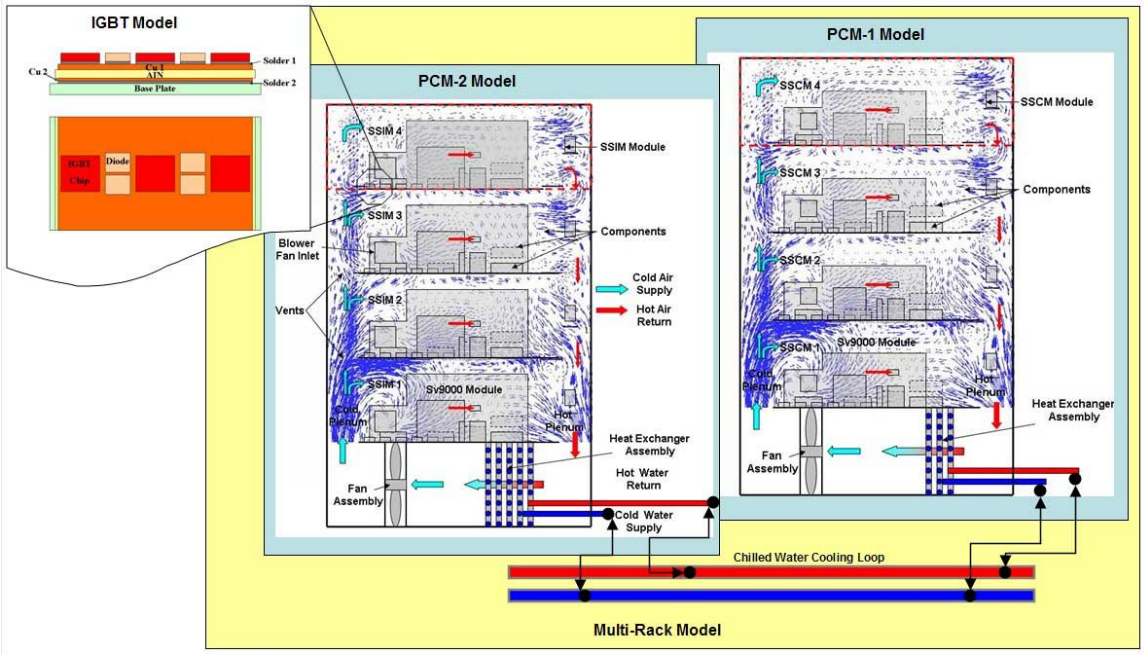

Figure 56: Methodology for Multi-Scale Modeling of Power Cabinets

The various models of different length scales are linked together by matching the boundary conditions. The advantage is that it allows high fidelity models at each length scale. That way, more accurate simulations are obtained than what could have been accomplished with a single model methodology. Also, the smallest features to be modeled can be selected according to the available computational resources. To accurately predict only one PCM cabinet using a CFD/HT model with a single uniform grid based on the smallest length scale, 180 x 10^9 nodes would have been required.

From the PCM-1 model under the prescribed design parameters, the following conclusions are reached:

- The PCM-1 cabinet operating point airflow rate is found to be 0.434 m3/s (920 CFM) which is much lower than the design requirements.

- The flow is unevenly distributed through the four bays of the PCM-1 cabinet. Approximately 90 % of the cold plenum inlet flow rate goes exclusively through Bay 1 and Bay 2.
- Re-circulation and reverse flow are observed in regions experiencing a lack of flow motion.
- As a result high temperature of the air flow and consequently high component temperatures are also experienced in the upper bays of the cabinet.

The same conclusions are also obtained from the PCM-2 analysis. The operating point airflow rate appears to be even smaller with 0.382 m^3/s (810 CFM). Since the PCM-2 cabinet experiences larger heat losses than PCM-1, even larger temperature discrepancies between the bays are observed in the airflow and the component temperatures. Further investigation would be required to complete and validate the present thermal analysis. The impact on the overall cabinet operating airflow rate of fan selection as well as the type and the number of heat exchangers should be investigated. In addition, comparing the thermal modeling results with the actual system data obtained through experiments would allow to verify the simulation accuracy at the system level.

The second major contribution of this work is the development of reduced-order models (ROM) based on proper orthogonal decomposition. POD based modeling methodology has been performed to develop the reduced order compact models of the PCM cabinets. The POD algorithm bases its approximations on full-field CFD/HT simulation results. The reduced-order modeling approach based on POD reduces the numerical models containing 35×10^9 DOF down to less than 20 DOF, while still retaining a great accuracy. Using CFD/HT observations for a single system parameter, the airflow rate, the POD model reconstruct the 3-D cabinet. It is shown that using four snapshots {0.399, 0.422, 0.446, 0.470} m^3/s ({845, 895, 945, 995} CFM) yields results

within 30 seconds as opposed to the CFD/HT simulations that take more than 3 hours. Only 4 modes are needed to capture the physics involved in cooling of the PCM cabinets. The prediction accuracy is also studied. It appears that the mean error is within 3.6% for the velocity field, and within 0.04% for the temperature field, and 0.15% for the pressure field. Since the POD model use data input from the CFD/HT model, its accuracy is entirely dependent upon the accuracy of the observations the decomposition operates on. In other words, if the CFD/HT full-field simulations used as observations are inaccurate or based on invalid assumptions, as a result the POD based system domain reconstructions would also be incorrect. The impact on the quality of predictions of the number of observations and snapshot range is also investigated. The study suggests that the best predictions are obtained by reducing the snapshot range around the parameter of the desired reconstructed field. It is also observed that increasing the number of observations within the same range does not provide necessarily more accurate predictions.

The reduced-order modeling methodology developed in the present study could be a useful tool to quickly and accurately characterize the thermal behavior of any electronics system. It also provides a good basis for design and optimization purposes. The reduced-order models, along with the full-field CFD simulations, allow identification of the cooling deficiencies within the complex power cabinets. Flow mal-distribution and recirculation, along with overheating of the components, can be quickly identified and visualized by coupling the POD algorithm to an advanced numerical simulation visualization tool, such as Tecplot.

Moreover, the cabinet model can be now integrated into a system-level modeling platform to simulate a zone of multiple cabinets. The modeling of a network of PCM cabinets as used in the IPS architecture can be obtained through the combination of cabinet models and flow network modeling (FNM). FNM is a methodology to obtain flow rates, pressure drop and temperatures of a cooling system in a network representation. The cold water piping structure providing the coolant mixture to each heat exchanger within the PCMs can be considered as a network of flow paths through components such pipes, valves and heat sinks as shown below.

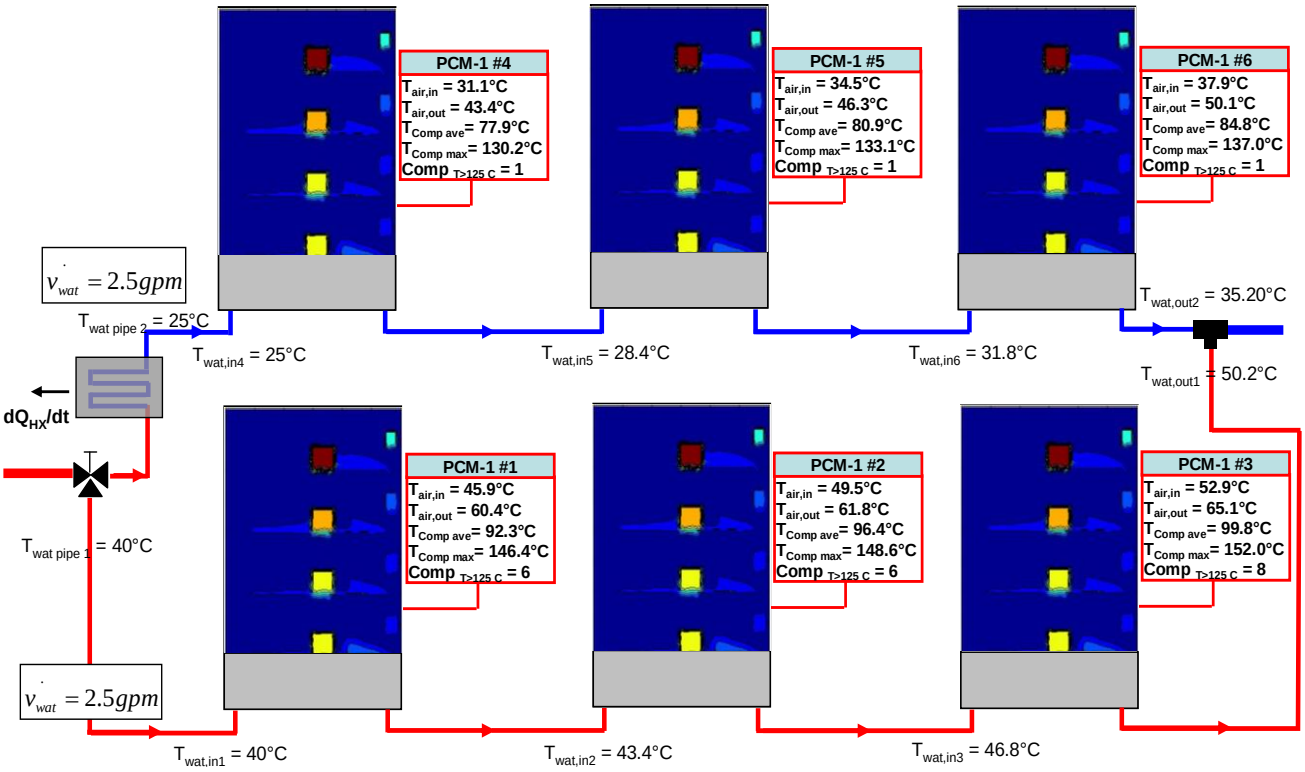

Figure 57: FNM coupled with CFD

The characteristics of these components (power, efficiency, thermal resistance) can be easily obtained and the FNM results can be used to drive the PCM models. Fast and accurate predictions of the thermal response at a multi-rack level and the resulting thermal performance of a zonal system can be obtained.

As shown, the development of reduced-order models would permit one to improve integration of simulation-based thermal analysis within the design process of any power electronics system. The reduced-order technique developed can also be used for design purposes. The system response to various heat source distributions as well as the effect of the component size can also be investigated. In such manner, the most efficient physical system configuration can be quickly obtained for a thermal management requiring the less amount of energy. However, further study would be required to define the viability and the limits of such POD-based reduced-order modeling for design optimization. The approach developed in this study requires considerable competence in heat transfer, flow mechanics as well as CFD/HT modeling and programming. A combination of multiple tools and softwares such as Gambit, Fluent, Visual Basic, Matlab and Tecplot was used. In order to facilitate future work, advanced automatic mesh generator along with a complete library of CAD detailed models of commercially-available electronic devices and systems should be integrated to the CFD/HT solvers. POD-based reduced-order modeling algorithm should be also integrated to CFD/HT programs such that the users could rapidly and accurately analyze complex systems involving thermal-fluid transport mechanisms across multiple decades of length scales.

APPENDIX A: CFD/HT MODEL MESH

In this appendix, the mesh developed for the PCM-1 and PCM-2 upper-four bays CFD/HT models is presented. In the following sections, samples of the component temperature results obtained from PCM-1 and PCM-2 models under the operating boundary conditions described in Section 4.1 and Section 4.2 are given.

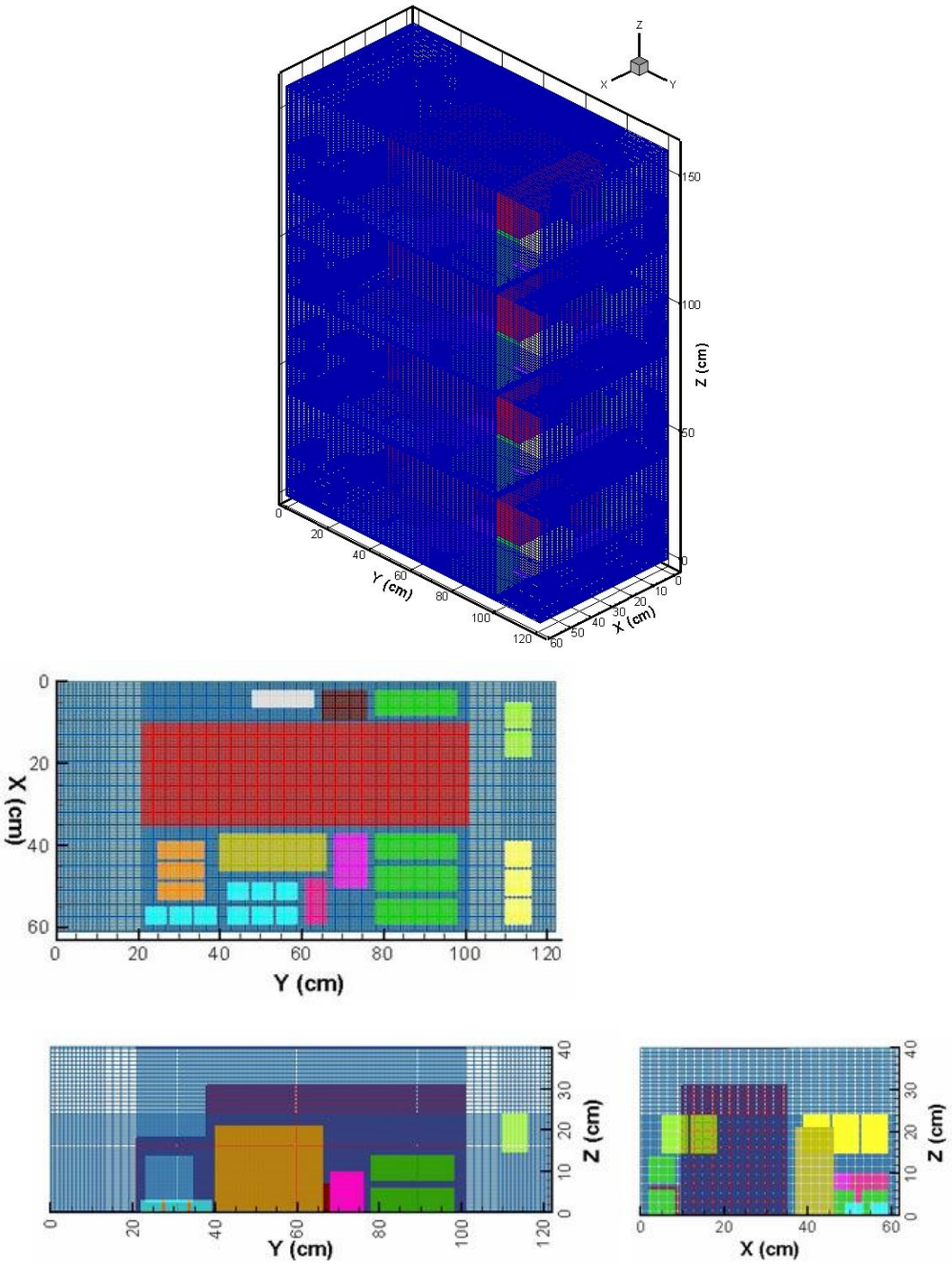

Figure 58: CFD/HT Model Mesh

APPENDIX B: PCM-2 COMPONENT TEMPERATURE

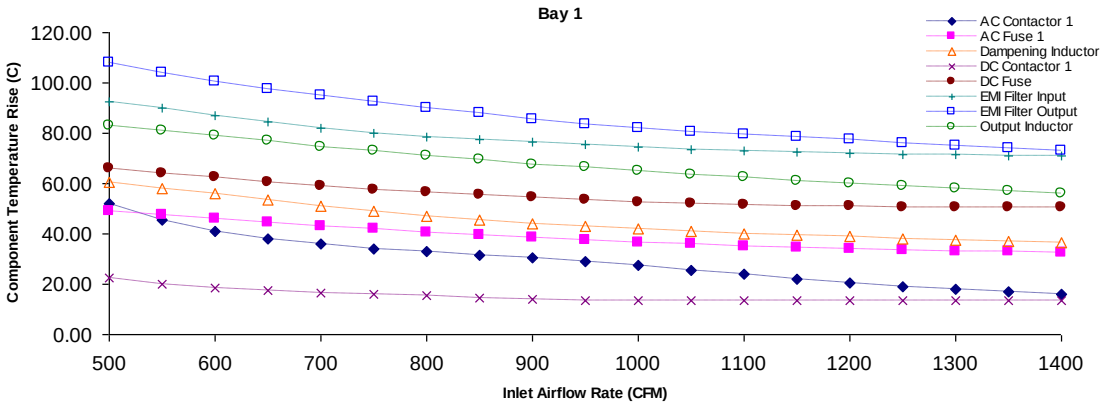

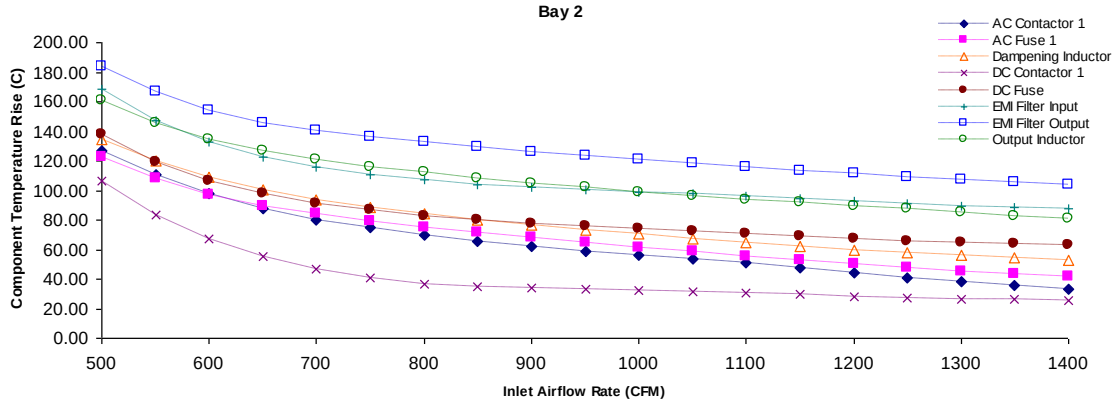

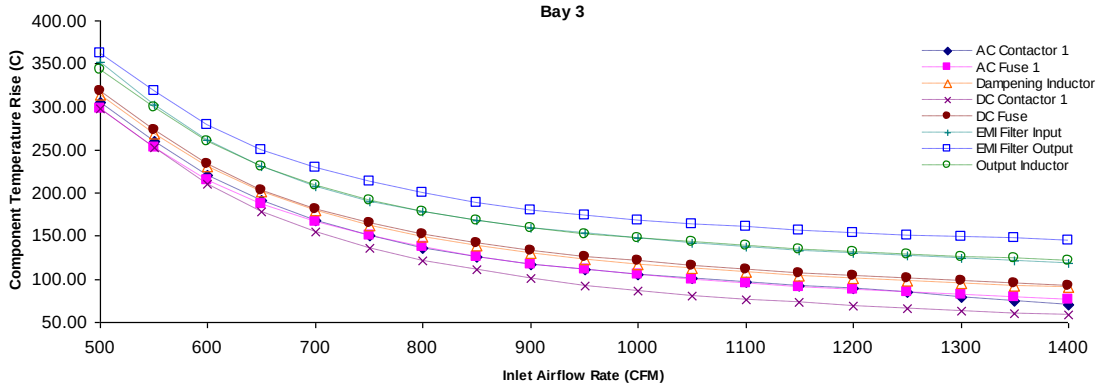

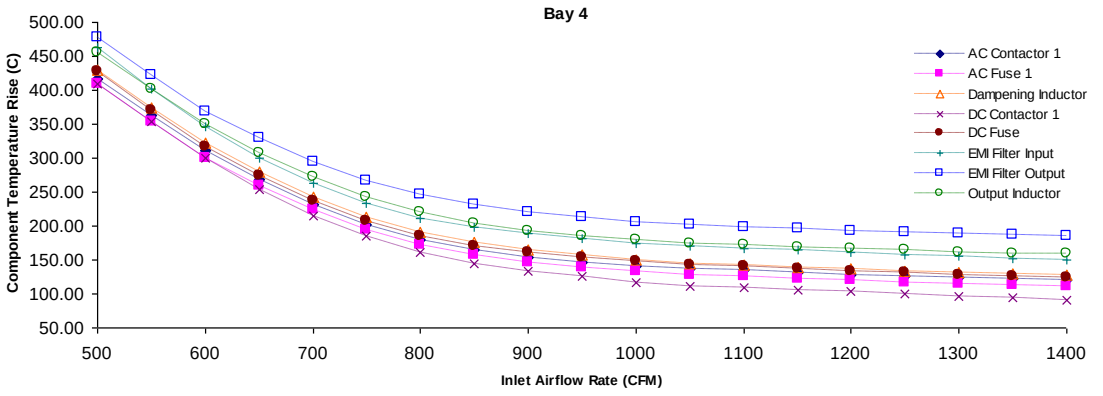

APPENDIX C: PCM-1 COMPONENT TEMPERATURE

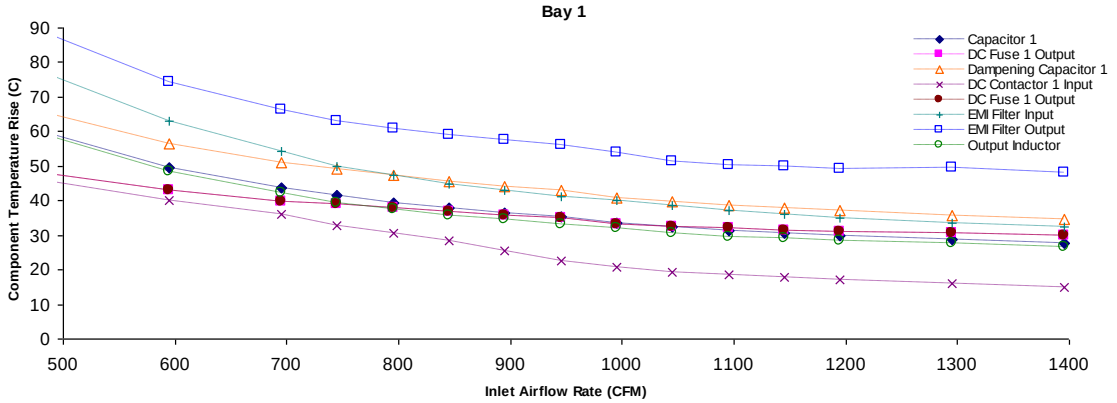

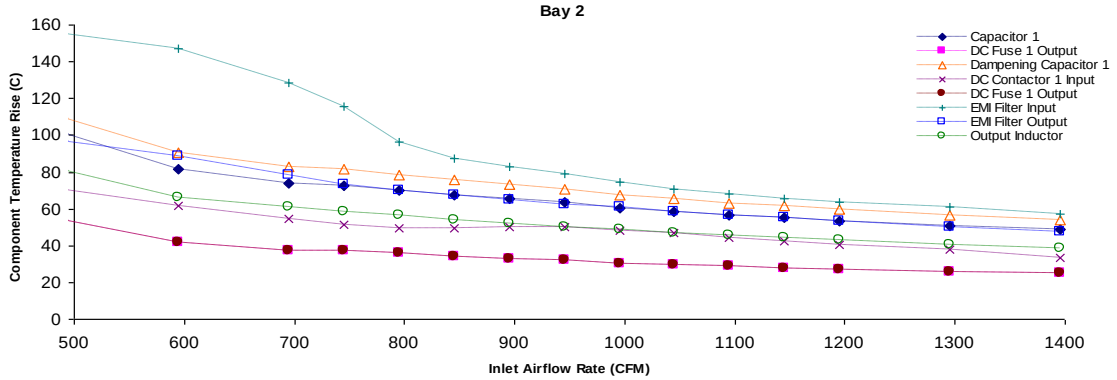

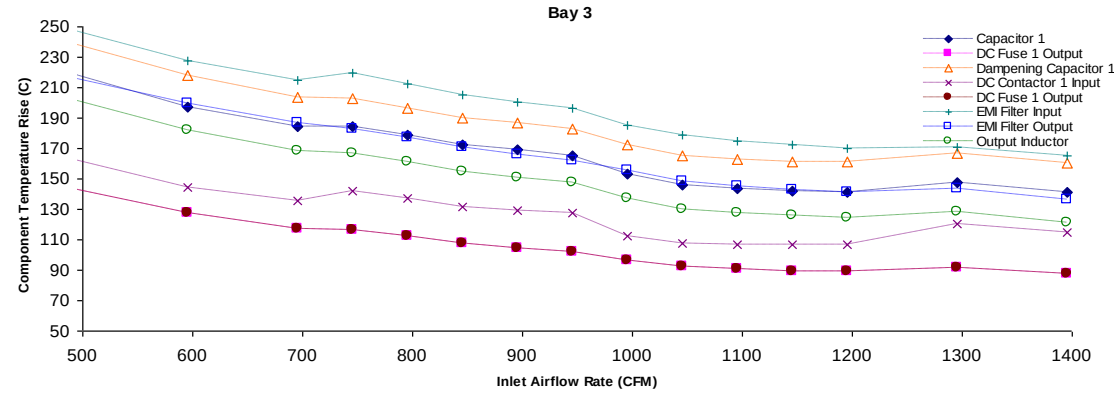

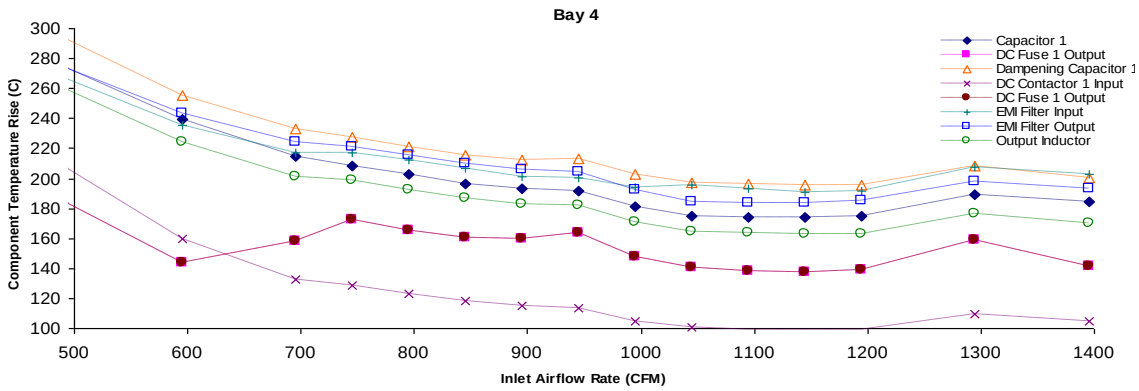

REFERENCES

1. Ericsen, T.H., N.; Khersonsky, Y., *Power electronics and future marine electrical systems,* in *Petroleum and Chemical Industry Technical Conference*. 2004.

2. Intel. *Moore's Law Official Webpage*. 2007 [cited; Available from: http://www.intel.com/technology/mooreslaw/.

3. Garimella, S.V., Joshi, Y.K., Bar-Cohen, A., Mahajan, R., Toh, K.C., Carey, V.P., Baelmans, M., Lohan, J., Sammakia, B., Andros, F., *Thermal Challenges in Next Generation Electronic Systems- Summary of Panel Presentations and Discussions.* Components and Packaging Technologies, IEEE Transactions on, 2002. **25**(4): p. 569 - 575.

4. Ohadi, M., Qi, J., *Thermal Management of Harsh-Environment Electronics.* Semiconductor Thermal Measurement and Management Symposium, 2004.

5. P. Rodgers, V.E., and M. Pecht *Extending the Limits of Air-Cooling in Microelectronic Equipment*, in *The 6th International Conference on Thermal, Mechanical and Multiphysics Simulation and Experiments in Micro-Electronics and Micro-Systems*. 2005.

6. Gardner, K.A., *Efficiency of extended surfaces.* Trans. ASME, 1945. **67**: p. 621-631.

7. Elenbaas, W., *Heat Dissipation of Parallel Plates by Free Convection.* Physica IX, 1942. **1**: p. 1-28.

8. Starner, K.E.M., H. N., *An experimental investigation of free-convection heat transfer from rectangular fin arrays.* Journal of Heat Transfer, 1963: p. 273-278.

9. Van de Pol, D.T., J., *Free Convection Heat Transfer from Vertical Fin-Arrays.* IEEE Transactions on Parts, Hybrids, and Packaging,, 1974. **10**(4): p. 267 - 271.

10. Aihara, T.a.M., S. *Optimum Design of. Natural Cooling Heat Sinks with Vertical. Rectangular-Fin Arrays*. in *Proc. Int. Symp. on Cooling Technology for Electronic Equipment*. 1998. Honolulu, Hawaii.

11. Azar, K., *Advanced cooling concepts and their challenges,,* in *Eight International Workshop on THERMINIC*. 2002: Madrid, Spain.

12. Viswanath, R., Wakharkar, V., Watwe, A., Lebonheur, V., *Thermal Performance Challenges From Silicon to Systems.* Intel Technology Journal, 2000.

13. Q. Nie, Joshi, Y., *MultiScale Thermal Modeling of Microsystem Enclosure.* International Symposium on Transport Phenomena, 2006. **7**.

14. Tucker, P.G., *CFD Applied to Electronic Systems: A review.* IEEE Transactions on Components, Packaging, and Manufacturing Technology TECHNOLOGIES, 1997. **20**(4).

15. Baelmans, M.M., J.; Nevelsteen, K.;, *Flow modeling in air-cooled electronic enclosures.* Semiconductor Thermal Measurment and Management Symposium, 2003.

16. Lasance, C.J.M., *The Influence of Various Common Assumptions on the Boundary-Condition-Independence of Compact Thermal Models.* IEEE TRANSACTIONS ON COMPONENTS AND PACKAGING TECHNOLOGIES, 2004. **27**(3).

17. Vinke, H.L., C.J.M.;, *Recent achievements in the thermal characterization of electronic devices by means of boundary condition independent compact models.* Semiconductor Thermal Measurment and Management Symposium, 1997.

18. Lasance, C.J.M., Vinke, H., Rosten, H.;, *Thermal characterization of electronic devices with boundary condition independent compact models.* iEEE Transactions on Components, Packaging, and Manufacturing Technology, 1995. **18**(4).

19. Dhinsa, K.B., C.; Pericleous, K.;, *Investigation into the performance of turbulence models for fluid flow and heat transfer phenomena in electronic applications.* iEEE TRANSACTIONS ON COMPONENTS AND PACKAGING TECHNOLOGIES, 2005. **28**(4).

20. Muthuraj, M.P., N.;, *Thermal analysis of sealed enclosure for over the ocean application [marine applications].* Semiconductor Thermal Measurment and Management Symposium, 2003.

21. Gupta, A., *Modeling large-scale electronic systems using computational fluid dynamics through a "zoom-in" approach.*
Thermal and Thermomechanical Phenomena in Electronic Systems, 2002.

22. Shammas, N.Y.A.R., M.P.; Plumpton, A.T.; Newcombe, D.;, *Finite element modelling of thermal fatigue effects in IGBT modules.* IEE Proceedings on Circuits, Devices and Systems, 2001. **148**(2).

23. Wen, S.S.G.-Q.L. *Finite Element Modeling of Heat Transfer and Thermal Stresses for Three-Dimensional Packaging of Power Electronics Modules.* in *Power Electronics and Motion Control Conference*. 2000.

24. Lee, T.-Y., *Design optimization of an integrated liquid-cooled IGBT powermodule using CFD technique.* IEEE Transactions on Components and Packaging Technologies. **23**: p. 55 - 60.

25. Berning, D.R., J.; Hefner, A.; Hernandez, M.; Ellenwood, C.; Lai, J.-S., *High speed IGBT module transient thermal response measurements for model validation*, in *Industry Applications Conference*. 2003.

26. Thome, R.J.B., E.; Reed, M.;, *Integration of Electromagnetic Technologies Into Shipboard Applications.* IEEE Transactions on Applied Superconductivity, 2006. **16**(2).

27. *A Report on Design Ratings and Thermal Performance of the PCM Cabinets*. 2005, Naval Surface Warfare Center: Philadelphia, PA.

28. ASHRAE, *Datacom Equipment Power Trends and Cooling Applications*, in *American Society of Heating, Refrigeration and Air-Conditioning Engineers*. 2005: Atlanta, GA.

29. Lytron. *Selecting a Heat Exchanger*. [cited 2007 June, 2007]; Available from: http://www.lytron.com/standard/heat-exchangers-select.htm.

30. Haider, S.I., Burton, L., Joshi Y., *A Reduced Order Modeling Framework for Thermal Modeling of Shipboard Power Electronics Cabinets*, in *9th Joint AIAA/ASME Thermophysics and Heat Transfer Conference*. 2006: San Francisco, California.

31. Kakac, S., and Liu, H, *Heat Exchangers: Selection, Rating, and Thermal Design*. CRC Press ed. 2002.

32. Colebrook, C.F., *Turbulent Flow in Pipes, with Particular Reference to the Transition Region between the Smooth and Rough Pipe Laws.* Journal of the Institution of Civil Engineers, 1938. **11**: p. 133-156.

33. ASHRAE, *Duct Design*. SI Edition ed. ASHRAE Handbook Fundamentals. 1997.

34. *Porous Jump Boundary Conditions*, in *FLUENT 6.2 User's Guide*. 2005.

35. Culham, J.R.M., Y.S., *Optimization of plate fin heat sinks using entropy generationminimization.* IEEE Transactions on Components and Packaging Technologies, 2001. **2**(2): p. 159 - 165.

36. Pratt, K.W., *Digital Image Processing*. 1991, New York: Wiley.

37. Lorenz, E., *Empirical Orthogonal Functions and Statistical Weather Prediction.* Statistical Forcasting Project, 1956.

38. Feeny, B.a.K., R., *On The Physical Interpretaion of Proper Orthogonal Modes in Vibrations.* Journal of Sound and Vibration, 1998. **211**(4).

39. Cizmas, P.a.P., A., *Proper Orthogonal Decomposition of Turbine Rotor-Stator Interaction.* Journal of Propulsion and Power, 2003. **19**(0748-4658).

40. Lumley, J., *The Structure of Inhomogeneous Turbulent Flows.* Atmospheric Turbulence and Radio Wave Propagation, 1967: p. 166-178.

41. Holmes, P., Lumley, J. L., *Turbulence, Coherent Structures, Dynamical Systems and Symmetry*. 1996: Cambridge University Press.

42. Arndt. R.E.A., D.F.L., and M.N. Glauser, *The Proper Orthogonal Decomposition of Pressure Fluctuations Surrounding a Turbulent Jet*. Journal of Fluid Mechanics, 1997. **340**.

43. Efe, M.O., and Ozbay, H. , *Proper orthogonal decomposition for reduced order modeling: 2D heat flow*. Proceedings of 2003 IEEE-Conference on Control Applications, 2003. **2**: p. 1273-1277.

44. Ly, H.V., and Tran, H.T., *Modeling and control of physical processes using proper orthogonal decomposition.* Mathematical and Computer Modeling, 2001. **33**: p. 223-236.

45. Podvin, B., and J. Lumley, *Reconstructing the flow in the wall region from wall sensors.* 1182-1190, 1998. **Physics of Fluids**(10): p. 5.

46. Smith, T., Moehlis, J. and Holmes, P., *Low-Dimensional Modeling of Turbulence Using the Proper Orthogonal Decomposition: A Tutorial.* Nonlinear Dynamics, 2005. **41**: p. 275-307.

47. Kosambi, D., *Statistics In Function Space.* Journal of the Indian Mathematical Society, 1943.

48. Loeve, M., *Functions Al´eatoire de Second ordre.* Comptes Rendus Acad. Sci. Paris, 1945. **220**.

49. Karhunen, K., *Zur Spektraltheorie Stochasticer Prozesse.* Ann. Acad. Sci. Fennicae, 1946. **A1**(34).

50. Pougachev, V., *General Theory of Correlations of Random Functions.* Izv. Akad. Nauk. SSSR. Math. Ser, 1953. **17**.

51. Obukhov, A., *Statistical Description of Continuous Fields.* Trudy Geophys. Int. Akad. Nauk. SSSR., 1954(24).

52. Theodorsen, T., *Mechanism of Turbulence*, in *2nd Midwestern Conference on Fluid Mechanics*. 1952: Ohio State University, Columbus, OH.

53. Townsend, A., *The Structure of Turbulent Shear Flow*. 1952: Cambridge University Press.

54. Chatterjee, A., *An Introduction to the Proper Orthogonal Decomposition.* Current Science, 2000. **78**(7).

55. Sirisup, S.a.K., G. E., *Stability and Accuracy of Periodic Flow Solutions Obtained by a POD-Penalty Method.* Physica D, 2005. **202**: p. 218-237.

56. Taylor, J.A.a.G., M. N., *Towards Practical Flow Sensing and Control via POD and LSE Based Low-Dimensional Tools.* ASME Journal of Fluids Engineering, 2004. **126**: p. 337-345.

57. Utturkar, Y., Zhang, B., and Shyy, W., *Reduced-Order Description of Fluid Flow with Moving Boundaries by Proper Orthogonal Decomposition*
International Journal of Heat and Fluid Flow, 2005. **26**: p. 276-288.

58. Galletti, B., Bruneau, C. H., Zannetti, L., and Iollo, A., *Low-Order Modeling of Laminar Flow Regimes Past a Confined Square Cylinder.* Journal of Fluid Mechanics, 2004: p. 161-170.

59. Rambo, J., *Reduced-order Modeling of Multiscale Turbulent Convection: Application to Data Center Thermal Management*, in *Department of Mechanical Engineering* 2006, Georgia Institute of Technology: Atlanta, GA.

60. Rempfer, D., *On Low-Dimensional Galerkin Models for Fluid Flow.* Theoretical and Computational Fluid Dynamics. **14**(2): p. 75-88.

61. Tarman, I.H.a.S., L., *Extensions of Karhunen-Loeve Based Approximations of Complicated Phenomena.* Computer Methods in Applied Mechanics and Engineering, 1998. **155**: p. 359-368.

62. Park, H.M.a.J., W. S., *The Karhunen-Loeve Galerkin Method for the Inverse Natural Convection Problems.* International Journal of Heat and Mass Transfer, 2001. **44**(1): p. 155-167.

63. Deane, A.E., Kevrekidis, I. G., Karniadakis, G. E., and Orszag, S. A., *Low-Dimensional Models for Complex Geometry Flows: Application to Grooved Channels and Circular Cylinders.* Physics of Fluids A, 1991. **3**(10): p. 2337-2354.

64. Ma, X.a.K., G. E., *A Low-Dimensional Model for Simulating Three-Dimensional Cylinder Flows.* Journal of Fluid Mechanics, 2002. **458**: p. 181-190.